AD-A243 616

Design and Performance of Controlled-Diffusion Stator Compared With Original Double-Circular-Arc Stator

Thomas F. Gelder,
James F. Schmidt,
and Kenneth L. Suder
Lewis Research Center
Cleveland, Ohio

Michael D. Hathaway
Propulsion Directorate
USAARTA-AVSCOM
Lewis Research Center
Cleveland, Ohio

91-14345

Summary

Airfoil shapes that control the diffusion of velocity over the blade row surfaces can improve fan or compressor performance over simpler, conventional blade shapes; or the same performance might be achieved with fewer, more highly loaded controlled-diffusion shapes. The objective of the present study was to compare the performance capabilities of a fan stator blade row having controlled-diffusion (CD) blade sections with the performance capabilities of one having double-circular-arc (DCA) blade sections. A CD stator with the same chord length as a DCA stator but with half the numbers of blades was designed and tested. The DCA stator had been previously tested with the same fan rotor (tip speed, 429 m/sec; pressure ratio, 1.64).

The design system utilized, the design itself, and the steady-state aerodynamic performance of a fan stator row with CD blade sections are described and discussed. Comparisons are made between the fan stage utilizing the CD stator and the fan stage utilizing the DCA stator. Conventionally spaced radial traverse data taken upstream and downstream of the rotor and stators are presented. Extra radial detail near the inner and outer walls is also presented for some operating conditions with the CD stator. Also, chordwise distributions of surface static pressures and Mach numbers on the CD stator at 10-, 50-, and 90-percent spans are presented.

The two-dimensional performances of the CD and DCA stators had similar minimum loss coefficients except over the one-third span near the hub. In that region the CD stator losses were much higher because of increased end-wall effects. Because of these higher hub region losses, the CD stator efficiency drop (rotor minus stage efficiency, overall) was about one percentage point higher than for DCA stator at speeds from 90 to 100 percent of design. Stage stall flows were unchanged by stator design.

Introduction

Various blade cross-sectional shapes have been studied over the years in order to (1) improve fan or compressor efficiency and flow range and to (2) achieve the same performance with fewer and therefore more highly loaded blades. Airfoil shapes that control the diffusion of velocity over the surface can increase the amount of laminar flow in relation to turbulent flow and delay or avoid flow separation before the trailing edge. As a result, aerodynamic loadings can be higher with controlled-diffusion (CD) blade shapes than with conventional double-circular-arc (DCA) blade shapes without sacrificing loss levels or operating range (ref. 1). This capability can reduce the number of blades required in a conventional fan stator row, for example. Because of the potential of controlled-diffusion airfoil shapes to improve the airfoil's operating efficiency, they have found wide application in recent years. Early examples were isolated, supercritical airfoils (ref. 2), supercritical cascades (refs. 3 to 6), and subcritical stators for compressors (ref. 7). More recent applications have been for low-speed turning vanes for wind tunnels (refs. 8 and 9). Although CD shapes are more complex than DCA shapes, modern numerically controlled machining techniques should reduce difficulties in fabrication.

The objective of the present study was to compare the performance capabilities of a fan stator blade row having CD blade sections with the performance capabilities of one having DCA blade sections. A CD stator with the same chord length as the DCA stator (ref. 10) but with half the blades was designed and tested. The same fan rotor (tip speed, 429 m/sec; pressure ratio, 1.64) was used with each stator row. One-half the stator blade number was selected because (1) the stator blade element flow predictions for such a design indicated some chance of success, (2) the capabilities of the CD blading in a real flow environment could be dramatically demonstrated, and (3) existing casings for the stage could be reused.

The design and analysis system used for this CD stator is described and details of the final design are presented. The compressor test facility, instrumentation, and test procedures are then described. The overall stage and rotor performances with each stator are then compared as are selected blade element data from each stator. These data for the CD stator include the following: surface pressure distributions near tip, mean, and hub; inlet and outlet conditions including extra detail near the end walls; loss values including some typical wake profiles, blade cross-sectional geometries, and flow path dimensions.

Additional experimental data from laser anemometer studies of the midspan section of the same CD and DCA stators have recently been published (refs. 11 and 12). Similar flow field measurements have also been reported for a number of spanwise sections of the same fan rotor used here but operating without a stator (refs. 13 and 14). The symbols and equations

Summary

Airfoil shapes that control the diffusion of velocity over the blade row surfaces can improve fan or compressor performance over simpler, conventional blade shapes; or the same performance might be achieved with fewer, more highly loaded controlled-diffusion shapes. The objective of the present study was to compare the performance capabilities of a fan stator blade row having controlled-diffusion (CD) blade sections with the performance capabilities of one having double-circular-arc (DCA) blade sections. A CD stator with the same chord length as a DCA stator but with half the numbers of blades was designed and tested. The DCA stator had been previously tested with the same fan rotor (tip speed, 429 m/sec; pressure ratio, 1.64).

The design system utilized, the design itself, and the steady-state aerodynamic performance of a fan stator row with CD blade sections are described and discussed. Comparisons are made between the fan stage utilizing the CD stator and the fan stage utilizing the DCA stator. Conventionally spaced radial traverse data taken upstream and downstream of the rotor and stators are presented. Extra radial detail near the inner and outer walls is also presented for some operating conditions with the CD stator. Also, chordwise distributions of surface static pressures and Mach numbers on the CD stator at 10-, 50-, and 90-percent spans are presented.

The two-dimensional performances of the CD and DCA stators had similar minimum loss coefficients except over the one-third span near the hub. In that region the CD stator losses were much higher because of increased end-wall effects. Because of these higher hub region losses, the CD stator efficiency drop (rotor minus stage efficiency, overall) was about one percentage point higher than for DCA stator at speeds from 90 to 100 percent of design. Stage stall flows were unchanged by stator design.

Introduction

Various blade cross-sectional shapes have been studied over the years in order to (1) improve fan or compressor efficiency and flow range and to (2) achieve the same performance with fewer and therefore more highly loaded blades. Airfoil shapes that control the diffusion of velocity over the surface can increase the amount of laminar flow in relation to turbulent flow and delay or avoid flow separation before the trailing edge. As a result, aerodynamic loadings can be higher with controlled-diffusion (CD) blade shapes than with conventional double-circular-arc (DCA) blade shapes without sacrificing loss levels or operating range (ref. 1). This capability can reduce the number of blades required in a conventional fan stator row, for example. Because of the potential of controlled-diffusion airfoil shapes to improve the airfoil's operating efficiency, they have found wide application in recent years. Early examples were isolated, supercritical airfoils (ref. 2), supercritical cascades (refs. 3 to 6), and subcritical stators for compressors (ref. 7). More recent applications have been for low-speed turning vanes for wind tunnels (refs. 8 and 9). Although CD shapes are more complex than DCA shapes, modern numerically controlled machining techniques should reduce difficulties in fabrication.

The objective of the present study was to compare the performance capabilities of a fan stator blade row having CD blade sections with the performance capabilities of one having DCA blade sections. A CD stator with the same chord length as the DCA stator (ref. 10) but with half the blades was designed and tested. The same fan rotor (tip speed, 429 m/sec; pressure ratio, 1.64) was used with each stator row. One-half the stator blade number was selected because (1) the stator blade element flow predictions for such a design indicated some chance of success, (2) the capabilities of the CD blading in a real flow environment could be dramatically demonstrated, and (3) existing casings for the stage could be reused.

The design and analysis system used for this CD stator is described and details of the final design are presented. The compressor test facility, instrumentation, and test procedures are then described. The overall stage and rotor performances with each stator are then compared as are selected blade element data from each stator. These data for the CD stator include the following: surface pressure distributions near tip, mean, and hub; inlet and outlet conditions including extra detail near the end walls; loss values including some typical wake profiles, blade cross-sectional geometries, and flow path dimensions.

Additional experimental data from laser anemometer studies of the midspan section of the same CD and DCA stators have recently been published (refs. 11 and 12). Similar flow field measurements have also been reported for a number of spanwise sections of the same fan rotor used here but operating without a stator (refs. 13 and 14). The symbols and equations

used to define the performance parameters are given in appendixes A and B. The abbreviations and units used for the tabular data are defined in appendix C.

Design and Analysis System

The general procedure used in the quasi-three-dimensional, inviscid-viscous interaction system is diagrammed in figure 1. Important features which made this a practical system were code compatibility and on-line graphics. The required inputs to succeeding codes in the flow diagram were quickly obtained from the output of previous ones. Also, blade section geometry and blade surface velocity or Mach number distributions were graphically displayed for immediate assessment as desired. The individual codes in the design and analysis system utilized for the subject CD stator are described in appendix D, while the overall process is described below. (It should be noted that if the CD stator were to be designed today, some improved codes, not then available, would be utilized and the overall process upgraded.)

The compressor design program (CDP) code, (ref. 15) first made a hub-to-tip plane flow-field calculation (axisymmetric) with preliminary blade geometry that satisfied the desired velocity diagrams at the blade edges. Then another hub-to-tip calculation is made by MERIDL (ref. 16) to calculate flow through the CD stator blade row. The CDP and MERIDL codes used previous test results from the original stage at peak efficiency operation to set the bounding flow conditions for the CD stator. The CDP code does not calculate flow conditions within the blade rows. The flow within and around the stator row was analyzed by MERIDL, TSONIC (ref. 17), QSONIC (ref. 18), and BLAYER (ref. 19). If the design criteria of unseparated flow (defined later) was not achieved, new stator blade cross sections were generated by the blade element program (BEP), which is part of the CDP code.

The analysis procedure was as follows: First, the inlet and outlet Mach numbers and air angles, along with stream-tube convergence and radius change, were determined by MERIDL. Next, individual blade element cross-sectional geometry was generated by the BEP. With this blade geometry and bounding flow conditions of Mach numbers and air angles, blade-to-blade flow fields were calculated for selected spanwise sections by using the TSONIC and QSONIC codes. Although results from these two codes were essentially the same over most of the chord length, there were differences near both the leading and trailing edges as later illustrated. The QSONIC code provides better definition near the leading edge than does the TSONIC code, and it is more accurate when local velocities are supersonic. The TSONIC code, however, provides more realistic velocities near the trailing edge than does the QSONIC because TSONIC employs a mass injection routine at the trailing edge that simulates the blade wake (unpublished

addendum to ref. 17). Thus, a composite of results was used with QSONIC values over the forward half-chord (approximately) and TSONIC values over the rear half-chord.

Because the code results from MERIDL, BEP, TSONIC, and QSONIC assume an inviscid flow, boundary-layer calculations were made next. The BLAYER code (ref. 19), with its two-dimensional integral method, calculates both laminar and turbulent boundary layers. The surface velocity distributions required as input to BLAYER were from the previous TSONIC and QSONIC results. From an initial laminar boundary layer at the leading edge, the BLAYER calculation proceeded chordwise until laminar separation was assumed to occur near the start of any adverse pressure gradient. A turbulent layer was then started by using initial conditions based on a laminar separation bubble model (ref. 20). To determine whether the turbulent layer would separate before the trailing edge, the incompressible form factor H_i was continuously calculated. If the value of H_i was less than 2.0, separation of the turbulent layer was not expected and the stator blade cross-sectional profile was aerodynamically acceptable. If H_i was greater than 2.0, the profile was modified and the analysis procedure was repeated. The calculated boundary-layer displacement thickness was added to the blade metal profile for the TSONIC and QSONIC calculations. Blade sections at five spanwise locations (10-, 30-, 50-, 70-, and 90-percent spans) were designed in a similar fashion. These were then stacked in the CDP to make a blade. Geometries for any intermediate cross sections of interest were obtained from a simple CURVFIT routine. Next, a check was made to ensure the gross compatibility of the hub-to-tip and blade-to-blade solutions. Only a few iterations were required to match the boundary conditions for these codes.

Finally, a satisfactory structural analysis was required before fabrication coordinates were released. If the structure was not satisfactory, the blade geometry was changed and the process retraced as indicated in figure 1.

Aerodynamic Designs

Stages 67B and 67

The flow path for stage 67B which consisted of rotor 67 and the CD stator 67B is presented on figure 2. Axial locations of instrumentation planes and a tabulation of wall coordinates are included. Only the CD stator 67B was designed in the present study. The upstream and downstream inputs to the design of stator 67B came from the measured performance across the original DCA stator 67. This DCA stator had been previously tested with rotor 67 in a single stage configuration called stage 67. (A side view schematic of stage 67 would be the same as that shown for stage 67B on fig. 2.) The stage 67 operating point at design speed that resulted in the best overall performance for rotor 67 was selected for the stator

67B design inputs. This overall and blade element performance for stage 67 is presented in tables I to III identified by reading number 392 (RDG 392).

Table I shows a stage pressure ratio and efficiency of 1.609 and 0.884, respectively, along with a rotor pressure ratio and efficiency of 1.643 and 0.905. The airflow was 34.56 kg/sec and the tip speed was 429 m/sec. (Throughout this report all absolute values of airflow or weight flow are equivalent or corrected values, that is $w \cdot \sqrt{\theta}/\delta$. These corrections are to standard day conditions at the rotor inlet.) Descriptions of rotor 67 and stator 67B follow under separate headings.

Rotor 67

Rotor 67 had multiple circular-arc blade sections, a blade aspect ratio of 1.56, an inlet hub-to-tip ratio of 0.357, and no part-span dampers. Details of the rotor 67 design as well as those for stator 67 are discussed in reference 10.

Stator 67B

Design details are discussed under the following subheadings: Flow parameters, Geometric parameters, and Surface velocities and boundary-layer parameters.

Flow parameters.—The aerodynamic inputs to the compressor design program (CDP) for stator 67B are shown for upstream and downstream locations in figures 3 and 4, respectively. The experimental data from reading 392 are also presented. The upstream inputs consisted of spanwise profiles of total temperature, total pressure, and tangential velocity (shown as Mach number). The inputs are at the rotor 67 trailing edge location, as far as possible upstream of the stator. The downstream inputs are profiles of total pressure and tangential velocity (Mach number) located about one stator chord downstream as shown on figure 2. The weight flow from reading 392 of 34.56 kg/sec was also specified.

As shown on figure 3(b), the stator inlet total pressure was nearly constant, which was the original intent for rotor 67 with stator 67. The accompanying energy addition (total temperature, fig. 3(a)) by the rotor showed increasing values from midspan toward the tip to compensate for the relatively higher losses over that region. Downstream total pressures (fig. 4(a)) show an expected decrease from the upstream values with the biggest difference over the inner one-third span. The essentially zero tangential Mach numbers at the stator outlet (fig. 4(b)) indicate that the original design goal of axial flow there was met.

The curve fits of the total pressure data (figs. 3(b) and 4(a)) indicate some falloff near the walls. This fairing was assumed (incorrectly, as will be demonstrated later) to sufficiently account for the blockage to the flow caused by the wall boundary layers. No blockage allowances were explicitly specified as is the usual design approach.

The chordwise distribution of stream-tube height (stream-tube convergence) and the streamline radius values through the stator 67B blade row are presented in figure 5(a) and (b), respectively. This information was obtained from the MERIDL analysis. It was also required input to the blade-to-blade analysis codes (TSONIC and QSONIC) used to predict blade surface velocities. The stream tube heights ratioed to the blade span at the leading edge are shown for five different spanwise locations. These height ratios were based on passing 1 percent of the total flow of one blade-to-blade passage. Stream-tube height-to-span ratios were nearly linear in the chordwise direction and almost constant near the tip. Streamline radii ratioed to the tip radius at the leading edge (fig. 5(b)) were essentially constant through the blade row except near the hub. This follows from the wall geometry across stator 67B as previously shown (fig.2).

Geometric parameters.—The blade geometry inputs to the CDP for stator 67B are shown in figures 6 to 8 along with comparisons to the original stator 67 which was a DCA. At the outset, stator 67B chord was set equal to that of stator 67 while its blade number and thus its blade solidity was set at one half. All other blade geometry features of stator 67B were tailored to prevent turbulent boundary-layer separation before the trailing edge. Many combinations of blade angle distribution (fig. 6(a) to (e)) and blade thickness distribution (fig. 6(f) to (j)) for each of five-spanwise elements were analyzed by MERIDL, TSONIC, QSONIC, and BLAYER (see Design and Analysis System) before the ones shown were selected. It was determined from these analyses that mean-line turning rates that were relatively high near the leading edge and near the start of the turbulent boundary layer on the suction surface, and also near the trailing edge, were a successful way to control the critical suction surface velocity diffusion to avoid separation (fig. 7(a) to (e)). The constant turning rates for stator 67 are also shown on figure 7(a) to (e).

As will be shown in the next section, the stator 67B sections exhibit only slightly supersonic surface Mach numbers on the suction surface. Partly because of this, the thickness distributions (fig. 6(f) to (j)) were not a first order effect in controlling velocity diffusion over the forward half chord. The modest increase in thickness over the last 15-percent chord increased the trailing edge velocity somewhat. This, in turn, reduced the adverse pressure gradient on the suction surface which was helpful in delaying separation as illustrated later.

The mean-line blade angles at the leading and trailing edges (KIC and KOC, see app. C) required to achieve the flow velocity triangles specified by the CDP are shown on figure 8. These KIC and KOC values were the result of incidence and deviation angle inputs (also shown on fig. 8) to the CDP. The incidence angles for stator 67B were determined in large part by what was required to suppress a predicted suction surface velocity peak in the leading edge region discussed in the next section. Also the deviation angles for stator 67B were

determined by the requirement of equal surface velocities at the trailing edge using TSONIC and a trailing edge mass injection model (see in app. D, Blade-To-Blade Codes, TSONIC). The end result of these design requirements was significantly more blade camber (KIC-KOC) for stator 67B than for stator 67. For example from figure 8(a), the camber at midspan for stator 67B was about 65° and for stator 67 about 47°. Most of this difference was due to differences in incidence angle.

Surface velocities and boundary-layer parameters.—The principal acceptance criteria for blade sections or elements of the present stator 67B design was no turbulent boundary-layer separation before the trailing edge for design point operation. Boundary-layer behavior was predicted by BLAYER (described in app. D) and was directly dependent on the blade surface velocity distribution. The surface velocity distributions in terms of Mach number for the midspan section of the redesigned stator 67B and the original design stator 67 are shown on figure 9(a) and (b), respectively. The results from both QSONIC and TSONIC are shown and both are utilized to best define the leading and trailing edge regions, respectively, as previously discussed. Note the equal surface Mach numbers at the trailing edge based on the TSONIC calculation with its trailing edge injection model.

As designed, the blade loading for stator 67B was twice that for stator 67 because of its half-blade number. This is confirmed by the approximately 2 to 1 area difference within the surface Mach number envelopes.

For stator 67, (fig. 9(b)), the QSONIC calculation indicates a large velocity spike near the leading edge on the suction surface. If this spike is realistic, it would cause immediate laminar separation and a longer run of reattached turbulent flow than if not present. This is illustrated by the behavior of the incompressible form factor H_i on figure 10(b). The values of H_i for the suction surface with and without the leading edge velocity spike or overspeed are shown. However, even with the longer turbulent layer with the leading edge overspeed, the indicated turbulent layer separation at an H_i of 2.0 moves forward only to about 92-percent chord instead of about 95 percent. Although the Robert's bubble model (see app. D and ref. 20) was utilized in the boundary layer calculation to determine the initial thickness of the reattached turbulent layer, its application to the very steep velocity gradient calculated by QSONIC is open to question. Thus the actual effect of such a leading edge overspeed on causing an earlier turbulent layer separation is not known, nor is the reality of the peak. The measured loss coefficient $\bar{\omega}_\mu$ was 0.030, indicative of only a small amount of turbulent separation. This was also consistent with either of the predicted turbulent separation locations shown for stator 67 at midspan.

A major design goal for stator 67B was to minimize or eliminate any leading edge velocity spikes on any of the blade sections across the span. The midspan results for stator 67B are shown on figure 9(a). Although the QSONIC calculation indicates a minor velocity spike near 1 percent chord on the

suction surface, the predominant velocity distribution is a continual acceleration of the flow from the leading edge to about 35 percent chord. The associated H_i calculation is shown on figure 10(a). For the suction surface, the major change is that the form factor for turbulent flow remains below the 2.0 level assumed critical for separation. Thus a blade shape to handle twice the aerodynamic loading of stator 67 has been designed that, according to the analyses codes used to predict its behavior, should not result in a separated turbulent boundary layer before the trailing edge. The behavior of the boundary layer on the pressure surface indicates no turbulent boundary-layer separation for stator 67B (fig. 10(a)). This was also true for the pressure surface of stator 67 but its H_i distribution is not shown on figure 10(b) to avoid confusion with the two suction surface calculations that are presented.

Relatively large values of negative incidence angle were necessary to minimize or eliminate the velocity spike on the suction surface near the leading edge. As indicated on figure 9(a) the design incidence at midspan for stator 67B was −14° ($i_{mc} = -14°$). An even more negative incidence angle would have helped the suction surface velocity distribution but it would have aggravated a velocity spike near the leading edge on the pressure surface. Leading edge shape (radii and eccentricity of ellipse) had some influence on controlling the leading edge velocity spike as did maximum blade thickness and its location. However, incidence angle was the primary parameter used in the design of stator 67B to minimize any leading edge overspeeds. It is interesting to note that measured minimum loss incidence angles for low solidity ($\sigma < 1$) blade rows, rotors, and stators in a NASA Lewis middle-stage study (ref. 21) were in the range of −10° to −15°. Stator 67B at midspan had a solidity of 0.84 and a design incidence angle of −14°.

In comparing the critical suction surface velocity distribution for stator 67B (fig. 9(a)) with its mean-line angles (fig. 6(a) to (e)), turning rates (fig. 7(a) to (e)), and form factor (fig. 10(a)) the following perspective is suggested. The relatively high blade angle at the leading edge was quickly reduced with a relatively large but rapidly decreasing turning rate. The initially very thin laminar layer could follow these changes. Similarly at the start of the turbulent boundary layer, where it was thinnest, a relatively large but rapidly decreasing turning rate was also allowable. It was the decreasing turning rate from about 45- to 80-percent chord that relaxed the adverse pressure gradient in time to level off the form factor below its critical value. Finally, an increased turning rate was allowable over the last 20-percent chord before the form factor started a significant upward climb toward separation.

The flexibility in defining the mean line and thus the turning rates for a CD blade section (figs. 6(a) to (e) and 7(a) to (e)) allows much more control of the velocity diffusion and thus the boundary layer behavior than the linear mean lines and constant turning rates required by a DCA blade section (fig. 6(a) to (e) and 7(a) to (e)). There is additional control available through the innumerable thickness distributions which are

possible (fig 6(f) to (j)). Blade geometry options available to the designer allow the controlled diffusion concept to be applied as desired. The designer tends to have too many geometry options at first. With experience this problem decreases. A rapid way of optimizing these design choices would be very desirable. Such an approach has been initiated by Sanger (ref. 22).

The effect of the boundary-layer displacement thickness δ^*, calculated by BLAYER, was included in all the surface velocity distributions shown and used to design stator 67B. The thicknesses of these unseparated boundary layers were typically quite thin as illustrated by figure 11. The metal or fabrication coordinates of the midspan section of stator 67B are shown along with the δ^* additions. As expected, the boundary layer in the trailing edge region was much thicker on the suction surface. The increased meanline turning rate over the last 10-percent chord previously discussed can also be seen.

Use of the present design and analysis system and its results were similar for the 10-percent and 90-percent span blade sections as for the midspan section just discussed. Many geometry combinations were analyzed for each section before choices were made. The geometry for the 30- and 70-percent span sections were obtained by radially curve fitting the coefficients of the polynomial expressions defining the blade angle and blade thickness distributions for the 10-, 50-, and 90-percent sections. These intermediate blade geometries were then analyzed like the others. The surface Mach number and boundary layer form factor results for all five spanwise sections of stator 67B are shown on figure 12. The results were similar for all sections from tip to hub.

For all blade sections an attempt was made to provide a continuously increasing suction surface Mach number from the leading edge to a peak near 35 percent chord. This has been shown by other investigators (ref. 4, 6, and 23) to be preferable (at least in conventional cascade tests) to the extended plateau-type distribution as is shown for the tip and hub sections on figure 12(a) and (e). With the plateau-type distribution, a laminar boundary-layer separation can form near its beginning and create a large size bubble before reattaching as a turbulent boundary layer. The end result is premature turbulent separation with increased losses and outlet air angles. A continuously increasing suction surface velocity to a peak in the 30- to 40-percent chord region tends to fix laminar separation at or near the peak. This delay in starting the turbulent layer along with a probably smaller laminar separation bubble results in a delayed turbulent separation and lower losses. The 30- to 70-percent blade sections exhibited more of the desired nonplateau-type velocity distributions than did the 10- and 90-percent blade sections. It was not found possible during the allotted design time to improve on these velocity distributions without giving up some of the desired air turning

A comparison of design cross sections between stator 67B and stator 67 at 10-, 50-, and 90-percent span is shown on figure 13 to summarize this discussion on stator designs. The differences due to camber distribution and incidence angle are apparent across the span. Recall also the 2 to 1 difference in blade number. The metal coordinates of stator 67B on design stream surfaces at 10-, 50-, and 90-percent span are presented on figure 14.

Apparatus and Procedures

Compressor Test Facility

A schematic view of the facility is shown in figure 15. The drive system consists of an electric motor with a variable frequency speed control. The drive motor is coupled to a 5.521 to 1 ratio speed-increasing gearbox that drives the test rotor. Atmospheric air enters from a line on the roof of the building and flows through the flow-measuring orifice and into the plenum chamber just upstream of the test rotor. The air then passes through the compressor stage and the collector valve and exhausts to the atmosphere for these tests.

Instrumentation

The compressor weight flow was determined from measurements with a calibrated thin-plate orifice. The air temperature at the orifice was determined from an average of two Chromel-Constantan thermocouples. Pressures across the orifice were measured by calibrated transducers.

Radial surveys of the flow were made at three axial locations: upstream of the rotor, between the rotor and the stator, and downstream of the stator (see fig. 2).

A combination probe (cobra with an unshielded thermocouple, fig. 16(a)) and an 18° wedge probe (fig. 16(b)) were used at each axial measuring station. Their circumferential locations were selected to avoid the wakes from any upstream probes. The combination probe at station 3 was also circumferentially traversed one stator blade gap to define the stator wake. The wedge probes were used to determine static pressure, and the combination probes were used to determine total pressure, total temperature, and flow angle. Each probe had associated null-balancing equipment that automatically aligned the probe to the direction of flow. Chromel-Constantan thermocouples were used in the combination probes to determine stream temperatures. Calibrated transducers were used to measure all pressures.

Chordwise distributions of static pressures were also measured on the suction and pressure surfaces of stator 67B along the 10-, 50-, and 90-percent span design streamlines. These static taps encompassed the same flow channel between stator blades with 15 locations on the suction surface of one blade and 8 locations on the pressure surface of the adjacent blade. These tap locations are shown on figure 17.

Static pressure taps were also installed on both the outer and inner walls of the compressor casing. These pressure taps were at the same axial location as the probes but were offset

possible (fig 6(f) to (j)). Blade geometry options available to the designer allow the controlled diffusion concept to be applied as desired. The designer tends to have too many geometry options at first. With experience this problem decreases. A rapid way of optimizing these design choices would be very desirable. Such an approach has been initiated by Sanger (ref. 22).

The effect of the boundary-layer displacement thickness δ^*, calculated by BLAYER, was included in all the surface velocity distributions shown and used to design stator 67B. The thicknesses of these unseparated boundary layers were typically quite thin as illustrated by figure 11. The metal or fabrication coordinates of the midspan section of stator 67B are shown along with the δ^* additions. As expected, the boundary layer in the trailing edge region was much thicker on the suction surface. The increased meanline turning rate over the last 10-percent chord previously discussed can also be seen.

Use of the present design and analysis system and its results were similar for the 10-percent and 90-percent span blade sections as for the midspan section just discussed. Many geometry combinations were analyzed for each section before choices were made. The geometry for the 30- and 70-percent span sections were obtained by radially curve fitting the coefficients of the polynomial expressions defining the blade angle and blade thickness distributions for the 10-, 50-, and 90-percent sections. These intermediate blade geometries were then analyzed like the others. The surface Mach number and boundary layer form factor results for all five spanwise sections of stator 67B are shown on figure 12. The results were similar for all sections from tip to hub.

For all blade sections an attempt was made to provide a continuously increasing suction surface Mach number from the leading edge to a peak near 35 percent chord. This has been shown by other investigators (ref. 4, 6, and 23) to be preferable (at least in conventional cascade tests) to the extended plateau-type distribution as is shown for the tip and hub sections on figure 12(a) and (e). With the plateau-type distribution, a laminar boundary-layer separation can form near its beginning and create a large size bubble before reattaching as a turbulent boundary layer. The end result is premature turbulent separation with increased losses and outlet air angles. A continuously increasing suction surface velocity to a peak in the 30- to 40-percent chord region tends to fix laminar separation at or near the peak. This delay in starting the turbulent layer along with a probably smaller laminar separation bubble results in a delayed turbulent separation and lower losses. The 30- to 70-percent blade sections exhibited more of the desired nonplateau-type velocity distributions than did the 10- and 90-percent blade sections. It was not found possible during the allotted design time to improve on these velocity distributions without giving up some of the desired air turning.

A comparison of design cross sections between stator 67B and stator 67 at 10-, 50-, and 90-percent span is shown on figure 13 to summarize this discussion on stator designs. The differences due to camber distribution and incidence angle are apparent across the span. Recall also the 2 to 1 difference in blade number. The metal coordinates of stator 67B on design stream surfaces at 10-, 50-, and 90-percent span are presented on figure 14.

Apparatus and Procedures

Compressor Test Facility

A schematic view of the facility is shown in figure 15. The drive system consists of an electric motor with a variable frequency speed control. The drive motor is coupled to a 5.521 to 1 ratio speed-increasing gearbox that drives the test rotor. Atmospheric air enters from a line on the roof of the building and flows through the flow-measuring orifice and into the plenum chamber just upstream of the test rotor. The air then passes through the compressor stage and the collector valve and exhausts to the atmosphere for these tests.

Instrumentation

The compressor weight flow was determined from measurements with a calibrated thin-plate orifice. The air temperature at the orifice was determined from an average of two Chromel-Constantan thermocouples. Pressures across the orifice were measured by calibrated transducers.

Radial surveys of the flow were made at three axial locations: upstream of the rotor, between the rotor and the stator, and downstream of the stator (see fig. 2).

A combination probe (cobra with an unshielded thermocouple, fig. 16(a)) and an 18° wedge probe (fig. 16(b)) were used at each axial measuring station. Their circumferential locations were selected to avoid the wakes from any upstream probes. The combination probe at station 3 was also circumferentially traversed one stator blade gap to define the stator wake. The wedge probes were used to determine static pressure, and the combination probes were used to determine total pressure, total temperature, and flow angle. Each probe had associated null-balancing equipment that automatically aligned the probe to the direction of flow. Chromel-Constantan thermocouples were used in the combination probes to determine stream temperatures. Calibrated transducers were used to measure all pressures.

Chordwise distributions of static pressures were also measured on the suction and pressure surfaces of stator 67B along the 10-, 50-, and 90-percent span design streamlines. These static taps encompassed the same flow channel between stator blades with 15 locations on the suction surface of one blade and 8 locations on the pressure surface of the adjacent blade. These tap locations are shown on figure 17.

Static pressure taps were also installed on both the outer and inner walls of the compressor casing. These pressure taps were at the same axial location as the probes but were offset

in the circumferential direction. The rotative speed of the test rotor was determined by an electronic speed counter. The test data were recorded by a central data recording system.

The estimated errors of the data, based on inherent accuracies of the instrumentation and recording system are as in the following table:

Weight flow, kg/sec	±0.3
Rotative speed, rpm	±30
Flow angle, deg	±1
Temperature, K	±0.6
Rotor-inlet total pressure, N/cm^2	±0.07
Rotor-outlet total pressure, N/cm^2	±0.07
Stator-outlet total pressure, N/cm^2	±0.07
Rotor-inlet static pressure, N/cm^2	±0.04
Rotor-outlet static pressure, N/cm^2	±0.04
Stator-outlet static pressure, N/cm^2	±0.04

Test Procedure

Survey data for stage 67B were taken over a range of weight flows (obtained by adjusting back pressure on the stage with a sleeve valve in the collector) from wide-open throttle flow to the near-stall conditions at 90- 95-, and 100-percent design speed. At 50- and 70-percent design speed, surveys at all stations were made near peak efficiency flow only.

At each operating point, radially traversable probes were sequentially placed at nine, conventionally spaced locations. These locations were at the radii of the design streamlines that intersected the rotor trailing edge at 5-, 10-, 15-, 30-, 50-, 70-, 85-, 90-, and 95-percent span. For a few operating points and 90- and 100-percent speed, a near-wall data series was also obtained to better define the flow conditions in those regions. First, data was acquired at eleven different spanwise locations that favored the outer wall region (1-, 2-, 3-, 4-, 5-, 10-, 15-, 20-, 50-, 70-, and 90-percent span). Then a companion sequence at the same operating point was obtained that favored the inner wall region (10-, 30-, 50-, 70-, 80-, 85-, 90-, 95-, 96-, 97-, and 98-percent span). These companion near-wall data sets were combined into one spanwise profile of flow conditions at each measuring station.

At each position the combination probe behind the stator was circumferentially traversed to eleven different locations across the stator gap. The wedge probe was set at midgap because preliminary studies showed that the static pressure across the stator gap was constant. Values of pressure, temperature, and flow angle were recorded at each circumferential position. At the last circumferential position, values of pressure, temperature, and flow angle were also recorded for stations 1 and 2. All probes were then traversed to the next radial position and the circumferential-traverse procedure repeated.

Calculation Procedure

All data shown in this report have been corrected to standard day conditions (i.e., total pressure of 10.13 N/cm^2 and total temperature of 288.2 K) at the rotor inlet (station 1). Also, references to weight flow or equivalent weight flow, or to speed or equivalent rotative speed, are to corrected values of these variables. All flows are the orifice measured values. The tabulated blade-element data have been translated from the measuring stations along design streamlines to conditions at the blade edges. At each radial survey position downstream of the stator (station 3), the eleven circumferential values of total temperature were mass averaged to obtain stator-outlet total temperature. The eleven values of total pressure were energy averaged. The flow angle presented for each radial position is calculated based on mass-averaged axial and tangential velocities.

To obtain the overall performance, the radial values of total temperature and pressure were mass averaged. Specific equations for the various performance parameters are defined in appendix B.

The static pressures measured along the stator 67B blade surfaces were converted to and presented as either pressure coefficients, C_p (see eq. (B22)) or Mach numbers, M_s (see eq. (B23)).

Results and Discussion

This section is based on the presented figures which are drawn from detailed tabulations of the data. Emphasis is on the differences in performance between a conventional double-circular-arc stator 67 (with 34 blades), and a controlled diffusion stator 67B (with 17 blades). Design values are also noted.

Tabulations of overall stage along with rotor and stator blade element data are included as a microfiche supplement for all stage 67B operating points. The 90-, 95-, and 100-percent speeds were selected for most of the performance tests because preliminary results indicated they encompassed the best operating conditions for the stators and were best for comparisons with the design intent. From stage 67, tabulated data is presented for its best operating point at design speed. Some of these data (from reading 392) were utilized as input to the design of stator 67B as previously discussed. Full size examples of the microfiche tables are shown for the following configurations operating near their best efficiency flow at design speed: tables I to III for stage 67 (reading 392), tables IV to VI for stage 67B (reading 2609), and tables VII to X for stage 67B (readings 2795 and 2800) in the near-wall data series.

Overall Performance

On the overall performance figures 18 to 20, the independent variable is equivalent weight flow normalized by the choking value (wide open throttle) at design speed. This avoids the use of dimensional values which is also true for all the dependent variables shown. Speeds of 90, 95, and 100 percent of design are shown at flows that range from wide open throttle to near stall.

The differences in performance between stage 67B and stage 67 were small (fig. 18). Total pressure ratio and efficiency were a little lower for stage 67B. This was primarily due to higher stator 67B losses to be discussed later. Peak stage efficiencies differed about 1 to 2 percent.

The near stall line was the same for both stages. This suggests that stage stall was initiated by the rotor which was the same for both stages. (Previous tests with the rotor alone at design speed (ref. 13), indicated stall at about 0.9 flow ratio).

The different design points are also shown. For stage 67B, they were a pressure ratio of 1.609, a temperature ratio of 1.165, and an efficiency of 0.88, at a flow fraction of 0.985. These values were obtained from the best operating point at design speed for the previously tested stage 67 (reading 392, table I) as indicated earlier. At 0.985 flow fraction, the measured pressure and temperature ratios were close to the design intent but the efficiency was down about 0.02 to 0.86. However at 95- and 90-percent speed efficiencies peaked near 0.88.

The original design point values for stage 67 (ref. 10) are also indicated. They were a pressure ratio of 1.590, a temperature ratio of 1.167, and an efficiency of 0.85, at a flow fraction of 0.95. At the 0.95 flow fraction the measured pressure and temperature ratios and efficiency slightly exceeded the original design values.

The performance of rotor 67 operating with either stator 67B or stator 67 was essentially the same (fig. 19). The efficiency differences were generally less than 1 percent. Such differences are not considered significant since different installations of the same stage in the same facility, and/or measurement inaccuracies could easily account for them. Also, with the relatively large axial spacing between the rotor and stator (fig. 2), interaction effects, if any, would be small.

The difference between rotor and stage overall efficiency (stator efficiency drop, $\Delta\eta$) is one measure of overall stator performance. The minimum value of this difference is a useful basis for comparing the performance of different stator designs operating with the same rotor. This is particularly true when the rotor performance is not affected by the change in stator design as was just shown. As indicated on figure 20, the minimum $\Delta\eta$ for stage 67B varied from about 0.035 to 0.046 at speeds from 90 to 100 percent while that for stage 67 varied from about 0.028 to 0.031. Thus at speeds near to and including design, a representative difference in minimum $\Delta\eta$

between the two stages was about one point (0.01) with stator 67 indicating less overall loss than stator 67B. Reasons for this difference in stator performance are developed in a following section where stator 67B surface pressures and Mach numbers are examined.

Spanwise Distributions of Pressures, Mach Numbers, Air Angles, and Losses

Two sets of comparisons involving stator inlet (station 2) and outlet (station 3) conditions across the span are discussed next. In the first set, stator 67B data are compared to design intent in figures 21 and 22. In the second set, stator 67B data are compared to that from stator 67 at the same flow at design speed in figures 23 and 24. In each of the figures 20 to 24, total pressure is shown in part (a), static pressure in part (b), air angle in part (c) and absolute, meridional, and tangential Mach numbers in parts (d), (e), and (f), respectively.

At the stator inlet, the spanwise profile of tangential Mach number was close to the design intent for the near design flow ratio (fig. 21(f)). This, coupled to the linear wheel speed profile (not shown) resulted in near design energy addition by the rotor (see fig. 19(b), temperature ratio). The accompanying stator inlet total pressure profile (fig. 21(a)) was also near design as expected from the design inputs utilized. However, the Mach number, profile (fig. 21(d)) was about 10 percent higher than design from 10 to 90 percent span. This resulted from higher than design meridional Mach number, M_m, profiles (fig. 21(e)). These higher than design M_m values can be traced to insufficient allowance for blockages to the flow in the design of stator 67B. Further discussions of flow blockage and determinations of more appropriate values are presented in appendix E.

The higher than design meridional Mach numbers combined with the near design tangential Mach numbers resulted in stator inlet air angles about 4° less than design over most of the span (fig. 21(c)).

At the stator outlet, the spanswise Mach number profile near design flow ratio was about 15 percent higher than design (fig. 22(d)). This discrepancy is higher here than at the stator inlet (fig. 21(d)), just discussed. Stator loss levels higher than design are a contributing factor. These higher losses are reflected by the lower-than-design total pressure profile (fig. 22(a)). The stator outlet air angle achieved the design intent of 0° near midspan (fig. 22(c)). Away from midspan underturnings of up to 8° occurred near 10- and 90-percent span.

In the comparison of stator inlet conditions between stator designs at the same flow rate and design speed (fig. 23), there were insignificant differences in pressures, air angles, and Mach numbers across the span. This was not surprising with the unchanged rotor performance previously discussed (fig. 19). However, at the stator outlet station (fig. 24), there were

differences in some of the flow parameters due to the different performance of the two stator designs. The main difference was in the outlet Mach number (fig. 24(d) or (e)), which was about 13 percent higher across the span with stator 67B than with stator 67. A decrease in effective annular flow area downstream of stator 67B compared to stator 67 is required for these Mach number differences. The wall boundary-layer blockages could be different as well as blockages from different stator losses across the span. The main difference in blockage is believed to result from the higher losses for stator 67B compared to stator 67 over the inner one-third span that will be illustrated later.

Spanwise distributions of flow conditions very near the walls are contained in appendix F. There, results form the near-wall data series are presented and discussed.

Further comparisons of the effects of stator design and operating point on stator inlet and outlet flow angles are shown on figures 25 and 26. The dependence of stator inlet air angle β_2 on flow at speeds near design for five spanwis locations is shown for both stator designs on figure 25. Stator outlet air angles, β_3, as a function of inlet angle β_2 for each design and for the same spans are shown in figure 26.

There were wide swings in β_2 as the flow was throttled from wide open to near stall flow ratios. For both stators at design speed (fig. 25), this swing was about 19° near the tip and about 10° near the hub. (There were slightly higher β_2 values for stator 67 compared to stator 67B at near stall flow ratios over the outer half span for reasons unknown.)

Near midspan of stator 67B and for values of inlet air angle resulting in minimum overall stator loss (indicated by vertical arrows along abscissa of fig. 26(a) to (e), the stator exit air angle was near 0° degrees as intended. Thus, the technique of providing a blade mean-line angle at the trailing edge that results in TSONIC code predictions of equal suction and pressure surface velocities there worked very well for the present design. (See in app. D the section Blade-To-Blade Codes, TSONIC.) In contrast to midspan results, the β_3 values for minimum loss operation and near 10- and 90-percent span indicated an under turning of from 3° to 6°.

The midspan values of β_3 for stator 67 (fig. 26(f) to (j)) showed a couple of degrees of over-turning near-minimum overall loss operation. In the end wall regions (10- and 90-percent span) the β_3 values were at or near the design intent of zero degrees. The relatively good agreement between predicted and actual β_3 values across the span of stator 67 can be credited to the large amount of experimental data from double-circular-arc blading that calibrated the deviation angle prediction method used in the design process. The variation of β_3 with β_2 was less for stator 67 than for stator 67B. This resulted from a wider low loss operating range for stator 67 shown next.

Stator loss coefficients, $\bar{\omega}_w$, as a function of inlet air angle at station 2 are shown on figure 27(a) to (e) for stator 67B. and on figure 27(f) to (j) for stator 67. Three speeds near design (90, 95, and 100 percent) are shown which yielded essentially

the same results. The same loss data as a function of incidence angle to the mean line are shown on figure 28.

In the definition of $\bar{\omega}_w$ (a wake total loss coefficient, app. A), the ideal total pressure at the trailing edge was assumed to equal the average of the three highest total pressures measured across the stator gap at station 3, $(\bar{P}_3)_{3hi}$. In the tabulated stator blade element data, values of $\bar{\omega}_w$ are labelled TOTAL LOSS COEFF WAKE. An alternative definition replaces $(\bar{P}_3)_{3hi}$ with P_2. In the tabulated data these values of $\bar{\omega}$ are labelled LOSS COEFF TOTAL. The difference in stator loss coefficient values between these two definitions is generally small except near either end wall; there the LOSS COEFF TOTAL is generally higher. The $\bar{\omega}_w$ definition is preferred in the present study because it generally provided more consistent and believable sets of loss data for both stator 67B and 67. (A similar choice was made in ref. 24 for three other stator designs.) Thus only $\bar{\omega}_w$ values are utilized for the figures and discussions of the two stator designs in this report.

The minimum loss levels on figure 27 at 30- and 50-percent span were essentially the same for either stator design with values from 0.025 to 0.030. Also, the range of inlet air angles, β_2, at low loss was broader for the lighter loaded stator 67 than it was for stator 67B at all spanwise locations. At 50-percent span, a doubling of the minimum loss level requires a 13° change in β_2 for stator 67 but only 8° for stator 67B.

Mean-line incidence angles at minimum loss differed considerably between stator designs (fig. 28). For stator 67B the minimum loss incidence angle ranged from about −28° at 10-percent span (tip) to about −20° at 50-percent span (fig. 28(a) to (e)). A similar 8° swing occurred with stator 67 but at a different absolute level from about −8° to 0° (fig. 28(f) to (j)). Near the hub (90-percent span), the minimum loss levels for stator 67B were nearly double those for stator 67. At 90-percent span the minimum $\bar{\omega}_w$ for stator 67B was about 0.14. For both stator designs the minimum loss levels occurred at lower than design values of incidence angle across the span. For stator 67B this difference from design varied from about 12° at 10-percent span to about 3° at 90-percent span. For stator 67 the difference from design ranged from about 10° at 10-percent span to about 2° at 90-percent span.

A comparison of stator wake total pressure profiles at six spanwise locations between stator 67B and 67 near peak stage efficiency operation at design speed is shown on figure 29. The accompanying levels of loss coefficient are also given. Loss levels were comparable between designs at 10- to about 70-percent span. It was at 90-percent span where the biggest differences occurred as previously discussed. Where the loss levels were comparable, the higher loaded stator 67B tended to have a more narrow but deeper wake profile than stator 67.

The spanwise distribution of stator losses at their best operating point was determined for both stator designs as follows. First, the loss coefficients for 10-, 30-, 50-, 70-, and 90-percent span as a function of flow fraction were plotted

as shown on figures 30 and 31 for stator 67B and stator 67, respectively. Data for 90 and 100 percent of design are presented. From these plots, a single flow fraction was selected for each speed that minimized the loss coefficient across the span. For both stators these flow fractions were 0.910 and 0.994 for 90- and 100-percent speed, respectively. Next, the stator inlet air angles β_2 at each spanwise location and for these flow fractions were obtained from the faired lines on figure 25. Finally, with these values of β_2, the faired line values of loss coefficient were obtained from figure 27(a) to (e) and (f) to (j) for stator 67B and stator 67, respectively.

The results of the above procedure are shown on figure 32. There, the stator loss coefficients as a function of spanwise location for 90- and 100-percent speed are shown for stator 67B and for stator 67. As previously discussed, the stator losses in coefficient form were the same at either 90 or 100 percent of design speed. Generally these best operating point loss coefficients were essentially the same for either stator design over the outer two-thirds span. Only in the hub region do the losses differ with a factor of two in favor of stator 67 occurring at 90-percent span. It is this difference in stator hub region losses that accounts for the approximately one point difference in the minimum rotor minus stage efficiency values for the two stage designs discussed with figure 20.

Chordwise Distributions of Surface Pressure and Mach Number for Stator 67B

The chordwise distribution of surface pressures for the tip (10-percent span), mean (50-percent span), and hub (90-percent span) sections of stator 67B are shown on each of the figures 33 and 34. The pressures are presented in coefficient form, which minimizes the effects of differing stator inlet Mach numbers (M_2) while revealing the effects of differing stator inlet air angles (β_2). Rotor speed (percent of design, percent N_D), flow ratio w/w_{choke}, stator exit air angle β_3, stator element loss coefficient $\bar{\omega}_u$, and the difference between rotor and stage overall efficiency, called stator $\Delta\eta$, are also tabulated on these figures. The design predictions from the TSONIC/QSONIC ANALYSES are also shown.

Results for operation near the minimum stator $\Delta\eta$ are shown in figures 33 and 34. For the three rotor speeds near design (fig. 33), the inlet air angles, β_2, for each spanwise location differed by less than 2°. But even within this narrow range of β_2, the effect of decreasing inlet angle can be seen (especially in fig. 33(a)) in slightly more negative C_p values on the suction surface near 0.4 axial chord. The mean section (fig. 33 (b)) showed the lowest loss levels with a three-speed average value of 0.031. This was coupled with suction surface gradients similar to the design intent; that is, there was little evidence of separation before the trailing edge. In fact, the mean section pressure patterns were similar to predictions on both surfaces. The disagreement between the design value of

β_2 (39.7°) and the three-speed average (34.8°) was due to the underpredicted wall blockage utilized in the design process as discussed elsewhere. (See also app. E.)

The highest loss levels and the greatest departure of the C_p patterns from design intent were for the hub section (fig. 33(c)). There the premature flattening of the suction surface pressures starting near 0.45 axial chord is suggestive of boundary-layer separation. This in turn leads to high loss coefficients which averaged 0.138 for the three speeds shown. The dip in hub section C_p at 0.08 chord fraction on the suction surface, and the peak at 0.13 chord fraction on the pressure surface are not understood. They were not consistently present as subsequent plots will indicate.

The low loss, nonseparated boundary layer data for the mean section (fig. 33(b)) show outlet air angles, β_3, within 1° of the axial direction. This was the design intent. The air has been underturned about 5° in the tip region and about 7° in the hub. Loss levels and extent of suction surface separation are also higher in the hub compared to the tip sections.

The two experimental C_p distributions on figure 34 are both for 90-percent N_D but differ a little in flow rate and thus inlet air angle β_2. The 0.895 flow ratio data of figure 33 is repeated on figure 34 for comparison with data at 0.923 flow ratio. The biggest change appeared in the tip region (fig. 34(a)). The value of $\bar{\omega}_u$ was only 0.025 with β_2 of 25.7° compared with 0.047 at β_2 of 30.6°. The stronger favorable pressure gradient over the first 0.4 chord appeared responsible for the reduced loss. It probably produced a thinner laminar layer which in turn resulted in a thinner turbulent layer starting just beyond 0.4 chord. Neither turbulent layers appear to have separated before the trailing edge however. Although the lower β_2 reduced the tip section loss, losses near the mean and hub sections were increased somewhat. Overall, the stator $\Delta\eta$ of about 0.033 was essentially the same at both flow rates shown on figure 34. The local loss coefficients defining the stator wakes that accompany the figure 34 data are shown on figure 35. Large suction surface separations of the hub sections were obvious from the wake patterns.

The stator 67B C_p data for the tip, mean, and hub sections over a broad range of flow ratios at 90-percent design speed are presented in parts (a), (b), and (c), respectively, of figure 36. The accompanying stator wake measurements for these same operating points are shown in the three parts of figure 37. Together, figures 36 and 37 illustrate the large changes in pressure distributions and losses ($\bar{\omega}_u$'s) due to changes in inlet air angle β_2. The change in β_2 ranges from about 22° for the tip section, to about 15° for the mean, to about 10° for the hub. The coefficient forms of C_p and $\bar{\omega}_u$ make them essentially insensitive to changes in M_2 resulting from changes in rotor speed from 90 to 100 percent of design. Thus figures 36 and 37 for 90-percent speed would show similar results if done for 100-percent speed. The 90-percent speed data were selected for presentation because of its closer match with design intent M_2 levels.

The 0.933 flow ratio was the wide open throttle condition where at 50-percent span (fig. 36(b)) β_2 was 27.1° and $\bar{\omega}_{\kappa}$ was 0.097. There was little premature flattening of the suction surface C_p before the trailing edge. This is to be expected at such a large negative incidence angle (i_{mc} of $-27.0°$). The high value of $\bar{\omega}_{\kappa}$ appeared to result from premature separation of the pressure surface boundary layer. The corresponding wake profile (fig. 37(b)) indicated a substantial broadening of the high loss region from the pressure surface side. The 0.779 flow ratio was near stall condition where at 50-percent span β_2 values was 42.0° and $\bar{\omega}_{\kappa}$ was 0.088. Here there was premature flattening of the suction surface C_p starting near an x/C_x of 0.5. The corresponding wake profile confirmed that most of the loss came from a suction surface separation.

At 90-percent span (fig. 36(c)) the $\bar{\omega}_{\kappa}$ values were all high, ranging from 0.204 for β_2 of 39.9° to 0.144 for β_2 of 49.8°. The wake profiles for all hub β_2 values were similar (fig. 37(c)). They all indicated a premature suction surface separation as did the C_p distributions. In contrast to the mean and tip sections, there was no β_2 value for the hub section low enough to suppress the suction surface separation before the trailing edge. Reasons for this behavior are discussed later in this section.

At 10-percent span (fig. 36(a)) and a flow ratio of 0.852, the M_2 and β_2 values were close to the design predictions but the C_p distribution was not. The suction surface indicated a short, relatively flat coefficient near the leading edge. This was followed by an adverse pressure gradient that indicated premature separation around midchord. The accompanying loss coefficient $\bar{\omega}_{\kappa}$ was relatively high at 0.070.

Relatively high losses also occurred in cascade tests of another, similar, CD stator section design (ref. 5). There similar indications of separation starting before midchord were measured for near design inlet flow conditions. At those conditions, flow visualization studies (ref. 5) revealed a rather large laminar separation bubble in the forward chord region with a flattened pressure distribution beneath it. The reattached turbulent boundary layer following such a bubble was believed to be substantially thickened and therefore less able to negotiate an adverse pressure gradient. (A corner suction slot starting in the region of reattachment precluded an observation of this boundary-layer thickness). Similar boundary layer behavior is attributed to the figure 36(a) results at the near design inlet conditions.

A similar premature suction surface separation also appeared at midspan with the same 0.852 flow ratio (fig. 36(b)). There, inlet conditions (M_2 of 0.62, β_2 of 37.1°) were not far from design (M_2 of 0.64, β_2 of 39.7°). It appears that premature separation of the laminar boundary layer with perhaps a large separation bubble before reattachment of a thick turbulent layer on the suction surface must be avoided for low loss operation.

The BLAYER calculation using the design C_p distributions did not predict the early laminar separations experienced at either 10- or 50-percent span. This occurred in spite of

generally favorable although modest pressure gradients to about 15- or 35-percent chord for the 10- or 50-percent spans, respectively. Stronger, favorable gradients for these highly loaded blades appear necessary for low loss operation as illustrated next.

The midspan section results from stator 67B at design speed with a strong, favorable gradient on the suction surface from the leading edge to about 40-percent chord is compared to design gradient results on figure 38. Surface Mach number M_s distributions are utilized here to emphasize the absolute values involved. The value of M_2 was the same (0.70) while β_2 differed by only 3.8°. At the lower β_2 of 35.6° (fig. 38(a)), the strong, favorable pressure gradient on the suction surface maintained a thin, laminar boundary layer to about 40-percent chord. There was no local flattening of the surface Mach numbers that accompanied the laminar separation bubbles observed in the reference 5 tests. Over the last 60-percent chord, a strong adverse pressure gradient existed. Since there was little departure from the calculated Mach number distribution there, an unseparated turbulent boundary layer that starts relatively thin a little beyond 40-percent chord is envisioned. In contrast at a β_2 of 39.4° (fig. 38(b)), there was a flat M_s distribution on the suction surface near the leading edge. Then the adverse gradient started early, at about 17-percent chord, with evidence of separation near 45-percent chord. The difference in $\bar{\omega}_{\kappa}$ was a factor of three between the two β_2 values shown. (The corresponding wake profiles are shown on fig. 39.) There was also a 5.5° difference in the exit air angle, β_3. With the premature separation of figure 38(b), the flow was underturned about 6° from the design intent. Based on the present data and similar results from cascade tests of other CD blade sections (refs. 6 and 23), a continuously strong, favorable gradient to about 35- to 40-percent chord is recommended for highly loaded blades in order to avoid premature laminar and then premature turbulent separation and high loss. It is also of interest to note that with the strong, favorable, suction surface gradient (fig. 38(a)), the blade surface Mach numbers calculated by the blade-to-blade codes agreed very well with the data when the input boundary values (like M_2 and β_2) were the same as those measured.

When stator 67B sections were operating near minimum loss at 90-percent design speed, the surface Mach number (M_s) distribution for the tip section was nearly the same as for the mean section as indicated by figure 40(a). The loss levels $\bar{\omega}_{\kappa}$ were also about the same. Also, since M_2 was about the same for each section, their C_p distributions (fig. 40(b)) were similar even though their β_2 values were quite different (25.7° and 34.0°); incidence angles differed by about the same amount. (See blade element tables.) The conclusion is that similar M_s distributions result in similar section loss levels, regardless of other differences, at least in the low loss regions of stator 67B over its outer half span.

The hub section (90-percent span) of stator 67B showed boundary-layer separation from the suction surface around midchord at all operating conditions, some of which were

previously shown (fig. 36(c)). Even at the lower speeds of 70 and 50 percent of design, similar patterns of premature separation were evident as shown in figure 41.

The usefulness of the pressure coefficient in comparing data at different values of M_2 is demonstrated again in figure 41(b). Since the values of β_2 were nearly the same, the C_p distributions taken at 50-, 70-, and 90-percent speed were in good agreement. The M_s distributions (fig. 41(a)) reveal the different absolute gradients which, in turn, are significant to the behavior of the boundary layers. The $\bar{\omega}_\kappa$ values decrease dramatically with speed, from 0.159 with M_2 of 0.77 to 0.043 with M_2 of 0.44. The accompanying wakes (fig. 42) confirmed the differing suction surface separations with their sizable changes in $\bar{\omega}_\kappa$.

It was the relatively poor performance over the one-third span nearest the hub that was responsible for the minimum stator $\Delta\eta$ being about one point higher for 67B than for stator 67 at speeds of 90 to 100 percent of design (fig. 20). Thus it is instructive to further examine the surface Mach number distributions near the hub and compare them to those at midspan where the performance was very good, at least for some inlet air angles (fig. 33(b)). This is done with the help of figure 43.

The M_s patterns over the forward one-third chord of the suction surface were similar for both hub and mean sections. However, the Mach number distribution for the hub section indicated a flow separation near 50-percent chord, whereas for the mean section no flow separation was apparent. The corresponding loss coefficients, $\bar{\omega}_\kappa$, were much different, 0.159 for the hub but only 0.029 for the mean.

The premature separation of the hub section suction surface boundary layer occurred at all speeds and flows tested (even at low levels of diffusion factor D, see tabular data).

Even the strongly favorable Mach number gradient achieved over about the first one-third chord of the hub section was not sufficient to avoid premature turbulent boundary-layer separation as it did for the mean section. Such favorable forward chord distributions also prevented early turbulent layer separation from the tip section as previously discussed (fig. 34(a)). Thus, non-two-dimensional flow effects in the hub end wall region are believed responsible. A corner stall (between stator blade suction surface and hub end wall) and/or secondary or cross flows in the hub end wall region are two possible flow mechanisms. Therefore, a simple reshaping of the stator 67B blade sections near the hub is not likely to significantly improve their performance. Instead, a redesign that minimizes or eliminates a possible corner stall, and/or reduces cross flows in the hub region is recommended. Such a redesign could include changes to the rotor, the hub wall contour, or the stator.

When the stator blade number was cut in half for stator 67B (with the same air turning requirements as for stator 67) the blade loading and cross flow gradients were doubled. Also, with only half the blades, there was twice the amount of lower energy flow along the hub wall per blade passage. To improve

the hub region flow[1] by stator redesign, two changes are suggested. One is to increase the blade number somewhat, and the other is to reduce the chord length, at least in the hub region (see ref. 24).

The benefits of increasing the blade number to decrease losses in the hub section are illustrated on figure 44. Here some unpublished surface Mach number distributions measured on stator 67A operating with R67 are compared with those at similar inlet conditions for stator 67B. Stator 67A was an alternate controlled diffusion design of the type described by Sanger in reference 22. The stator 67A design has the same chord and blade number (34) as the original DCA, stator 67. The measured wake local loss coefficients are also shown on figure 44 for all three stator designs, all operating with the same rotor. The more lightly loaded stator 67A shows little or no evidence of boundary-layer separation from the upper surface in the M_s distribution plot. The accompanying stator loss coefficient of 0.096 is also an improvement over the stator 67B value of 0.135. The original stator 67 has the lowest value of loss coefficient, 0.080. Unfortunately there were no stator 67 surface pressure measurements from which M_s distribution comparisons could be made.

The 90-percent span sections of stator 67 and 67A do not exhibit suction surface Mach number distributions that indicate significant separation but their loss levels are still high compared with spanwise locations away from the hub (fig. 32). Thus the majority of the losses in the hub region are thought to be due to three-dimensional effects for all three designs.

Summary of Results

The design system utilized, the design itself, and the steady-state aerodynamic performance of a fan stator row for a transonic single-stage fan with controlled diffusion (CD) blade sections were presented. Comparisons were made with the originally designed and tested double-circular-arc (DCA) stator row which had twice the number of blades of equal chord. In addition to the radially detailed traverse data upstream and downstream of the rotor and stator, chordwise distributions of surface Mach numbers from static taps on the CD stator at 10-, 50-, and 90-percent spans were also presented. The following principal results were obtained from this study:

1. The two-dimensional performances of the CD and DCA stators were similar with minimum loss coefficients of about

---

[1] The inner (hub-) end of stator 67B was machined, incorrectly, to the same profile (in the axial-radial plane) as that for stator 67. This resulted in a larger than intended clearance space over the forward half chord (between the end of stator 67B and the inner wall). The greater camber over the forward chord of stator 67B compared with stator 67 (see fig. 13) caused the mismatch. The stator hub-end clearance was about 1.4 percent of span (0.178 cm) at the leading edge of stator 67B, tapering down to about 0.2 percent span (0.025 cm) at midchord. This later clearance was continued from midchord to the trailing edge. This hub-end excess clearance is not believed to be a significant factor in the aerodynamic performance of stator 67B, but is described here for completeness of the study record.

0.030, except in the one-third span near the hub. In that region, the CD stator losses were much higher because of increased end-wall effects. Attaining the low two-dimensional loss performance with the CD blade sections under study required a strong, favorable pressure gradient on the suction surface to about 35- to 40-percent chord.

2. Because of higher hub region losses, the CD stator efficiency drop (rotor minus stage efficiency, overall) was about one percentage point higher than for the DCA stator at speeds from 90 to 100 percent of design. Stage stall flows were unchanged by stator design.

3. Accurate prediction of Mach numbers and air angles at different spanwise locations, which are required boundary value inputs to some of the analysis codes in the present design and analysis system are dependent on realistic flow blockage allowance inputs.

Lewis Research Center
National Aeronautics and Space Administration
Cleveland, Ohio, November 9, 1988

Appendix A
Symbols

A_{an} annulus area at rotor leading edge, m^2

ΔA_{an} incremental annulus area, m^2

A_f frontal area at rotor leading edge, m^2

a_a stagnation speed of sound, m/sec

C aerodynamic, chord, cm

C_p static pressure coefficient, eq. (B22)

C_x axial projection of aerodynamic chord, cm

c_p specific heat at constant pressure, 1004 J/kg K

D diffusion factor

H_i incompressible form factor, δ^*/θ'

i_{ss} incidence angle to suction surface at leading edge, eq. (B2)

i_{mc} incidence angle to mean line at leading edge, eq. (B1)

M Mach number

m meridional streamline distance, cm

N rotative speed, rpm

NR number of radial locations where measurements of flow conditions are made

N_D design rotative speed, 16 045 rpm

n tangential distance, cm

P total pressure, N/cm^2

p static pressure, N/cm^2

r radius, cm

s path distance on blade-element layout cone, cm

T total temperature, K

U wheel speed, m/sec

V velocity, m/sec

w equivalent weight flow, kg/sec, $(w\sqrt{\theta}/\delta)$

w_{choke} equivalent weight flow of choked value at design speed, kg/sec, $(w_{choke}\sqrt{\theta}/\delta)$

w_D design equivalent weight flow, 34.56 kg/sec, $(w_D\sqrt{\theta}/\delta)$

x axial distance, cm

z axial distance from rotor hub leading edge, cm (see fig. 2)

α_c cone angle, deg

α_s slope of streamline, deg

β air angle, angle between air velocity and axial direction, deg

β_c relative meridonal flow angle based on cone angle, arctan $(\tan \beta_r \cos \alpha_c /\cos \alpha_s)$, deg

γ ratio of specific heats (1.40)

δ ratio of rotor-inlet total pressure to standard pressure of 10.13 N cm^2

δ° deviation angle from mean line at trailing edge, eq. (B3)

δ^* boundary layer displacement thickness

η efficiency

$\Delta\eta$ overall rotor minus stage efficiency (stator efficiency drop)

θ ratio of rotor-inlet total temperature to standard temperature of 288.2 K.

θ' boundary layer momentum thickness

κ local angle of blade mean line with respect to the meridional direction, deg

κ_{mc} angle between blade mean camber line and meridional plane, deg

κ_{ss} angle between blade suction-surface and meridional plane, deg

ρ density, kg/m^3

σ solidity, ratio of chord to spacing

$\bar{\omega}$ total-loss coefficient

$\bar{\omega}_p$ profile-loss coefficient

$\bar{\omega}_s$ shock-loss coefficient

$\bar{\omega}_w$ wake total-loss coefficient where $(P'_{id})_{TE}$ (see eq. (B5)), is average of three highest total pressures measured across the stator gap

Subscripts:

ad adiabatic

c blade-element centerline on layout cone

h hub

id ideal

LE blade leading edge

m meridional direction

mom momentum rise

p polytropic

s surface of stator blade

TE blade trailing edge

t tip

z axial direction

θ tangential direction

1 instrumentation plane upstream of rotor (see fig. 2)

2 instrumentation plane between rotor and stator (see fig. 2)

3 instumentation plane downstream of stator (see fig. 2)

Superscript:

$'$ relative to blade

Appendix B
Equations

Mean incidence angle

$$i_{mc} = (\beta_c')_{LE} - (\kappa_{mc})_{LE} \qquad \text{(B1)}$$

Suction-surface incidence angle

$$i_{ss} = (\beta_c')_{LE} - (\kappa_{ss})_{LE} \qquad \text{(B2)}$$

Deviation angle

$$\delta^\circ = (\beta_c')_{TE} - (\kappa_{mc})_{TE} \qquad \text{(B3)}$$

Diffusion factor

$$D = 1 - \frac{V_{TE}'}{V_{LE}'} + \left| \frac{(rV_\theta)_{TE} - (rV_\theta)_{LE}}{(r_{TE} + r_{LE})\sigma(V_{LE}')} \right| \qquad \text{(B4)}$$

Total-loss coefficient

$$\overline{\omega} = \frac{(P_{id}')_{TE} - \overline{P}_{TE}'}{P_{LE}' - p_{LE}} \qquad \text{(B5)}$$

Profile-loss coefficient

$$\overline{\omega}_p = \overline{\omega} - \overline{\omega}_s \qquad \text{(B6)}$$

Total-loss parameter

$$\frac{\overline{\omega} \cos (\beta_c')_{TE}}{2\sigma} \qquad \text{(B7)}$$

Profile-loss parameter

$$\frac{\overline{\omega}_p \cos (\beta_c')_{TE}}{2\sigma} \qquad \text{(B8)}$$

Rotor total-pressure ratio

$$\overline{(P_2/P_1)} = \left[\frac{\int_{r_h}^{r_t} (P_2/P_1)^{(\gamma-1)/\gamma} \rho V_z r \, dr}{\int_{r_h}^{r_t} \rho V_z r \, dr} \right]^{\gamma/(\gamma-1)}$$

$$= \left[\frac{\sum_{i=1}^{NR} (P_2/P_1)_i^{(\gamma-1)/\gamma} \rho_{2,i} V_{z2,i} \Delta A_{an,2,i}}{\sum_{i=1}^{NR} \rho_{2,i} V_{z2,i} \Delta A_{an,2,i}} \right]^{\gamma/(\gamma-1)} \qquad \text{(B9)}$$

Stage total-pressure ratio

$$\overline{(P_3/P_1)} = \left[\frac{\int_{r_h}^{r_t} (P_3/P_1)^{(\gamma-1)/\gamma} \rho V_z r \, dr}{\int_{r_h}^{r_t} \rho V_z r \, dr} \right]^{\gamma/(\gamma-1)}$$

$$= \left[\frac{\sum_{i=1}^{NR} (P_3/P_1)_i^{(\gamma-1)/\gamma} \rho_{3,i} V_{z3,i} \Delta A_{an,3,i}}{\sum_{i=1}^{NR} \rho_{3,i} V_{z3,i} \Delta A_{an,3,i}} \right]^{\gamma/(\gamma-1)} \qquad \text{(B10)}$$

Total temperature ratio

$$\overline{(T_2/T_1)} = \frac{\int_{r_h}^{r_t} (T_2/T_1)\, \rho V_z r\, dr}{\int_{r_h}^{r_t} \rho V_z r\, dr}$$

$$= \frac{\sum\limits_{i=1}^{NR} (T_2/T_1)\, \rho_{2,i} V_{z2,i}\, \Delta A_{an,2,i}}{\sum\limits_{i=1}^{NR} \rho_{2,i} V_{z2,i}\, \Delta A_{an,2,i}} \qquad (B11)$$

Rotor adiabatic efficiency

$$\eta_{ad} = \frac{(\overline{P_2/P_1})^{(\gamma-1)/\gamma} - 1}{(\overline{T_2/T_1}) - 1} \qquad (B12)$$

Stage adiabatic efficiency

$$\eta_{ad} = \frac{(\overline{P_2/P_1})^{(\gamma-1)/\gamma} - 1}{(\overline{T_3/T_1}) - 1} \qquad (B13)$$

Rotor-inlet mass averaged temperature

$$(\overline{T_1}) = \frac{\int_{r_h}^{r_t} T_1\, \rho V_z r\, dr}{\int_{r_h}^{r_t} \rho V_z r\, dr} = \frac{\sum\limits_{i=1}^{NR} T_{1,i}\, \rho_{1,i} V_{z1,i}\, \Delta A_{an,1,i}}{\sum\limits_{i=1}^{NR} \rho_{1,i} V_{z1,i}\, \Delta A_{an,1,i}}$$

$$(B14)$$

Momentum-rise efficiency

$$\eta_{mom} = \frac{(\overline{P_2/P_1})^{(\gamma-1)/\gamma} - 1}{\dfrac{\int_{r_h}^{r_t} \left[(UV_\theta)_2 - (UV_\theta)_1\right] \rho V_z r\, dr}{\overline{T_1} C_p}}$$

$$= \frac{(\overline{P_2/P_1})^{(\gamma-1)/\gamma} - 1}{\dfrac{\sum\limits_{i=1}^{NR} \left[(UV_\theta)_2 - (UV_\theta)_1\right] \rho_{2,i} V_{z2,i} \Delta A_{2,i}}{\overline{T_1} C_p}} \qquad (B15)$$

Head-rise coefficient

$$\frac{c_p \overline{T_1}}{U_t^2} \left[(\overline{P_2/P_1})^{(\gamma-1)/\gamma} - 1 \right] \qquad (B16)$$

Equivalent weight flow

$$\frac{w\sqrt{\theta}}{\delta} \qquad (B17)$$

Equivalent rotative speed

$$\frac{N}{\sqrt{\theta}} \qquad (B18)$$

Weight flow per unit annulus area

$$\frac{\dfrac{w\sqrt{\theta}}{\delta}}{A_{an}} \qquad (B19)$$

Weight flow per unit frontal area

$$\frac{\dfrac{w\sqrt{\theta}}{\delta}}{A_f}$$

(B20)

Flow coefficient

$$\left(\frac{V_z}{U_t}\right)_{LE}$$

(B21)

Stator surface static pressure coefficient

$$C_p = \frac{P_s - P_2}{\dfrac{\gamma - 1}{2} P_2 M_2^2}$$

(B22)

Stator surface Mach number

$$M_s = \sqrt{\frac{2}{\gamma - 1}\left[\left(\frac{P_s}{p_s}\right)^{\frac{\gamma-1}{\gamma}} - 1\right]}$$

(B23)

(with P_s assumed equal to P_2 at appropriate spanwise location)

Appendix C
Abbreviations and Units Used in Tables

ABS	absolute
BETAM	meriodional air angle, deg
DEV	deviation angle (defined by eq. (B3)), deg
D-FACT	diffusion factor (defined by eq. (B4))
EFF	adiabatic efficiency (defined by eq. (B12) or (B13))
IN	inlet (leading edge of blade)
INCIDENCE	incidence angle (suction surface defined by eq. (B2), and mean by eq. (B1)), deg
KIC	angle between blade mean camber line at leading edge and meridional plane, deg
KOC	angle between blade mean camber line at trailing edge and meridional plane, deg
LOSS COEFF	loss coefficient (total defined by eq. (B5), profile by eq. (B6))
LOSS PARAM	loss parameter (total defined by eq. (B7), profile by eq. (B8))
MERID	meridional
MERID VEL R	meriodional velocity ratio

OUT	outlet (trailing edge of blade)
PERCENT SPAN	percent of blade span from tip at rotor trailing edge for design streamlines
PRESS	pressure, N/cm^2
PROF	profile
RADII	radius, cm
REL	relative to blade
RP	radial position
RPM	equivalent rotative speed, rpm (defined by eq. (B18))
SOLIDITY	ratio of aerodynamic chord to blade spacing
SPEED	speed, m/sec
SS	suction surface
TANG	tangential
TEMP	temperature, K
TOT LOSS COEFF WAKE	equation (B5) with $(P_{id})_{TE}$ equal to average of three highest total pressures measured across the stator gap
TOT	total
VEL	velocity, m/sec

17

Appendix D
Description of Codes in the Design and Analysis System

Several two- and quasi-three-dimensional inviscid codes and a two-dimensional integral boundary-layer code are utilized in the present design and analysis system. Brief descriptions are presented here; further details are in the cited references. These descriptions are grouped under subtitles of Hub-To-Tip Codes, Blade-To-Blade Codes, and Boundary-Layer Code. Code names used on figure 1 and in the text are also identified.

Hub-To-Tip Codes

CDP.—This Compressor Design Program developed by Crouse and Gorrell (ref. 15) does a hub-to-tip aerodynamic flow field calculation and also computes the associated blade geometry to satisfy the required velocity diagrams at the blade edges. As developed, the flow solutions are applicable for calculation stations outside the blade rows and at the blade edges, but not inside the blade rows. The streamline curvature method is used for the iterative aerodynamic solution. Inputs to the CDP can be classified into two groups: general information and calculation station and blade row information. A number of parameters are input to specify and control the blade row aerodynamics and geometry. Also, a number of different input and output options are available.

The geometry of each blade element or blade section in the CDP is specified as follows: The mean line of the blade is described by two polynomial segments, each of which can be specified by up to a fourth degree polynomial. The polynomial is a fit of local mean-line blade angles in terms of mean-line distance. The fraction of chord from the leading edge at which the two polynomial segments join is called the transition location. The distribution of blade thickness about the mean line is also specified by two polynomials, both of which may be up to fourth degree. The thickness is added symmetrically to each side of the mean line as the term implies. The fit is made from the maximum thickness location toward the leading and trailing edges for front and rear segments, respectively. The maximum thickness location is independent of the transition location and both are specified. The leading and trailing edges of the blade are specified as either circles or ellipses. Finally each polynomial coefficient in the CDP is defined across all blade elements with a third degree polynomial function of annulus height. The entire blade is evolved in the CDP by stacking all of the gradually changing blade elements on a radial line.

The output from the aerodynamic solution of the CDP has an overall blade row and compressor performance summary followed by blade element parameters for the individual blade rows. Blade coordinates in the streamwise direction for subsequent use in analysis codes can be printed and stored. Also, blade coordinates on horizontal plans for fabrication purposes can be similarly obtained.

BEP.—This Blade Element Program (unpublished) has been extracted from the compressor design program (CDP) for convenience in designing the geometry of the individual blade elements or sections that make up the blade from hub-to-tip. The inputs to the BEP are the same as those previously described for the blade section geometry portion of the CDP. This blade element code has been expanded with a graphics package such that points can be input on a cathode ray tube and curve fitted. Thus blade angle and blade thickness distributions can be immediately displayed and modified. The curve fit coefficients that are inputs to the CDP are also made available from this graphics process.

CURVFIT.—This is a simple auxiliary code that radially curve fits geometric or aerodynamic values obtained from selected blade element designs generally made near the hub, mean, and tip. CURFIT provides the required radial distributions of input for either CDP or MERIDL.

MERIDL.—This analysis code developed by Katsanis and McNally (ref. 16) provides a hub-to-tip solution of the flow on a midchannel stream surface of a turbomachinery blade row. The MERIDL code solves the stream function equation by finite difference techniques for subsonic, compressible flow. It calculates the flow through the blade row and is used here primarily to provide the stream-tube convergence and radius change for subsequent blade-to-blade analyses. The required geometric inputs are the annulus profile coordinates and the blade section geometry from hub-to-tip including, as desired, blockage effects of boundary-layer displacement thicknesses, δ^*. The blade section metal geometry is obtained by the CDP while δ^* is obtained from a subsequently described boundary-layer code, BLAYER (ref. 19).

The required aerodynamic inputs to MERIDL are the weight flow, the radial distribution of blade relative values of inlet total temperature, inlet and outlet total pressure, and inlet and outlet tangential velocity or whirl (rV_θ). These inputs are obtained from the CDP. As used here, the midchannel stream surface in MERIDL is specified a little differently than in reference 16. The total air turning from the CDP is distributed from leading to trailing edge at the same rate as the change in mean camber line. This assumption replaces the one in reference 16 where transition surfaces near the leading and trailing edges were blended into the mean camber line shape as an arbitrary function of blade solidity. The most appropriate description of this midchannel surface awaits the analysis of detailed measurements taken within a variety of blade rows and for a range of speeds and flows.

Blade-To-Blade Codes

TSONIC.—This quasi-three-dimensional flow analysis code developed by Katsanis (ref. 17) calculates the subsonic flow.

and with an approximate scheme slightly supersonic ($M_s < 1.1$ approx.) flow about selected blade elements generally near the hub, mean, and tip. The code solves the stream function equation by finite difference techniques for subsonic, compressible flow. Input of the blade geometry is required and in the present study, it included the blockage effects of the boundary-layer displacement thickness δ^* described later. Approximations of some of the real three-dimensional flow effects in a turbomachinery blade row also were made in TSONIC by correcting its basically two-dimensional blade-to-blade flow for radius change and stream-tube convergence in the throughflow direction. Radius change and stream-tube height distribution were calculated by and obtained directly from MERIDL for the stream surfaces of interest. Other required aerodynamic inputs are the weight flow, the inlet total temperature and density, the inlet and outlet flow angles relative to the blade, and total pressure loss across the blade. These inputs were generally obtained from MERIDL solutions and were directly transferable to the TSONIC code.

A mass injection model at the blade section trailing edge has been incorporated in TSONIC (unpublished addendum to ref. 17). It simulates the blade wake and reduces the sensitivity of the surface velocity calculation in the trailing edge region. The mass was injected uniformly with the amount set equal to the percent physical blockage at the blade trailing edge, including the boundary-layer displacement thicknesses (δ^*) there. The simulated wake is extended downstream with an orientation determined by downstream whirl boundary conditions. Angular momentum is conserved in this region. An illustration of this mass injection model in TSONIC was presented by Sanger in reference 22.

The TSONIC code with trailing edge injection was also utilized to predict the exit air angle at each blade section. Usually, exit air angles are estimated from deviation angle prediction methods like Carter's rule (see ref. 25).

Such deviation rules are based on correlations of experimental data from different blade shapes. Generally some boundary-layer separation from the suction surface is present and the variety of blade shapes tested has been somewhat limited. In the present study, the blade section geometry is different from that previously tested and the design intent was to avoid any blade boundary layer separation. For these reasons a different method of estimating the blade exit air angle (required input to TSONIC) was used as follows:

The blade exit air angle was selected to result in TSONIC code calculated suction and pressure surface velocities that were equal right at the trailing edge. Limited comparisons using this technique for estimating exit air angle with low loss experimental data are illustrated in the following table. In general there was agreement within 1.5° or less.

Name	Percent span from tip	Solidity	Total camber, deg	Mach number, M_{LE}	Ref.	Air angles, deg		
						Measured	Calc.	$\Delta\beta_{TE}$
						β_{LE}	β_{TE}	β_{TE}	
Rotor 28 D	10	1.38	21.2	0.82	21	60.7	49.1	49.4	-0.3
Stator 67	50	1.68	46.2	.72	10	35.1	-.4	-1.9	+1.5
Stator 59 D	50	1.90	42.0	.79	24	35.6	.4	-1.1	+1.5

To obtain the quasi-three-dimensional flow solutions desired, the selected exit air angles for TSONIC that close the surface velocity diagram at the trailing edge should agree at all spanwise sections with those calculations by the CDP and MERIDL. Thus the downstream (rV_θ) whirl input required for these codes was adjusted until the hub-to-tip and blade-to-blade codes agreed on these exit air angles.

The output of TSONIC provided the subsonic blade surface velocities and the exit air angle on the selected stream surfaces. For supersonic surface velocities and a better definition of surface velocities in the leading edge region, another blade-to-blade analysis code was used and is described next.

QSONIC.—This quasi-three-dimensional flow analysis code developed by Farrell (ref. 18) is a fully conservative solution of the full potential equation. It uses the finite volume technique on a body-fitted periodic mesh. Artificial density is imposed in transonic regions to insure stability and capture of any shock waves. Corrections for radius change and stream-tube convergence were also included in the QSONIC solution as they were in TSONIC. In QSONIC, peak local relative Mach numbers should be less than about 1.4 to satisfy the isentropic flow assumption. Any discontinuities (shocks) are assumed weak enough to be approximated as isentropic jumps.

The finer, body-fitted mesh of QSONIC is better than the relatively coarse and nominally square mesh of TSONIC in defining the surface velocities in the leading edge region. However in the trailing edge region, the TSONIC solutions with its trailing edge mass injection modeling were used. There is no comparable modelling available in the QSONIC code and without it the trailing edge velocities calculated by QSONIC are generally erratic and unrealistic (fig. 9 and ref. 18). The TSONIC and QSONIC calculations of the blade surface velocities generally were in close agreement when the values were subsonic and removed from the leading or trailing edge by about 5 percent of chord (fig. 9). As elsewhere illustrated and discussed, the final description of surface velocities was a composite of TSONIC and QSONIC results. QSONIC results were favored near the leading edge and in

supersonic flow regions while TSONIC results were followed in approaching the trailing edge.

Boundary-Layer Code, BLAYER

Blade surface boundary layers were calculated from a program developed by McNally (BLAYER, ref. 19). The code uses integral methods to solve the two-dimensional compressible laminar and turbulent boundary-layer equations in an arbitrary pressure gradient. As described in reference 19, Cohen and Reshotko's method was used for the laminar boundary layer; transition was predicted by the Schlicting-Ulrich-Granville method; and Sasman and Cresci's method was used for the turbulent boundary layer.

A boundary layer that is initially laminar may proceed through normal transition to a turbulent boundary layer, or it may undergo some form of laminar separation before becoming turbulent. If laminar separation was predicted before transition, as were all cases studied here, the turbulent calculation may be started by specifying the momentum thickness and form factor as initial values. These initial values were obtained by using the laminar separation bubble modelling of Roberts (ref. 20). Knowing the inviscid surface velocity distribution, the Robert's model calculates the bubble size and the momentum thickness of the starting turbulent boundary layer, and the form factor there is specified. Turbulent boundary layer separation was assumed to occur when the incompressible form factor H_i exceeded 2.0, a rather conservative value.

The boundary layer displacement thickness δ^* along both the suction and pressure surface is an output of BLAYER. This δ^* was added normal to the local blade metal geometry from the BEP to establish the blade input geometry for subsequent TSONIC or QSONIC analysis. This modified metal geometry was also the input for MERIDL to account for blade boundary-layer blockage effects.

Appendix E
Flow Blockage Allowances

As previously indicated (see the section Aerodynamic Designs, Stator 67B) no explicit flow blockage allowances were utilized in the design of stator 67B. Instead, fairings of the design inputs (like total temperature and pressure, and tangential velocity, figs. 3 and 4), to the walls were assumed adequate to account for flow blockage effects. This was an incorrect assumption as was shown by the measured performance of stator 67B near design flow. The meridional Mach numbers at the inlet and outlet of stator 67B were significantly higher than design in figures 21(e) and 22(e), respectively. These higher meridional Mach numbers, in turn, caused lower than design inlet air angles (fig. 21(c)).

To illustrate the effects of explicit wall blockage allowances on some of the key design parameters, design simulations from the compressor design program (CDP) with and without such allowances were calculated. These were then compared to experimental results from stage 67B (stator 67B operating with rotor 67) near peak stage efficiency on figures 45 to 47.

In each of the figures 45 to 47, radial profiles of total pressure are shown in part (a), static pressure in part (b), air angle in part (c), and absolute, meridional, and tangential Mach numbers in parts (d), (e), and (f), respectively. Also, figures 45, 46, and 47, are for measuring stations 1, 2, and 3 respectively. The wall blockage allowances utilized to produce the results on figures 45 to 47 came from figures 48 and 49. It is figure 48 that illustrates the method of determining tip and hub blockage allowances from displacement thicknesses δ^* for the annular flow passage at the three measuring stations. First the core flow data points at each station are extrapolated to the walls by the assumed curve shown. Then δ^* is that location which results in the integral of $2\pi r\rho V_x dr$ between δ^* and the wall being equal to that between δ^* and the extrapolated core flow profile. This precedure is illustrated by the equal cross-hatched areas above and below δ^* at each wall and measuring station (fig. 48). These δ^* values in terms of an annular area fraction of total (i.e., blockage allowance) are given on figure 48 and plotted on figure 49.

The blockage allowances for the outer wall on figures 48 and 49 at stations 1 and 2 are within 10 percent of those determined in reference 26 for the same rotor and flow but from a more complex procedure. The outer wall blockage allowance at station 3, 0.027, is about 60 percent higher with stator 67B than that determined for stator 67 in reference 26. The different stator designs contributed to this difference in blockage. There were no measurements near the inner (hub) wall in the reference 26 studies, so no comparisons with the present stator 67B data are possible there.

At the rotor inlet, the measured meridional (same as absolute) Mach number profile near design flow and from about 20- to 80-percent span is about 5 percent higher than the design intent based on the CDP simulation with blockage

allowances of zero (i.e., no change to flow path radii). (See fig. 45(d).) However, with tip and hub blockage allowances (from figs. 48 and 49) applied in the form of changed flow path radii, the redesign simulation is in good agreement with the measured data in terms of Mach number profiles. Note that the total pressure profiles input to the design are the same as the experimental data at the three measuring stations (figs. 45(a), 46(a), and 47(a)). The differences in Mach number between the designs and the data are due to the different static pressure profiles (part (b) of figs. 45 to 47) which in turn are dependent on the blockage allowances as indicated in the figures.

At the stator inlet, the meridional Mach number profile with the wall blockage allowances from figure 48 is a closer match to the experimental data than with zero blockage (fig. 46(e)). However the measured values are still a few percent higher than design. We think that the additional blockage required for a match between design and data is the result of nonaxisymmetric phenomena like blade wakes, tip leakage, corner stalls, etc. These so-called tangential blockages, some of which occur across the total span, and their role in the total effective blockage to the flow through axial compressors is illustrated and discussed by Dring in reference 27.

The tangential Mach number profile at the stator inlet is input to the simulation, thus agreement with data is given there (fig. 46(f)). The relatively small differences in absolute Mach number (fig. 46(d)) and air angle (fig. 46(c)) between the data and the simulation with wall blockage from figures 48 and 49 stem from the different meridional Mach numbers (fig. 46(e)) previously discussed. Without any wall blockage allowances, the stator inlet simulations for Mach number were about 5 percent low (fig. 46(d)), and for air angle, 2° to 5° high (fig. 46(c)).

At the stator outlet (fig. 47(d)) the measured meridional (same as absolute) Mach number profile even with the wall blockage allowances from figure 48, is about 5 percent higher than the simulation in the CDP over the inner two-thirds of the span. Again, we think the additional blockage allowance required for a match between simulation and data is the result of nonaxisymmetric phenomena. At station 3 stator wake profiles were measured. From a total span integration of these wake data from the near-wall data series near design flow, an additional blockage allowance of 0.015 was determined. Although not shown here, this additional blockage, applied half at the tip and half at the hub of station 3, further improves the agreement between the design simulation and data. Only a couple of percent difference in Mach number profiles remain after adding the blockage due to wakes to the wall blockage allowances of figure 48.

We conclude from this discussion of flow blockage and that in reference 27, that two types are involved. One is related

to the axisymmetric flows along the inner and outer walls. This type of blockage can be determined as shown on figure 48. The other source of blockage is from nonsymmetrical flows that can occur not only near the walls but across the span. This source was demonstrated in reference 27 with detailed data from blade wake measurements for a particular rotor. Unfortunately, such data are a function of roto. or stator design and also of axial location. Thus experimental results from a variety of designs are needed for reliable estimates in any future designs.

We also conclude that realistic flow blockage allowances are required if accurate predictions of Mach numbers and air anɡ.es at different spanwise locations are to be close to the design intent. These conditions are required boundary value inputs to some of the analysis codes in the present design and analysis system. It is not sufficient to apply mass averaged inputs of total pressure, tangential velocity, air angles, and others from measured data to through flow analyses like the CDP or MERIDL. (See app. D.)

Appendix F
Spanwise Distributions of Pressures, Mach Numbers, and Air Angles from Near-Wall Data Series

Results from the near-wall data series for three levels of flow at design speed are presented in figures 50 to 52 for measuring stations 1 to 3. respectively. The design intent conditions across stator 67B are also indicated on figures 51 and 52.

In each of the figures 50 to 52, total pressure is shown in part (a), static pressure in part (b), air angle in part (c), and absolute, meridional, and tangential Mach numbers in parts (d), (e), and (f), respectively. Only the near-wall conditions will be discussed here since those over the rest of the span were previously discussed with figures 21 to 24.

At the rotor inlet (station 1) the wall boundary layers indicated by the meridional Mach number profiles (fig. 50(d)) extended to about 5-percent span from each end. At the stator inlet (station 2) the boundary-layer thickness on the outer wall increased to about 10-percent span but remained at about 5 percent near the hub (fig. 51(e)). These results were independent of flow ratio. At the stator outlet (station 3), the outer and inner wall boundary-layer thicknesses were not well defined for the near peak-stage efficiency flow ratio of about 0.992 (fig. 52(e)). However, as the flow was throttled to ratios near 0.945 or 0.916, the outer wall boundary layer appeared thinner at the outlet than at the inlet of the stator.

The air angles measured at the rotor inlet (fig. 50(c)) were within 1° of zero across the span as expected. At the stator inlet (fig. 51(c)), the air angles decreased nearly 15° from the outer wall to 10-percent span. Also, there were over 5° decreases from the inner wall to 95-percent span. These rapid changes in stator inlet air angle occured within the wall boundary-layer thicknesses previously indicated. At the stator outlet (fig. 52(c)), the air angles within the outer wall boundary layer increased nearly 5° from the wall to 5-percent span. An increase of about 12° occurred from the inner wall to about 85-percent span from the tip. Inner wall boundary-layer thickness was not clearly defined in this region. However in this hub region, the stator outlet air is overturned very near the wall. That overturning changes to increasing degrees of underturning from about 97- to 85-percent span. This is a classic profile illustrating the effects of secondary flows near the wall (ref. 28).

Data from the near-wall series were also used to determine, for future reference, some flow blockage allowances. Details of these determinations are discussed in appendix E.

References

1. Behlke, R.F.: The Development of a Second Generation of Controlled Diffusion Airfoils for Multistage Compressors. J. Turbomachinery, vol. 108, no. 1, July 1986, pp. 32–41.

2. Bauer, F.; Garabedian, P.R.; and Korn, D.: Supercritical Wing Sections. Vol. I, II, and III, Springer-Verlag, 1972, 1975, 1977.

3. Stephens, H.E.: Application of Supercritical Airfoil Technology to the Compressor Cascades. AIAA Paper 78-1138, July 1978.

4. Rechter, H.; Schimming, P.; and Starken, H.: Design and Testing of Two Supercritical Compressor Cascades. ASME Paper 79-GT-11, Mar. 1979.

5. Boldman, D.R.; Buggele, A.E.; and Shaw, L.M.: Experimental Evaluation of Shockless Supercritical Airfoils in Cascade. AIAA Paper 83-0003, Jan. 1983. (NASA TM-83045).

6. Schmidt, J.F.; Gelder, T.F.; and Donovan, L.F.: Redesign and Cascade Tests of a Supercritical Controlled Diffusion Stator Blade-Section. AIAA Paper 84-1207, June 1984. (NASA TM-83635).

7. Behlke, R.F.; Brooky, J.D.; and Canal, E.: Study of Controlled Diffusion Stator Blading. (PWA-5698-77, Pratt & Whitney Aircraft Group; NASA Contract NAS3-22008) NASA CR-167995, 1983.

8. Sanz, J.M., et al.: Design and Performance of a Fixed, Nonaccelerating Guide Vane Cascade That Operates Over an Inlet Flow Angle Range of 60 Deg. J. Eng. Gas Turbines Power, vol. 107, no. 2, Apr. 1985, pp. 477–484.

9. Gelder, T.F., et al.: Wind Tunnel Turning Vanes of Modern Design. AIAA Paper 86-0044, Jan. 1986. (NASA TM-87146).

10. Urasek, D.C.; Gorrell, W.T.; and Cunnan, W.S.: Performance of Two-Stage Fan Having Low-Aspect-Ratio, First-Stage Rotor Blading. NASA TP-1493, 1979.

11. Suder, K.L., et al.: Measurements of the Unsteady Flow Field Within the Stator Row of a Transonic Axial Flow Fan. I—Measurement and Analysis Technique. ASME Paper 87-GT-226, June 1987. (NASA TM-88945.)

12. Hathaway, M.D., et al.: Measurements of the Unsteady Flow Field Within the Stator Row of a Transonic Axial Flow Fan. II—Results and Discussion. ASME Paper 87-GT-227, June 1987. (NASA TM-88946.)

13. Strazisar, A.J.: Investigation of Flow Phenomena in a Transonic Fan Rotor Using Laser Anemometry. J. Eng. Gas Turbines Power, vol. 107, no. 2, Apr. 1985, pp. 427–435.

14. Pierzga, M.J.; and Wood, J.R.: Investigation of the Three-Dimensional Flow Field Within a Transonic Fan Rotor: Experiment and Analysis. J. Eng. Gas Turbines Power, vol. 107, no. 2, Apr. 1985, pp. 436–449.

15. Crouse, J.E.; and Gorrell, W.T.: Computer Program for Aerodynamic and Blading Design of Multistage Axial-Flow Compressors. NASA TP-1946, 1981.

16. Katsanis, T.; and McNally, W.D.: Revised FORTRAN Program for Calculating Velocities and Streamlines on the Hub-Shroud Midchannel Stream Surface of an Axial, Radial, or Mixed-Flow Turbomachine or Annular Duct. I: Users Manual. NASA TN D-8430, 1977.

17. Katsanis, T.: FORTRAN Program for Calculating Transonic Velocities on a Blade-to-Blade Stream Surface of a Turbomachine. NASA TN D-5427, 1969.

18. Farrell, C.A.: Computer Program for Calculating Full Potential Transonic, Quasi-Three-Dimensional Flow Through a Rotating Turbomachinery Blade Row. NASA TP-2030, 1982.

19. McNally, W.D.: FORTRAN Program for Calculating Compressible Laminar and Turbulent Boundary Layers in Arbitrary Pressure Gradients. NASA TN D-5681, 1970.

20. Roberts, W.B.: The Effect of Reynolds Number and Laminar Separation on Axial Cascade Performance. J. Eng. Power, vol. 97, no. 2, Apr. 1975, pp. 261–274.

21. Britsch, W.R.; Osborn, W.M.; and Laessig, M.R.: Effects of Diffusion Factor, Aspect Ratio, and Solidity on Overall Performance of 14 Compressor Middle Stages. NASA TP-1523, 1979.

22. Sanger, N.L.: The Use of Optimization Techniques to Design Controlled-Diffusion Compressor Blading. ASME Paper 82-GT-149, Apr. 1982. (NASA TM-82763).

23. Stephens, H.E.; and Hobbs, D.E.: Design and Performance Evaluation of Supercritical Airfoils for Axial Flow Compressors. PWA-FR-11455, Pratt & Whitney Aircraft, June 1979. (Avail. NTIS, AD-A071206.)

24. Gelder, T.F.: Aerodynamic Performances of Three Fan Stator Designs Operating With Rotor Having Tip Speed of 337 Meters per Second and Pressure Ratio of 1.54. I—Experimental Performance. NASA TP-1610, 1980.

25. Johnson, I.A.; and Bullock, R.O., eds.: Aerodynamic Design of Axial-Flow Compressors. NASA SP-36, 1965.

26. Ball, C.L.; Reid, L.; and Schmidt, J.F.: End-Wall Boundary Layer Measurements in a Two-Stage Fan. NASA TM-83409, 1983.

27. Dring, R.P.: Blockage in Axial Compressors. J. Eng. Gas Turbines Power, vol. 106, no. 3, July 1984, pp. 712–714.

28. Horlock, J.H.: Axial Flow Compressors. Butterworths Scientific Publications, London, England, 1958. p. 128.

TABLE I.- OVERALL PERFORMANCE FOR STAGE 67. 100 PERCENT
DESIGN SPEED. SI UNITS.

```
READING NUMBER                                        0392
ROTOR TOTAL PRESSURE RATIO . . . . . . . . . . . 1.643
STATOR TOTAL PRESSURE RATIO. . . . . . . . . . . 0.980
ROTOR TOTAL TEMPERATURE RATIO. . . . . . . . . . 1.168
STATOR TOTAL TEMPERATURE RATIO . . . . . . . . . 0.997
ROTOR ADIABATIC EFFICIENCY . . . . . . . . . . . 0.905
ROTOR MOMENTUM-RISE EFFICIENCY . . . . . . . . . 0.953
ROTOR HEAD-RISE COEFFICIENT. . . . . . . . . . . 0.280
FLOW  COEFFICIENT. . . . . . . . . . . . . . . . 0.436
AIRFLOW PER UNIT FRONTAL AREA. . . . . . . . . . 168.78
AIRFLOW PER UNIT ANNULUS AREA. . . . . . . . . . 196.43
AIRFLOW AT ORIFICE . . . . . . . . . . . . . . . 34.56
AIRFLOW, FRACTION OF CHOKED VALUE AT 100% N_D . . . . . 0.985
ROTATIVE SPEED . . . . . . . . . . . . . . . . . 16047.3
PERCENT OF DESIGN SPEED. . . . . . . . . . . . . 100.0
```

COMPRESSOR PERFORMANCE

```
STAGE TOTAL PRESSURE RATIO . . . . . . . . . . . 1.609
STAGE TOTAL TEMPERATURE RATIO. . . . . . . . . . 1.165
STAGE ADIABATIC EFFICIENCY . . . . . . . . . . . 0.884
```

TABLE II. - BLADE ELEMENT DATA AT BLADE EDGES FOR ROTOR 67. 100 PERCENT
DESIGN SPEED. SI UNITS. READING NUMBER 0392.

RP	RADII IN	RADII OUT	ABS BETAM IN	ABS BETAM OUT	REL BETAM IN	REL BETAM OUT	TOTAL TEMP IN	TOTAL TEMP RATIO	TOTAL PRESS IN	TOTAL PRESS RATIO
1	24.856	24.112	-0.0	43.3	66.3	60.9	288.7	1.205	9.94	1.645
2	24.145	23.467	-0.0	36.8	64.5	57.0	288.2	1.187	10.13	1.665
3	23.429	22.819	-0.0	34.4	63.2	55.6	288.2	1.177	10.16	1.664
4	21.245	20.881	-0.0	35.6	60.1	50.7	288.1	1.168	10.15	1.654
5	18.247	18.296	-0.0	38.1	56.1	41.6	288.1	1.159	10.15	1.630
6	13.343	14.417	-0.0	43.9	49.0	17.0	288.1	1.160	10.16	1.625
7	12.433	13.769	-0.0	45.5	47.5	11.1	288.1	1.159	10.17	1.623
8	11.478	13.124	-0.0	46.0	46.0	6.1	288.3	1.160	10.14	1.621
9	10.490	12.479	0.0	47.3	45.3	-0.3	288.3	1.161	10.05	1.657

RP	ABS VEL IN	ABS VEL OUT	REL VEL IN	REL VEL OUT	MERID VEL IN	MERID VEL OUT	TANG VEL IN	TANG VEL OUT	WHEEL SPEED IN	WHEEL SPEED OUT
1	183.6	203.6	457.1	304.7	183.6	148.1	-0.0	139.7	418.6	406.1
2	193.6	215.0	449.0	315.9	193.6	172.2	-0.1	128.8	405.0	393.6
3	199.8	217.6	442.9	317.7	199.8	179.6	-0.1	122.9	395.2	384.9
4	205.8	223.2	412.9	286.6	205.8	181.5	-0.1	129.9	357.8	351.7
5	206.6	234.2	370.2	246.3	206.6	184.3	-0.0	144.6	307.2	308.0
6	194.8	264.5	296.7	199.2	194.8	190.5	-0.0	183.5	223.7	241.7
7	190.8	271.2	282.6	193.6	190.8	190.0	-0.0	193.6	208.5	230.9
8	185.5	276.8	267.3	193.3	185.5	192.2	-0.1	199.3	192.3	219.9
9	174.4	286.5	247.9	194.1	174.4	194.1	0.0	210.7	176.2	209.6

RP	ABS MACH NO IN	ABS MACH NO OUT	REL MACH NO IN	REL MACH NO OUT	MERID MACH NO IN	MERID MACH NO OUT	MERID PEAK SS VEL R	PEAK SS MACH NO
1	0.555	0.561	1.383	0.840	0.555	0.408	0.807	1.524
2	0.588	0.600	1.364	0.882	0.588	0.481	0.889	1.515
3	0.608	0.611	1.349	0.892	0.608	0.504	0.899	1.509
4	0.628	0.631	1.260	0.810	0.628	0.513	0.882	1.444
5	0.631	0.667	1.131	0.702	0.631	0.525	0.892	1.389
6	0.592	0.763	0.902	0.574	0.592	0.549	0.978	1.289
7	0.579	0.785	0.858	0.560	0.579	0.550	0.996	1.211
8	0.562	0.802	0.810	0.560	0.562	0.557	1.036	1.122
9	0.526	0.834	0.748	0.565	0.526	0.565	1.113	1.035

RP	PERCENT SPAN	INCIDENCE MEAN	INCIDENCE SS	DEV	D FACT	EFF	LOSS COEFF TOT	LOSS COEFF PROF	LOSS PARAM TOT	LOSS PARAM PROF
1	5.00	1.7	-0.6	7.4	0.446	0.745	0.202	0.119	0.037	0.022
2	10.00	1.6	-0.8	4.0	0.400	0.839	0.123	0.045	0.024	0.009
3	15.00	1.4	-1.1	2.7	0.380	0.886	0.085	0.011	0.017	0.002
4	30.00	1.1	-1.6	2.0	0.407	0.923	0.060	0.010	0.012	0.002
5	50.00	1.9	-1.9	4.5	0.444	0.940	0.052	0.026	0.011	0.005
6	80.00	5.0	-2.1	9.2	0.464	0.932	0.082	0.080	0.017	0.016
7	85.00	4.8	-2.0	10.2	0.458	0.933	0.088	0.088	0.017	0.017
8	90.00	4.4	-1.9	12.4	0.425	0.923	0.111	0.111	0.021	0.021
9	0.00	4.8	-0.9	13.5	0.377	0.966	0.057	0.057	0.010	0.010

TABLE III. - BLADE ELEMENT DATA AT BLADE EDGES FOR STATOR 67. 100 PERCENT DESIGN SPEED. SI UNITS. READING NUMBER 0392.

RP	RADII IN	RADII OUT	ABS BETAM IN	ABS BETAM OUT	REL BETAM IN	REL BETAM OUT	TOTAL TEMP IN	TOTAL TEMP RATIO	TOTAL PRESS IN	TOTAL PRESS RATIO
1	23.774	23.779	40.1	2.0	40.1	2.0	347.9	0.990	16.36	0.990
2	23.198	23.228	33.6	2.1	33.6	2.1	342.1	0.999	16.87	0.970
3	22.611	22.662	31.3	1.0	31.3	1.0	339.1	0.999	16.90	0.981
4	20.836	20.950	32.4	0.3	32.4	0.3	336.3	1.000	16.79	0.992
5	18.456	18.682	35.1	-0.4	35.1	-0.4	333.9	0.997	16.55	0.985
6	14.778	15.278	42.3	1.5	42.3	1.5	334.1	0.994	16.51	0.972
7	14.150	14.717	44.5	2.2	44.5	2.2	333.9	0.996	16.50	0.974
8	13.518	14.155	45.6	1.8	45.8	1.8	334.5	0.997	16.45	0.961
9	12.883	13.597	48.1	-2.0	48.1	-2.0	334.7	0.997	16.66	0.922

RP	ABS VEL IN	ABS VEL OUT	REL VEL IN	REL VEL OUT	MERID VEL IN	MERID VEL OUT	TANG VEL IN	TANG VEL OUT	WHEEL SPEED IN	WHEEL SPEED OUT
1	219.9	163.1	219.9	163.1	168.1	163.0	141.7	5.8	0.0	0.0
2	235.2	171.0	235.2	171.0	195.8	170.9	130.3	6.2	0.0	0.0
3	238.9	177.7	238.9	177.7	204.2	177.6	124.0	3.1	0.0	0.0
4	242.6	185.7	242.6	185.7	204.7	185.7	130.1	0.8	0.0	0.0
5	249.1	180.8	249.1	180.8	203.8	180.8	143.3	-1.3	0.0	0.0
6	265.8	179.8	265.8	179.8	196.5	179.8	179.0	4.6	0.0	0.0
7	268.7	182.1	268.7	182.1	191.6	182.0	188.4	7.0	0.0	0.0
8	269.8	176.7	269.8	176.7	188.0	176.6	193.5	5.6	0.0	0.0
9	274.0	163.1	274.0	163.1	182.9	163.0	204.0	-5.8	0.0	0.0

RP	ABS MACH NO IN	ABS MACH NO OUT	REL MACH NO IN	REL MACH NO OUT	MERID MACH NO IN	MERID MACH NO OUT	HI3 TOT PRESS	TOTAL LOSS COEFF WAKE	MERID VEL R	PEAK SS MACH NO
1	0.610	0.447	0.610	0.447	0.466	0.447	16.43	0.066	0.970	1.057
2	0.661	0.471	0.661	0.471	0.551	0.471	16.62	.060	0.873	0.991
3	0.676	0.493	0.676	0.493	0.578	0.493	16.80	.050	0.870	0.944
4	0.690	0.519	0.690	0.519	0.583	0.519	16.82	.033	0.907	0.952
5	0.714	0.507	0.714	0.507	0.584	0.507	16.44	.030	0.887	0.984
6	0.767	0.505	0.767	0.505	0.567	0.504	16.28	.045	0.915	1.110
7	0.776	0.511	0.776	0.511	0.554	0.511	16.38	.057	0.950	1.152
8	0.779	0.494	0.779	0.494	0.543	0.494	16.31	.091	0.939	1.158
9	0.793	0.455	0.793	0.455	0.529	0.454	15.97	.110	0.891	1.204

RP	PERCENT SPAN	INCIDENCE MEAN	INCIDENCE SS	DEV	D FACT	EFF	LOSS COEFF TOT	LOSS COEFF PROF	LOSS PARAM TOT	LOSS PARAM PROF
1	5.00	5.4	-0.5	16.1	0.494	0.000	0.045	0.045	0.017	0.017
2	10.00	0.3	-5.7	14.0	0.469	0.000	0.117	0.117	0.043	0.043
3	15.00	-2.2	-8.2	11.8	0.440	0.000	0.073	0.073	0.026	0.026
4	30.00	-2.0	-7.8	9.6	0.412	0.000	0.029	0.029	0.010	0.010
5	50.00	-2.1	-7.8	8.2	0.446	0.000	0.053	0.053	0.016	0.016
6	80.00	-0.8	-6.1	11.1	0.478	0.000	0.088	0.088	0.021	0.021
7	85.00	-0.1	-5.3	12.6	0.474	0.000	0.080	0.080	0.019	0.019
8	90.00	-0.5	-5.6	13.5	0.495	0.000	0.117	0.117	0.026	0.026
9	0.00	-0.0	-5.0	11.2	0.562	0.000	0.230	0.230	0.049	0.049

TABLE IV. - OVERALL PERFORMANCE FOR STAGE 67B. 100 PERCENT
DESIGN SPEED. SI UNITS.

```
READING NUMBER                                              2609
ROTOR TOTAL PRESSURE RATIO . . . . . . . . . . . . 1.616
STATOR TOTAL PRESSURE RATIO. . . . . . . . . . . . 0.977
ROTOR TOTAL TEMPERATURE RATIO. . . . . . . . . . . 1.163
STATOR TOTAL TEMPERATURE RATIO . . . . . . . . . . 0.999
ROTOR ADIABATIC EFFICIENCY . . . . . . . . . . . . 0.899
ROTOR MOMENTUM-RISE EFFICIENCY . . . . . . . . . . 0.918
ROTOR HEAD-RISE COEFFICIENT. . . . . . . . . . . . 0.269
FLOW  COEFFICIENT. . . . . . . . . . . . . . . . . 0.446
AIRFLOW PER UNIT FRONTAL AREA. . . . . . . . . . . 169.41
AIRFLOW PER UNIT ANNULUS AREA. . . . . . . . . . . 196.97
AIRFLOW AT ORIFICE . . . . . . . . . . . . . . . . 34.70

AIRFLOW, FRACTION OF CHOKED VALUE AT 100% N_D . . . . 0.993
ROTATIVE SPEED . . . . . . . . . . . . . . . . . 16052.5
PERCENT OF DESIGN SPEED. . . . . . . . . . . . . . 100.1
```

COMPRESSOR PERFORMANCE

```
STAGE TOTAL PRESSURE RATIO . . . . . . . . . . . . 1.579
STAGE TOTAL TEMPERATURE RATIO. . . . . . . . . . . 1.162
STAGE ADIABATIC EFFICIENCY . . . . . . . . . . . . 0.858
```

TABLE V. - BLADE ELEMENT DATA AT BLADE EDGES FOR ROTOR 67.
100 PERCENT DESIGN SPEED. SI UNITS.   READING NUMBER 2609.

RP	RADII IN	RADII OUT	ABS BETAM IN	ABS BETAM OUT	REL BETAM IN	REL BETAM OUT	TOTAL TEMP IN	TOTAL TEMP RATIO	TOTAL PRESS IN	TOTAL PRESS RATIO
1	24.897	24.115	0.0	43.8	65.8	60.6	288.5	1.200	9.93	1.605
2	24.206	23.470	0.0	35.7	63.9	56.4	288.4	1.188	10.13	1.626
3	23.467	22.822	0.0	33.7	62.5	55.2	288.2	1.169	10.14	1.629
4	21.179	20.881	0.0	35.5	59.3	50.5	288.1	1.159	10.15	1.620
5	18.138	18.293	0.0	38.2	55.2	41.8	288.1	1.155	10.16	1.606
6	14.874	15.707	0.0	41.8	50.5	27.3	288.1	1.153	10.16	1.611
7	12.187	13.767	0.0	46.0	46.7	10.9	288.0	1.159	10.16	1.612
8	11.290	13.119	0.0	47.9	45.2	5.0	288.0	1.158	10.15	1.602
9	10.396	12.474	0.0	51.0	44.5	-5.1	288.5	1.164	10.01	1.658

RP	ABS VEL IN	ABS VEL OUT	REL VEL IN	REL VEL OUT	MERID VEL IN	MERID VEL OUT	TANG VEL IN	TANG VEL OUT	WHEEL SPEED IN	WHEEL SPEED OUT
1	187.4	205.3	457.9	301.6	187.4	148.2	0.0	142.1	417.8	404.7
2	199.4	218.4	452.8	320.4	199.4	177.3	0.0	127.4	406.6	394.2
3	205.2	219.0	444.4	319.3	205.2	182.3	0.0	121.4	394.4	383.5
4	211.5	223.7	414.2	286.7	211.5	182.2	0.0	129.7	356.1	351.1
5	211.8	232.7	371.1	245.4	211.8	182.9	0.0	143.8	304.7	307.3
6	206.7	251.2	324.6	210.7	206.7	187.2	0.0	167.6	250.3	264.3
7	193.1	271.4	281.7	191.9	193.1	188.5	0.0	195.3	205.1	231.7
8	188.8	275.5	267.8	185.5	188.8	184.8	0.0	204.3	189.9	220.6
9	178.2	291.0	249.7	183.9	178.2	183.1	0.0	226.1	174.9	209.8

RP	ABS MACH NO IN	ABS MACH NO OUT	REL MACH NO IN	REL MACH NO OUT	MERID MACH NO IN	MERID MACH NO OUT	MERID VEL R	PEAK SS MACH NO
1	0.568	0.568	1.387	0.834	0.568	0.410	0.791	1.505
2	0.607	0.610	1.378	0.895	0.607	0.495	0.889	1.502
3	0.626	0.617	1.356	0.900	0.626	0.514	0.888	1.490
4	0.647	0.635	1.267	0.814	0.647	0.517	0.861	1.427
5	0.648	0.664	1.135	0.700	0.648	0.522	0.864	1.370
6	0.631	0.722	0.991	0.606	0.631	0.538	0.906	1.374
7	0.587	0.785	0.856	0.555	0.587	0.545	0.976	1.181
8	0.573	0.799	0.812	0.538	0.573	0.536	0.979	1.107
9	0.538	0.847	0.754	0.535	0.538	0.533	1.028	1.040

RP	PERCENT SPAN	INCIDENCE MEAN	INCIDENCE SS	DEV	D FACT	EFF	LOSS COEFF TOT	LOSS COEFF PROF	LOSS PARAM TOT	LOSS PARAM PROF
1	5.00	1.1	-1.2	6.7	0.456	0.725	0.211	0.132	0.039	0.024
2	10.00	1.0	-1.5	2.9	0.394	0.791	0.157	0.080	0.032	0.016
3	15.00	0.8	-1.7	2.0	0.377	0.884	0.083	0.012	0.017	0.002
4	30.00	0.5	-2.3	2.1	0.408	0.930	0.053	0.005	0.011	0.001
5	50.00	1.1	-2.7	5.5	0.447	0.936	0.055	0.031	0.011	0.006
6	70.00	3.6	-3.0	8.4	0.475	0.951	0.051	0.039	0.011	0.008
7	85.00	4.2	-2.4	10.9	0.463	0.920	0.107	0.107	0.021	0.021
8	90.00	3.9	-2.3	12.0	0.458	0.913	0.125	0.125	0.023	0.023
9	95.00	4.5	-1.2	9.1	0.433	0.950	0.084	0.084	0.014	0.014

TABLE VI. – BLADE ELEMENT DATA AT BLADE EDGES FOR STATOR
67B. 100 PERCENT DESIGN SPEED. SI UNITS. READING NUMBER 2609.

RP	RADII IN	RADII OUT	ABS BETAM IN	ABS BETAM OUT	REL BETAM IN	REL BETAM OUT	TOTAL TEMP IN	TOTAL TEMP RATIO	TOTAL PRESS IN	TOTAL PRESS RATIO
1	23.683	23.741	38.4	7.6	38.4	7.6	346.1	0.991	15.94	0.978
2	23.132	23.193	31.4	6.4	31.4	6.4	342.7	0.995	16.48	0.960
3	22.560	22.626	29.8	4.4	29.8	4.4	337.0	1.001	16.51	0.973
4	20.815	20.927	31.6	1.4	31.6	1.4	333.9	1.002	16.44	0.992
5	18.473	18.682	34.4	0.3	34.4	0.3	332.7	1.001	16.32	0.992
6	16.081	16.396	38.7	3.2	38.7	3.2	332.3	1.001	16.37	0.975
7	14.282	14.707	43.1	7.5	43.1	7.5	333.8	0.995	16.38	0.948
8	13.701	14.183	44.7	6.6	44.7	6.6	333.5	0.996	16.27	0.951
9	13.129	13.675	47.6	4.2	47.6	4.2	335.6	0.991	16.59	0.921

RP	ABS VEL IN	ABS VEL OUT	REL VEL IN	REL VEL OUT	MERID VEL IN	MERID VEL OUT	TANG VEL IN	TANG VEL OUT	WHEEL SPEED IN	WHEEL SPEED OUT
1	232.8	174.3	232.8	174.3	182.4	172.8	144.7	23.1	0.0	0.0
2	240.5	184.4	248.5	184.4	212.2	183.3	129.3	20.5	0.0	0.0
3	247.3	191.4	247.3	191.4	214.6	190.8	122.8	14.6	0.0	0.0
4	248.2	203.3	248.2	203.3	211.4	203.3	130.2	4.8	0.0	0.0
5	251.8	203.8	251.8	203.8	207.7	203.8	142.4	0.9	0.0	0.0
6	261.8	201.4	261.8	201.4	204.4	201.0	163.7	11.1	0.0	0.0
7	275.7	192.8	275.7	192.8	201.5	191.2	188.2	25.1	0.0	0.0
8	278.0	193.7	278.0	193.7	197.5	192.5	195.6	22.2	0.0	0.0
9	290.8	188.4	290.8	188.4	196.0	187.9	214.8	13.8	0.0	0.0

RP	ABS MACH NO IN	ABS MACH NO OUT	REL MACH NO IN	REL MACH NO OUT	MERID MACH NO IN	MERID MACH NO OUT	H13 TOT PRESS	TOTAL LOSS COEFF WAKE	MERID VEL R	PEAK SS MACH NO
1	0.650	0.480	0.650	0.480	0.509	0.476	15.88	0.070	0.947	1.197
2	0.702	0.511	0.702	0.511	0.599	0.508	16.09	.058	0.864	1.141
3	0.704	0.534	0.704	0.534	0.611	0.533	16.34	.059	0.889	1.115
4	0.711	0.572	0.711	0.572	0.606	0.572	16.45	.031	0.962	1.144
5	0.724	0.575	0.724	0.575	0.597	0.575	16.32	.029	0.981	1.148
6	0.756	0.560	0.756	0.568	0.590	0.567	16.29	.063	0.984	1.205
7	0.799	0.543	0.799	0.543	0.584	0.538	16.29	.134	0.949	1.290
8	0.807	0.546	0.807	0.546	0.573	0.542	16.22	.131	0.975	1.311
9	0.847	0.529	0.847	0.529	0.571	0.528	16.13	.135	0.958	1.417

RP	PERCENT SPAN	INCIDENCE MEAN	INCIDENCE SS	DEV	D FACT	EFF	LOSS COEFF TOT	LOSS COEFF PROF	LOSS PARAM TOT	LOSS PARAM PROF
1	5.00	-16.1	-21.6	18.8	0.643	0.000	0.088	0.088	0.065	0.065
2	10.00	-20.6	-26.8	17.8	0.578	0.000	0.142	0.142	0.104	0.104
3	15.00	-20.7	-27.6	16.0	0.539	0.000	0.096	0.096	0.068	0.068
4	30.00	-18.3	-26.9	13.5	0.515	0.000	0.028	0.028	0.019	0.019
5	50.00	-18.5	-28.5	12.7	0.520	0.000	0.029	0.029	0.017	0.017
6	70.00	-17.3	-27.8	15.2	0.526	0.000	0.080	0.080	0.041	0.041
7	85.00	-15.8	-26.3	18.7	0.565	0.000	0.151	0.150	0.068	0.068
8	90.00	-15.4	-25.7	17.5	0.570	0.000	0.139	0.138	0.060	0.060
9	95.00	-13.8	-24.0	14.9	0.635	0.000	0.211	0.204	0.088	0.086

TABLE VII. - BLADE ELEMENT DATA AT BLADE EDGES FOR ROTOR
67. 100 PERCENT DESIGN SPEED. SI UNITS.
NEAR WALL DATA SERIES. READING NUMBER 2795. AIRFLOW AT
ORIFICE, 34.67. AIRFLOW FRACTION OF CHOKED VALUE AT
100% N$_D$, 0.992.

RP	RADII IN	RADII OUT	ABS BETAM IN	ABS BETAM OUT	REL BETAM IN	REL BETAM OUT	TOTAL TEMP IN	TOTAL TEMP RATIO	TOTAL PRESS IN	TOTAL PRESS RATIO
1	25.400	24.641	1.2	47.2	71.4	70.0	200.5	1.170	9.25	1.525
2	25.273	24.511	0.5	46.9	69.5	67.0	207.9	1.103	9.49	1.512
3	25.146	24.381	0.3	46.1	67.8	65.9	200.5	1.186	9.73	1.494
4	25.016	24.252	0.4	44.2	66.8	64.2	208.4	1.187	9.86	1.491
5	24.887	24.122	0.7	42.4	65.9	62.9	208.4	1.187	9.97	1.408
6	24.201	23.477	0.9	32.7	64.2	50.0	208.4	1.173	10.15	1.528
7	23.459	22.830	0.3	30.1	63.1	56.9	208.3	1.147	10.16	1.529
8	22.695	22.182	-0.0	30.6	61.7	55.4	208.4	1.145	10.17	1.530
9	18.151	18.301	0.6	35.6	55.3	42.3	207.9	1.140	10.18	1.557
10	14.930	15.712	0.6	33.6	50.4	26.0	207.9	1.155	10.16	1.591
11	11.384	13.124	1.0	44.5	45.0	5.6	208.3	1.157	10.15	1.591

RP	ABS VEL IN	ABS VEL OUT	REL VEL IN	REL VEL OUT	MERID VEL IN	MERID VEL OUT	TANG VEL IN	TANG VEL OUT	WHEEL SPEED IN	WHEEL SPEED OUT
1	142.3	159.5	447.0	316.1	142.2	108.4	3.0	117.0	426.7	414.0
2	157.9	171.1	451.3	309.5	157.9	116.9	1.4	124.9	424.2	411.4
3	172.0	180.3	455.2	306.3	172.0	125.1	0.8	129.8	419.0	409.4
4	179.2	186.5	455.3	307.5	179.2	133.0	1.3	130.0	418.1	407.0
5	185.7	191.4	455.4	310.3	185.7	141.4	2.3	129.0	406.0	405.3
6	194.6	200.0	447.6	331.3	194.6	175.7	2.9	112.9	406.0	393.0
7	199.6	209.3	440.6	331.7	199.6	181.0	0.9	105.1	393.6	383.1
8	205.2	212.3	433.0	321.6	205.2	182.0	-0.1	108.0	381.2	372.6
9	209.2	232.2	367.6	255.3	209.2	108.8	2.2	135.1	304.4	306.9
10	206.1	257.0	322.9	222.0	206.0	198.0	2.3	163.0	250.9	264.1
11	187.8	285.9	265.6	204.9	187.8	204.0	3.2	200.3	191.1	220.3

RP	ABS MACH NO IN	ABS MACH NO OUT	REL MACH NO IN	REL MACH NO OUT	MERID MACH NO IN	MERID MACH NO OUT	MERID VEL R	PEAK SS MACH NO
1	0.425	0.440	1.336	0.872	0.425	0.293	0.762	1.591
2	0.474	0.473	1.356	0.855	0.474	0.323	0.741	1.564
3	0.519	0.498	1.372	0.846	0.519	0.346	0.727	1.536
4	0.541	0.516	1.376	0.851	0.541	0.370	0.747	1.519
5	0.562	0.530	1.379	0.860	0.562	0.392	0.761	1.500
6	0.591	0.585	1.360	0.929	0.591	0.493	0.903	1.498
7	0.608	0.534	1.341	0.941	0.608	0.514	0.906	1.496
8	0.626	0.604	1.321	0.915	0.626	0.520	0.891	1.481
9	0.640	0.655	1.124	0.731	0.640	0.540	0.902	1.363
10	0.623	0.741	0.986	0.640	0.620	0.571	0.961	1.371
11	0.569	0.833	0.805	0.597	0.569	0.595	1.086	1.105

RP	PERCENT SPAN	INCIDENCE MEAN	INCIDENCE SS	DEV	D FACT	EFF	LOSS COEFF TOT	LOSS COEFF PROF	LOSS PARAM TOT	LOSS PARAM PROF
1	1.00	5.4	3.1	15.9	0.387	0.720	0.204	0.114	0.026	0.015
2	2.00	4.0	1.7	13.7	0.415	0.684	0.230	0.142	0.033	0.020
3	3.00	2.7	0.3	11.8	0.431	0.654	0.251	0.167	0.038	0.025
4	4.00	2.0	-0.4	10.2	0.428	0.647	0.255	0.175	0.041	0.028
5	5.00	1.2	-1.1	9.0	0.420	0.644	0.257	0.179	0.043	0.030
6	10.00	1.3	-1.1	4.5	0.347	0.744	0.180	0.106	0.034	0.020
7	15.00	1.3	-1.2	3.7	0.329	0.880	0.077	0.006	0.015	0.001
8	20.00	1.1	-1.5	3.7	0.341	0.893	0.069	0.004	0.013	0.001
9	50.00	1.3	-2.6	6.0	0.406	0.912	0.072	0.050	0.015	0.010
10	70.00	3.5	-3.0	7.9	0.433	0.917	0.086	0.075	0.018	0.016
11	90.00	3.7	-2.6	12.5	0.377	0.904	0.139	0.139	0.026	0.026

TABLE VIII. - BLADE ELEMENT DATA AT BLADE EDGES FOR STATOR
67B. 100 PERCENT DESIGN SPEED. SI UNITS. NEAR WALL DATA
SERIES. READING NUMBER 2795. AIRFLOW AT ORIFICE, 34.67.
AIRFLOW, FRACTION OF CHOKED VALUE AT 100% N_D, 0.992.

RP	RADII IN	RADII OUT	ABS BETAM IN	ABS BETAM OUT	REL BETAM IN	REL BETAM OUT	TOTAL TEMP IN	TOTAL TEMP RATIO	TOTAL PRESS IN	TOTAL PRESS RATIO
1	24.272	24.275	43.0	4.1	43.0	4.1	339.8	0.996	14.10	1.007
2	24.160	24.166	42.9	6.3	42.9	6.3	340.5	0.996	14.35	0.999
3	24.046	24.059	42.4	7.0	42.4	7.0	342.1	0.991	14.53	0.993
4	23.934	23.950	40.7	7.7	40.7	7.7	342.2	0.990	14.71	0.988
5	23.023	23.038	39.0	7.6	39.0	7.6	342.2	0.990	14.84	0.985
6	23.246	23.277	30.0	6.4	30.0	6.4	338.3	0.994	15.51	0.961
7	22.652	22.697	27.6	4.7	27.6	4.7	330.6	1.000	15.53	0.975
8	22.055	22.118	27.9	2.8	27.9	2.8	330.1	1.002	15.56	0.985
9	18.491	18.697	32.5	0.3	32.5	0.3	330.5	1.000	15.85	0.989
10	16.043	16.373	37.4	2.5	37.4	2.5	332.5	0.997	16.17	0.970
11	13.540	14.072	44.5	6.7	44.5	6.7	333.5	0.994	16.15	0.938

RP	ABS VEL IN	ABS VEL OUT	REL VEL IN	REL VEL OUT	MERID VEL IN	MERID VEL OUT	TANG VEL IN	TANG VEL OUT	WHEEL SPEED IN	WHEEL SPEED OUT
1	174.1	144.3	174.1	144.3	127.2	143.9	118.0	10.4	0.0	0.0
2	185.9	156.7	185.9	156.7	136.1	155.8	126.7	17.1	0.0	0.0
3	195.4	163.9	195.4	163.9	144.4	162.7	131.6	20.1	0.0	0.0
4	202.2	169.4	202.2	169.4	153.3	167.9	131.0	22.0	0.0	0.0
5	207.4	173.5	207.4	173.5	161.1	172.0	130.7	23.0	0.0	0.0
6	220.2	184.0	220.2	184.0	197.6	183.6	114.0	20.7	0.0	0.0
7	228.7	192.4	228.7	192.4	202.7	191.7	105.9	15.8	0.0	0.0
8	231.9	199.0	231.9	199.0	204.9	198.8	108.6	9.6	0.0	0.0
9	248.0	213.9	248.0	213.9	209.7	213.9	133.8	1.1	0.0	0.0
10	264.4	223.4	264.4	223.4	210.1	223.2	160.5	9.8	0.0	0.0
11	276.8	213.7	276.8	213.7	197.4	212.3	194.1	25.0	0.0	0.0

RP	ABS MACH NO IN	ABS MACH NO OUT	REL MACH NO IN	REL MACH NO OUT	MERID MACH NO IN	MERID MACH NO OUT	HI3 TOT PRESS	TOTAL LOSS COEFF WAKE	MERID VEL R	PEAK SS MACH NO
1	0.402	0.397	0.402	0.397	0.352	0.396	14.51	0.146	1.131	1.001
2	0.516	0.432	0.516	0.432	0.378	0.430	14.60	.113	1.144	1.075
3	0.542	0.453	0.542	0.453	0.401	0.449	14.60	.097	1.127	1.120
4	0.562	0.469	0.562	0.469	0.426	0.465	14.77	.085	1.095	1.125
5	0.578	0.481	0.578	0.481	0.449	0.477	14.85	.076	1.060	1.113
6	0.644	0.516	0.644	0.516	0.558	0.513	15.14	.064	0.929	1.045
7	0.654	0.541	0.654	0.541	0.579	0.539	15.39	.064	0.946	1.011
8	0.664	0.563	0.664	0.563	0.587	0.562	15.56	.060	0.970	1.025
9	0.717	0.600	0.717	0.609	0.604	0.608	15.82	.033	1.020	1.115
10	0.764	0.636	0.764	0.636	0.607	0.636	16.09	.053	1.062	1.203
11	0.803	0.607	0.803	0.607	0.573	0.602	16.06	.165	1.075	1.334

RP	PERCENT SPAN	INCIDENCE MEAN	INCIDENCE SS	DEV	D FACT	EFF	LOSS COEFF TOT	LOSS COEFF PROF	LOSS PARAM TOT	LOSS PARAM PROF
1	1.00	-13.8	-18.3	14.5	0.644	0.000	-.047	-.047	-.036	-.036
2	2.00	-13.0	-17.6	16.7	0.604	0.000	0.007	0.007	0.005	0.005
3	3.00	-12.8	-17.7	17.6	0.592	0.000	0.036	0.036	0.027	0.027
4	4.00	-14.0	-19.1	10.4	0.568	0.000	0.060	0.060	0.045	0.045
5	5.00	-15.5	-20.7	18.4	0.552	0.000	0.072	0.072	0.054	0.054
6	10.00	-22.0	-28.0	17.7	0.491	0.000	0.161	0.161	0.118	0.118
7	15.00	-22.9	-29.6	16.3	0.441	0.000	0.101	0.101	0.072	0.072
8	20.00	-22.1	-29.5	14.5	0.440	0.000	0.059	0.059	0.041	0.041
9	50.00	-20.4	-30.4	12.7	0.451	0.000	0.039	0.039	0.023	0.023
10	70.00	-18.6	-29.1	14.5	0.442	0.000	0.068	0.068	0.035	0.035
11	90.00	-15.6	-25.8	17.4	0.483	0.000	0.180	0.179	0.077	0.076

TABLE IX. - BLADE ELEMENT DATA AT BLADE EDGES FOR ROTOR 67.
100 PERCENT DESIGN SPEED. SI UNITS. NEAR WALL DATA SERIES.
READING NUMBER 2800. AIRFLOW AT ORIFICE, 34.67. AIRFLOW,
FRACTION OF CHOKED VALUE AT 100 % N_D, 0.992.

RP	RADII IN	RADII OUT	ABS BETAM IN	ABS BETAM OUT	REL BETAM IN	REL BETAM OUT	TOTAL TEMP IN	TOTAL TEMP RATIO	TOTAL PRESS IN	TOTAL PRESS RATIO
1	24.201	23.477	0.9	32.7	64.2	58.0	280.4	1.174	10.13	1.528
2	21.166	20.889	0.1	32.3	59.5	52.0	280.2	1.147	10.14	1.530
3	18.151	18.301	0.6	35.6	55.3	42.3	287.9	1.148	10.16	1.557
4	14.930	15.712	0.6	39.6	50.4	26.8	287.9	1.155	10.14	1.591
5	13.170	14.420	0.8	42.1	47.7	16.2	288.1	1.160	10.14	1.609
6	12.203	13.772	0.8	43.8	46.5	10.6	280.1	1.158	10.15	1.599
7	11.304	13.124	1.0	44.5	45.0	5.6	280.3	1.157	10.13	1.591
8	10.403	12.479	0.9	46.5	43.9	-3.3	280.4	1.165	10.09	1.623
9	10.302	12.349	0.6	47.5	44.5	-5.0	280.6	1.165	10.00	1.622
10	10.122	12.220	0.5	49.2	45.7	-6.4	208.5	1.169	9.83	1.619
11	9.942	12.090	1.0	51.8	47.8	-6.2	280.4	1.166	9.60	1.590

RP	ABS VEL IN	ABS VEL OUT	REL VEL IN	REL VEL OUT	MERID VEL IN	MERID VEL OUT	TANG VEL IN	TANG VEL OUT	WHEEL SPEED IN	WHEEL SPEED OUT
1	194.6	208.9	447.6	331.3	194.6	175.0	2.9	112.9	406.0	393.0
2	209.3	217.2	412.4	290.2	209.3	183.5	0.5	116.2	355.9	351.3
3	209.2	232.1	367.6	255.3	209.2	188.0	2.2	135.1	304.4	306.9
4	206.1	257.0	322.9	222.0	206.0	198.0	2.3	163.0	250.9	264.1
5	190.3	272.8	294.9	210.7	190.3	202.3	2.9	183.1	221.1	242.0
6	192.0	278.7	279.9	204.6	192.8	201.1	2.9	192.9	205.7	230.7
7	187.8	285.9	265.6	204.9	187.8	203.9	3.2	200.3	191.1	220.3
8	180.3	306.6	250.2	211.5	180.2	211.1	2.9	222.3	176.4	210.0
9	174.1	305.0	244.1	207.3	174.1	206.5	1.8	225.5	172.9	207.3
10	164.1	300.2	235.1	197.5	164.1	196.3	1.6	227.1	169.9	205.1
11	149.0	282.9	222.0	175.9	149.0	174.9	2.7	222.3	167.2	203.4

RP	ABS MACH NO IN	ABS MACH NO OUT	REL MACH NO IN	REL MACH NO OUT	MERID MACH NO IN	MERID MACH NO OUT	MERID PEAK SS VEL R	MACH NO
1	0.591	0.585	1.360	0.920	0.591	0.493	0.903	1.498
2	0.640	0.618	1.260	0.819	0.640	0.522	0.877	1.427
3	0.640	0.665	1.124	0.731	0.640	0.540	0.902	1.363
4	0.629	0.741	0.986	0.640	0.629	0.571	0.961	1.371
5	0.604	0.790	0.898	0.610	0.604	0.585	1.020	1.249
6	0.586	0.809	0.850	0.594	0.586	0.584	1.043	1.179
7	0.567	0.833	0.805	0.597	0.569	0.595	1.086	1.105
8	0.545	0.899	0.756	0.620	0.545	0.619	1.171	1.037
9	0.525	0.896	0.736	0.608	0.525	0.605	1.186	1.025
10	0.493	0.876	0.707	0.576	0.493	0.573	1.197	1.018
11	0.446	0.819	0.665	0.510	0.446	0.507	1.174	1.005

RP	PERCENT SPAN	INCIDENCE MEAN	INCIDENCE SS	DEV	D FACT	EFF	LOSS COEFF TOT	LOSS COEFF PROF	LOSS PARAM TOT	LOSS PARAM PROF
1	10.00	1.3	-1.1	4.5	0.347	0.741	0.183	0.109	0.035	0.021
2	20.00	0.7	-2.0	3.6	0.366	0.892	0.083	0.036	0.016	0.007
3	50.00	1.3	-2.6	6.0	0.406	0.912	0.072	0.050	0.015	0.010
4	70.00	3.5	-3.0	7.9	0.433	0.917	0.066	0.075	0.010	0.016
5	80.00	3.9	-3.2	8.9	0.420	0.913	0.108	0.106	0.022	0.022
6	85.00	3.9	-2.8	10.5	0.411	0.910	0.120	0.120	0.023	0.023
7	90.00	3.7	-2.6	12.5	0.377	0.905	0.137	0.137	0.025	0.025
8	95.00	3.9	1.3	10.9	0.320	0.901	0.164	0.164	0.028	0.028
9	96.00	4.6	-1.1	10.2	0.321	0.897	0.178	0.178	0.030	0.030
10	97.00	6.0	0.4	10.4	0.336	0.875	0.235	0.235	0.039	0.039
11	98.00	8.2	2.7	12.1	0.387	0.852	0.304	0.304	0.050	0.050

TABLE X. - BLADE ELEMENT DATA AT EDGES FOR STATOR 676. 100
PERCENT DESIGN SPEED. SI UNITS. NEAR WALL DATA SERIES.
READING NUMBER 2800. AIRFLOW AT ORIFICE, 34.67. AIRFLOW,
FRACTION OF CHOKED VALUE AT 100% N_D, 0.992.

	RADII		ABS BETAM		REL BETAM		TOTAL TEMP		TOTAL PRESS	
RP	IN	OUT	IN	OUT	IN	OUT	IN	RATIO	IN	RATIO
1	23.246	23.277	30.0	6.4	30.0	6.4	338.5	0.994	15.48	0.961
2	20.064	20.973	29.4	0.8	29.4	0.8	330.5	0.999	15.51	0.994
3	18.481	18.697	32.5	0.3	32.5	0.3	330.5	1.000	15.82	0.989
4	16.043	16.373	37.4	2.5	37.4	2.5	332.5	0.997	16.14	0.978
5	14.806	15.204	40.5	6.3	40.5	6.3	334.1	0.994	16.33	0.947
6	14.181	14.633	42.8	7.7	42.8	7.7	333.6	0.993	16.24	0.938
7	13.548	14.072	44.5	6.7	44.5	6.7	333.4	0.994	16.12	0.938
8	12.908	13.510	48.2	3.4	48.2	3.4	335.9	0.989	16.38	0.909
9	12.779	13.406	49.6	2.4	49.6	2.4	336.3	0.990	16.22	0.914
10	12.652	13.297	51.4	0.9	51.4	0.9	337.1	0.907	15.92	0.929
11	12.522	13.188	54.1	-0.8	54.1	-0.8	336.4	0.990	15.26	0.968

	ABS VEL		REL VEL		MERID VEL		TANG VEL		WHEEL SPEED	
RP	IN	OUT	IN	OUT	IN	OUT	IN	OUT	IN	OUT
1	228.3	184.8	228.3	184.8	197.7	183.7	114.1	20.7	0.0	0.0
2	236.8	205.3	236.8	205.3	206.3	205.2	116.3	3.0	0.0	0.0
3	248.7	213.9	248.7	213.9	209.7	213.9	133.8	1.1	0.0	0.0
4	264.4	223.4	264.4	223.4	210.1	223.2	160.4	9.8	0.0	0.0
5	274.5	217.5	274.5	217.5	208.8	216.2	178.3	24.0	0.0	0.0
6	276.0	213.3	276.0	213.3	202.6	211.4	187.4	28.6	0.0	0.0
7	276.8	213.7	276.8	213.7	197.4	212.3	194.0	25.0	0.0	0.0
8	288.2	209.0	288.2	209.0	192.0	208.6	214.9	12.3	0.0	0.0
9	286.3	207.5	286.3	207.5	185.6	207.3	217.9	8.6	0.0	0.0
10	280.6	206.5	280.6	206.5	175.0	206.5	219.4	3.1	0.0	0.0
11	265.0	206.0	265.0	206.0	155.5	206.0	214.6	-2.9	0.0	0.0

	ABS MACH NO		REL MACH NO		MERID MACH NO		H13 TOT PRESS	TOTAL LOSS COEFF WAKE	MERID VEL R	PEAK SS MACH NO
RP	IN	OUT	IN	OUT	IN	OUT				
1	0.644	0.516	0.644	0.516	0.559	0.513	15.11	0.064	0.929	1.045
2	0.679	0.582	0.679	0.582	0.592	0.582	15.58	.038	0.935	1.065
3	0.717	0.608	0.717	0.608	0.604	0.608	15.79	.033	1.020	1.115
4	0.764	0.636	0.764	0.636	0.607	0.636	16.06	.053	1.062	1.209
5	0.795	0.618	0.795	0.618	0.605	0.614	16.17	.128	1.035	1.202
6	0.800	0.605	0.800	0.606	0.588	0.600	16.12	.159	1.043	1.317
7	0.803	0.607	0.803	0.607	0.573	0.602	16.03	.166	1.075	1.334
8	0.837	0.592	0.837	0.592	0.558	0.591	15.80	.152	1.087	1.458
9	0.831	0.586	0.831	0.586	0.533	0.586	15.69	.146	1.117	1.482
10	0.811	0.583	0.811	0.583	0.506	0.583	15.59	.142	1.180	1.493
11	0.761	0.582	0.761	0.582	0.447	0.582	15.53	.158	1.325	1.470

	PERCENT	INCIDENCE		DEV	D FACT	EFF	LOSS COEFF		LOSS PARAM	
RP	SPAN	MEAN	SS				TOT	PROF	TOT	PROF
1	10.00	-22.0	-20.0	17.7	0.471	0.000	0.161	0.161	0.118	0.118
2	30.00	-20.5	-29.1	12.9	0.449	0.000	0.022	0.022	0.015	0.015
3	50.00	-20.4	-30.4	12.7	0.451	0.000	0.039	0.039	0.023	0.023
4	70.00	-18.6	-29.1	14.5	0.442	0.000	0.068	0.068	0.035	0.035
5	80.00	-17.3	-27.8	17.0	0.467	0.000	0.155	0.155	0.072	0.072
6	85.00	-16.2	-26.5	18.8	0.480	0.000	0.179	0.179	0.080	0.079
7	90.00	-15.6	-25.8	17.4	0.483	0.000	0.180	0.179	0.077	0.076
8	95.00	-13.2	-23.2	13.5	0.554	0.000	0.247	0.230	0.100	0.097
9	96.00	-11.9	-21.9	12.4	0.563	0.000	0.236	0.226	0.095	0.091
10	97.00	-10.3	-20.2	10.8	0.564	0.000	0.201	0.191	0.000	0.077
11	98.00	-7.7	-17.6	9.1	0.539	0.000	0.101	0.096	0.040	0.038
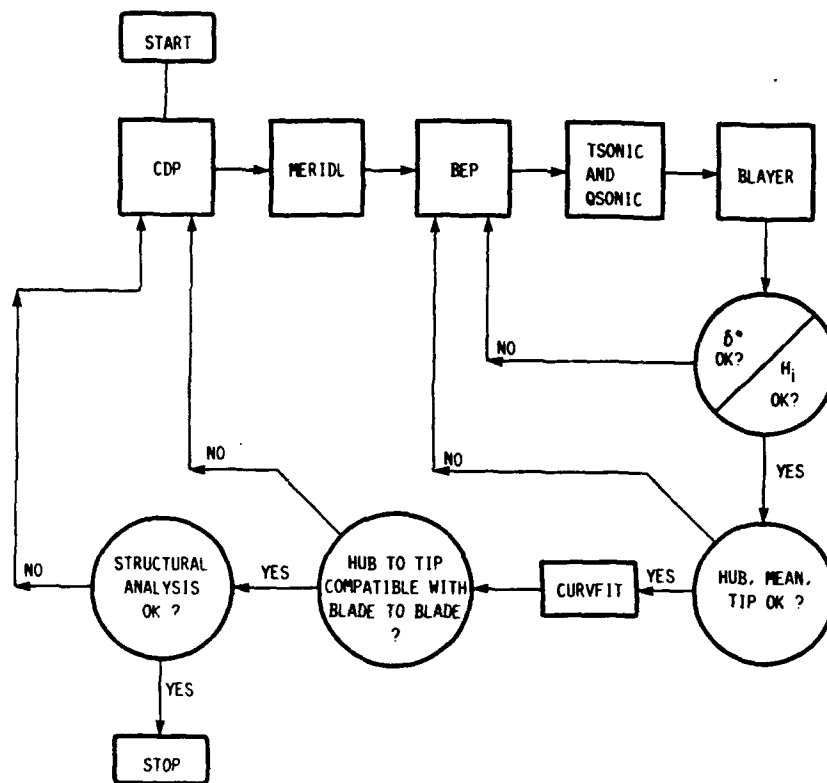
Figure 1.—Design and analysis system.
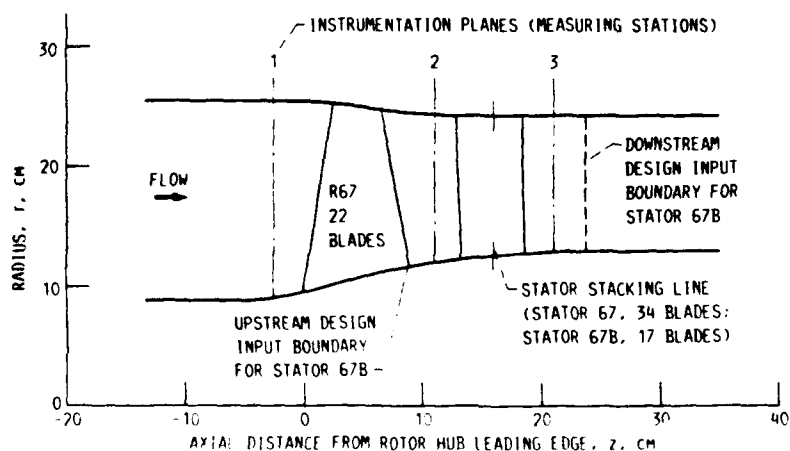
AXIAL DISTANCE z, cm	RADIUS, r, cm	
	OUTER	INNER
-13.093	25.654	8.994
-8.016		8.903
-2.936		9.093
a-2.490		9.174
-0.203	25.651	9.543
2.144	25.570	10.160
4.684	25.128	10.973
7.224	24.681	11.565
9.764	24.460	11.902
a11.000	24.430	12.040
12.304	24.384	12.139
14.844		12.438
17.384		12.822
19.924		13.025
20.803		13.038
a21.060		13.040
25.000		13.050

aMEASURING STATION.

Figure 2.—Flow path schematic and coordinates for stage 67B.
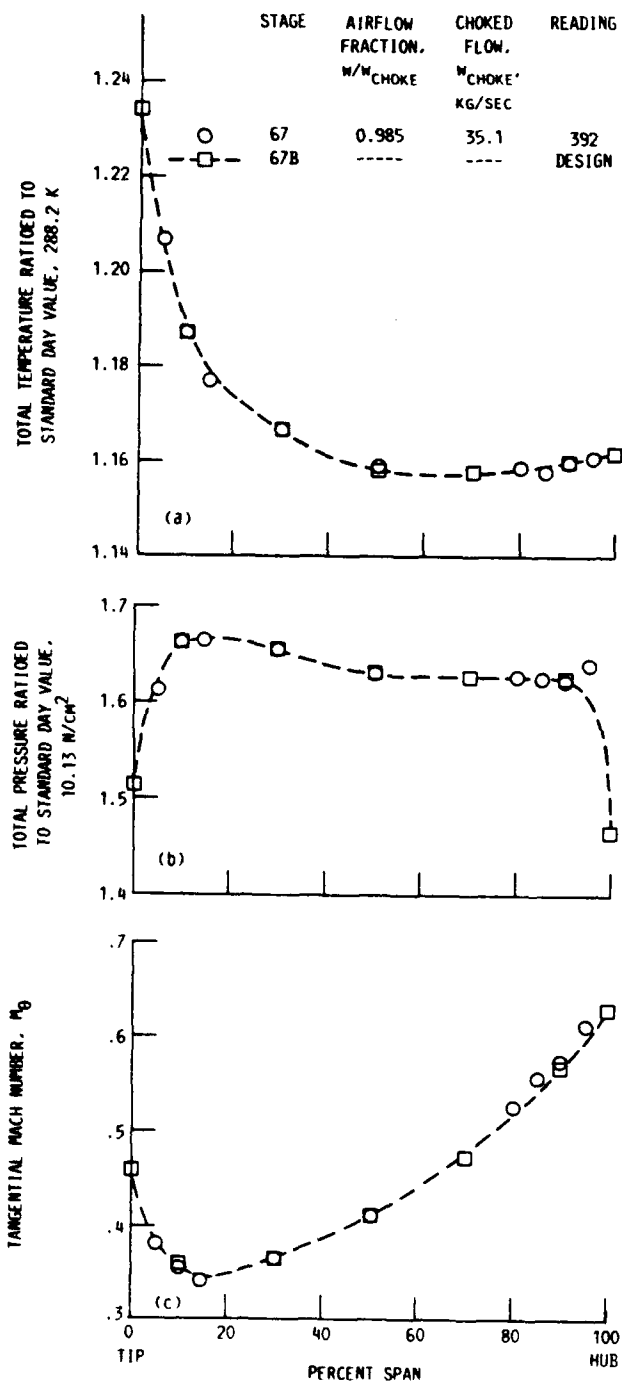
(a) Total temperature ratioed to standard day value. 288.2 K.
(b) Total pressure ratioed to standard day value. 10.13 N/cm².
(c) Tangential Mach number. M_θ

Figure 3.—Upstream design inputs to CDP for stator 67B and performance data from stage 67 at its best operating point. All values at rotor trailing edge. (See fig. 2.)
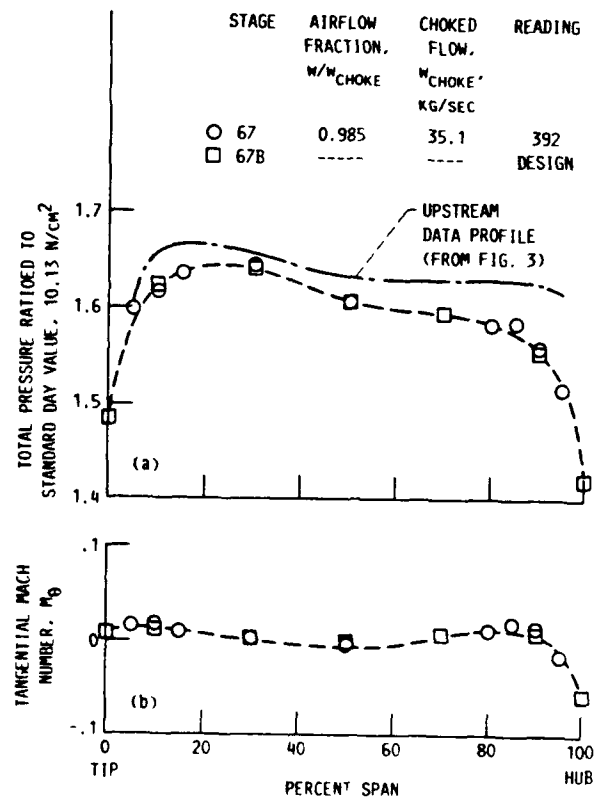
(a) Total pressure ratioed to standard day value. 10.13 N/cm².
(b) Tangential Mach number. M_θ

Figure 4.—Downstream design inputs to CDP for stator 67B and performance data from stage 67 at its best operating point. All values at about one stator chord downstream of stator 67B trailing edge. (See fig. 2.)

(a) Stream-tube height.
(b) Streamline radius.
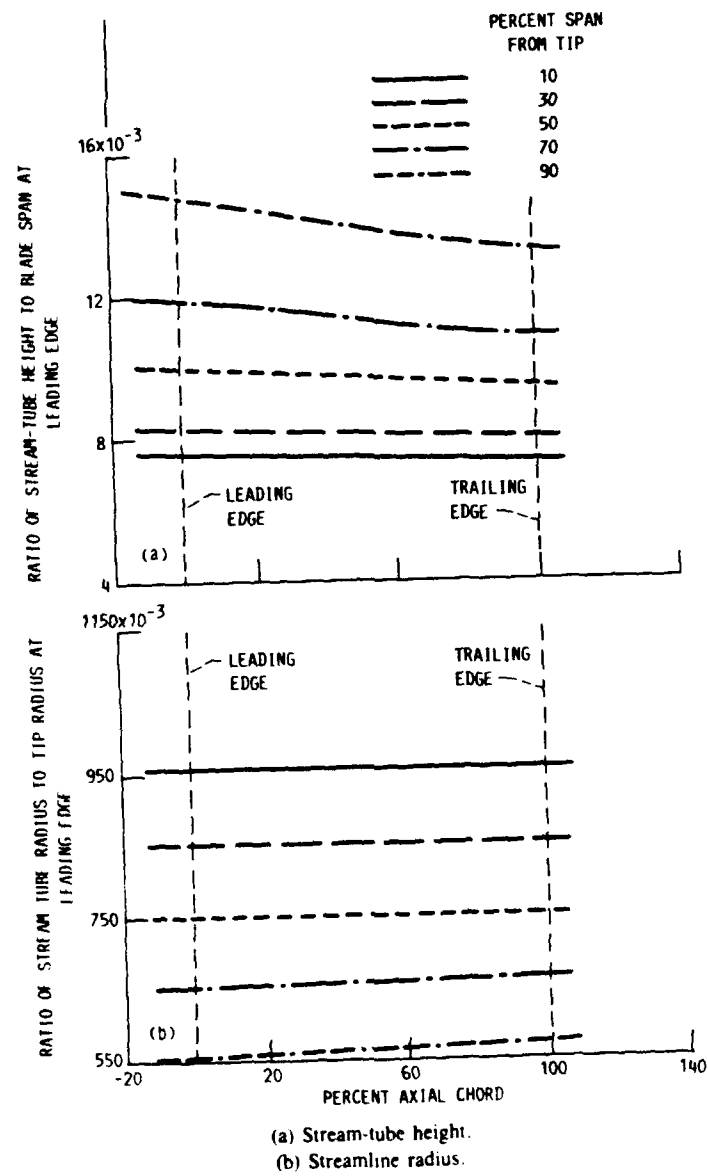
Figure 5.—Chordwise distribution of stream-tube height and streamline radius for stator 67B at several spanwise locations for design conditions.
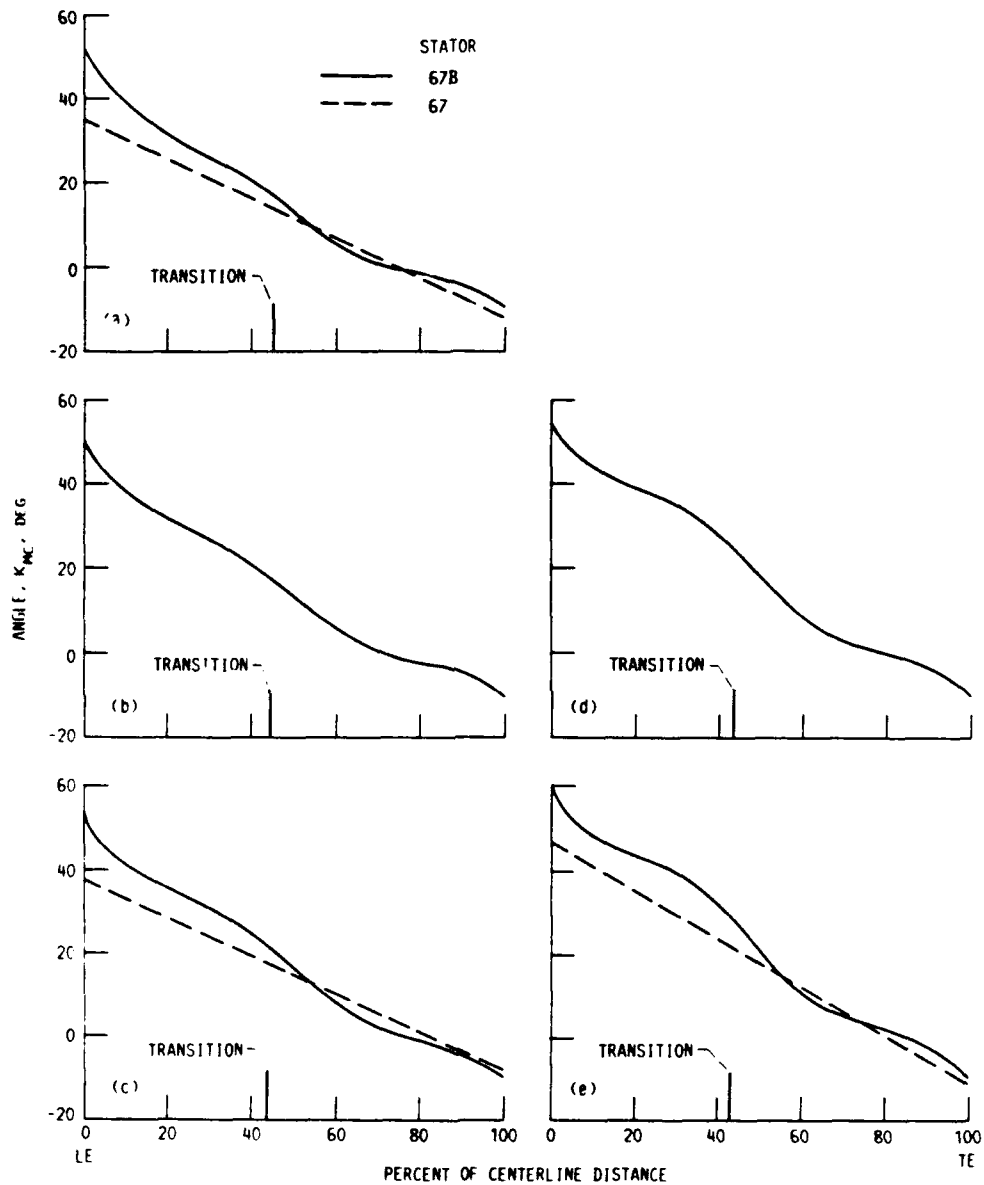
(a) Blade angle at 10-percent span from tip
(b) Blade angle at 30-percent span from tip
(c) Blade angle at 50-percent span from tip
(d) Blade angle at 70-percent span from tip
(e) Blade angle at 90-percent span from tip

Figure 6 —Chordwise distribution of blade angle (of mean line) and blade thickness for stator 67B and 67 at several spanwise locations
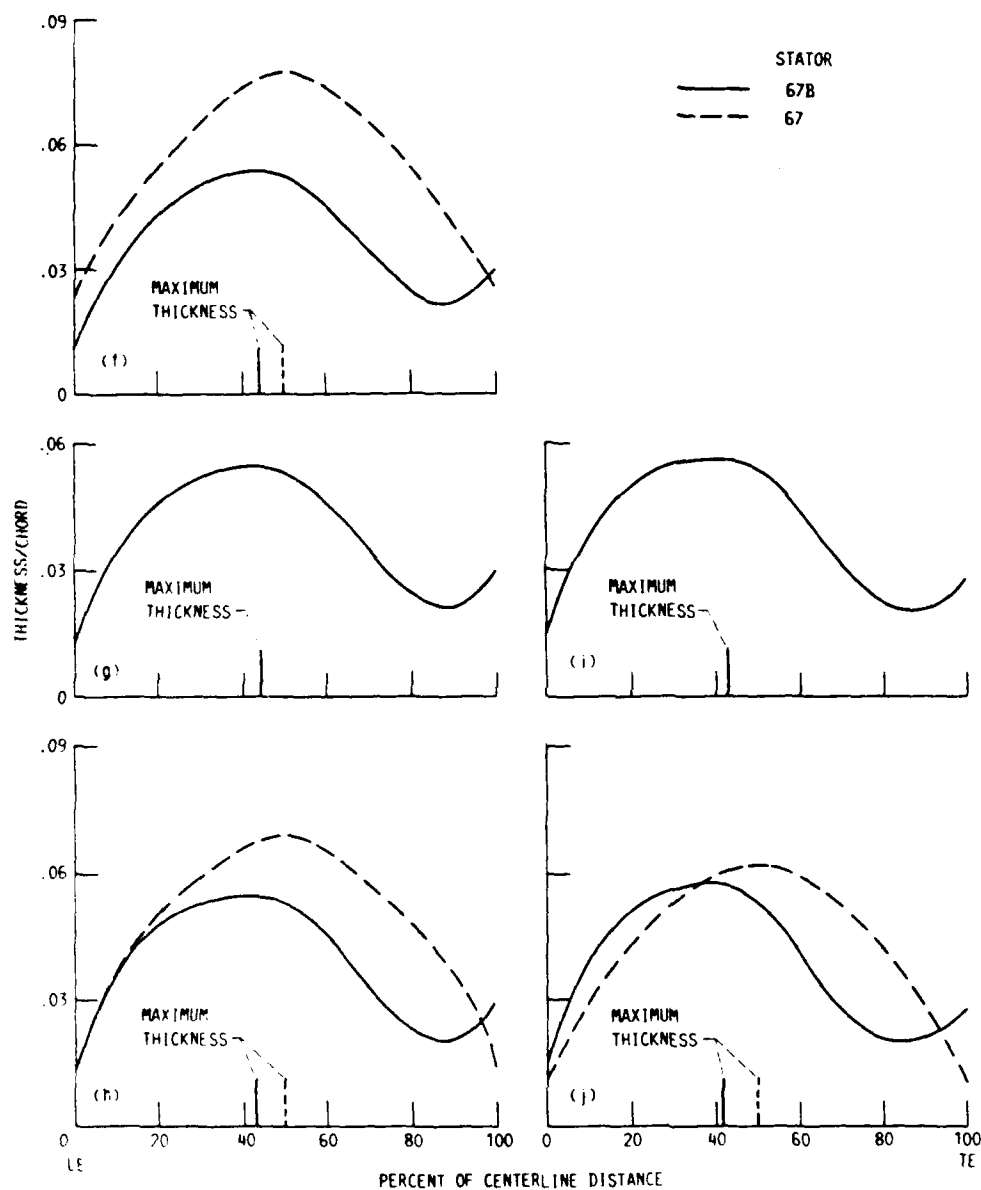
(f) Blade thickness at 10-percent span from tip
(g) Blade thickness at 30-percent span from tip
(h) Blade thickness at 50-percent span from tip
(i) Blade thickness at 70-percent span from tip
(j) Blade thickness at 90-percent span from tip

Figure 6.—Concluded

(a) Ten-percent span from tip.
(b) Thirty-percent span from tip.
(c) Fifty-percent span from tip.
(d) Seventy-percent span from tip.
(e) Ninety-percent span from tip
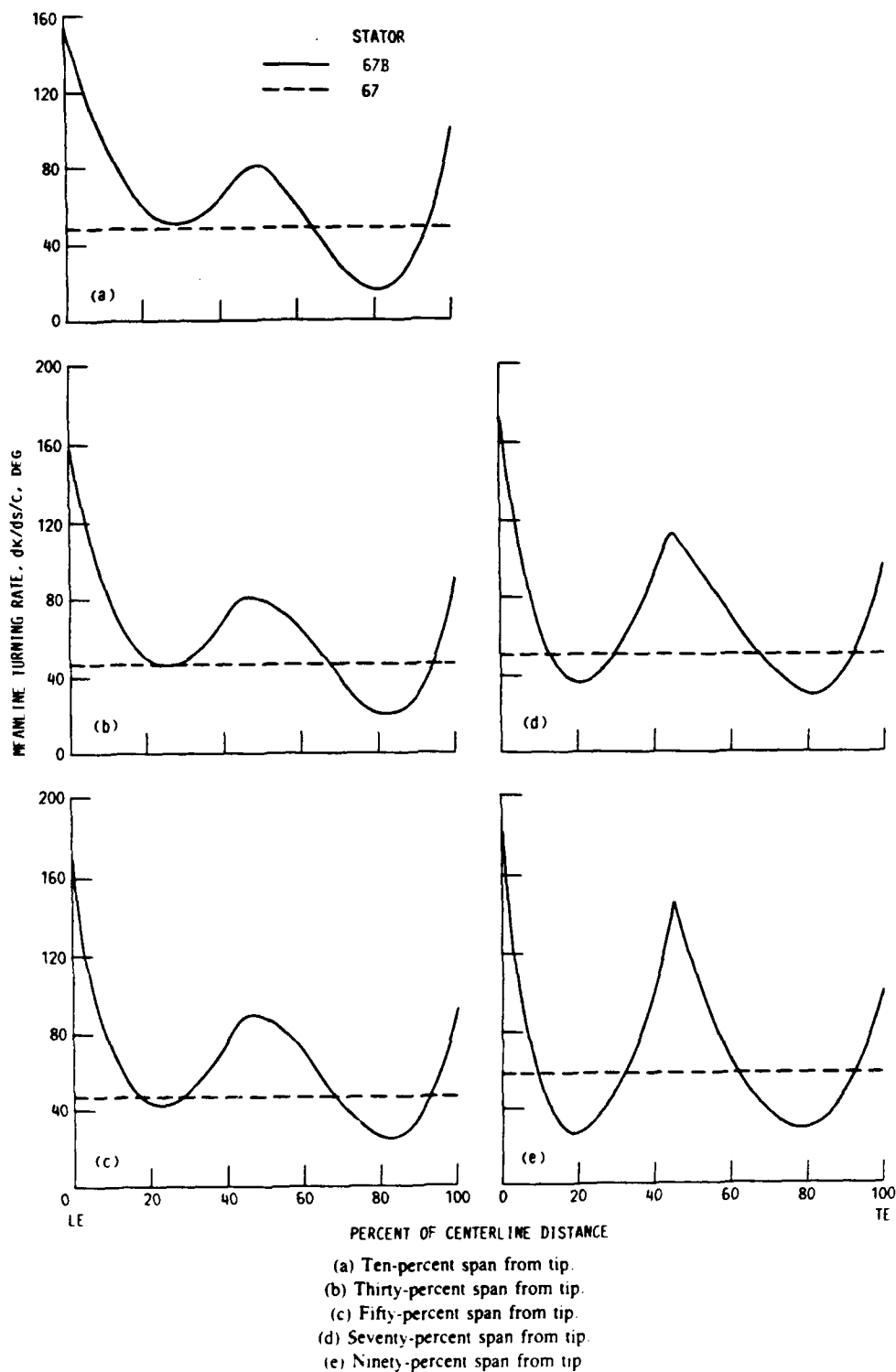
Figure 7.—Chordwise distribution of mean-line turning rates for stator 67B and 67 at several spanwise locations

1x

Figure 8.—Spanwise distributions of stator blade geometry parameters.
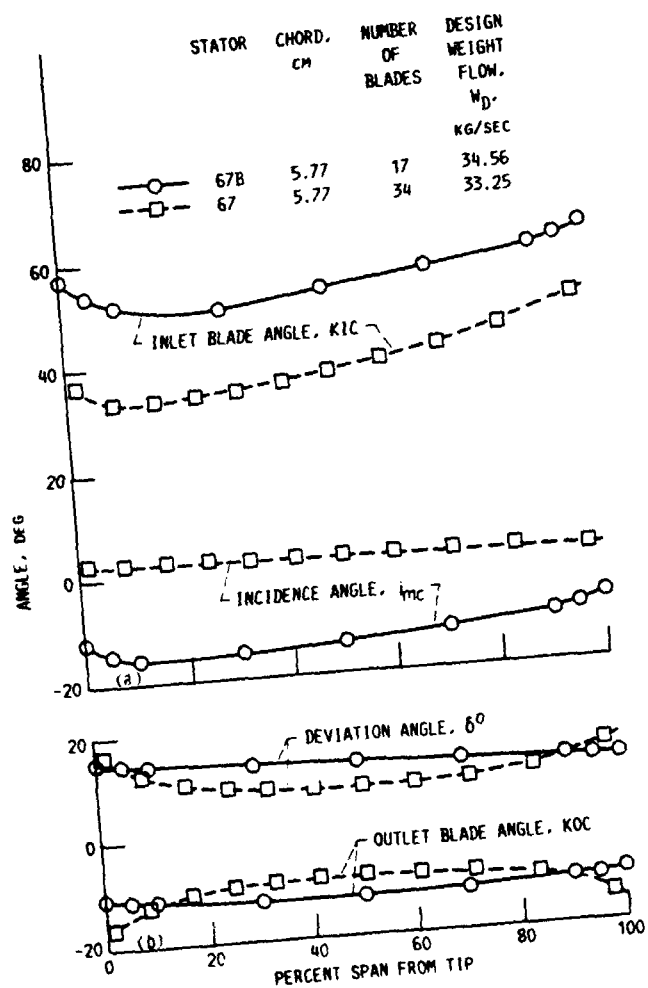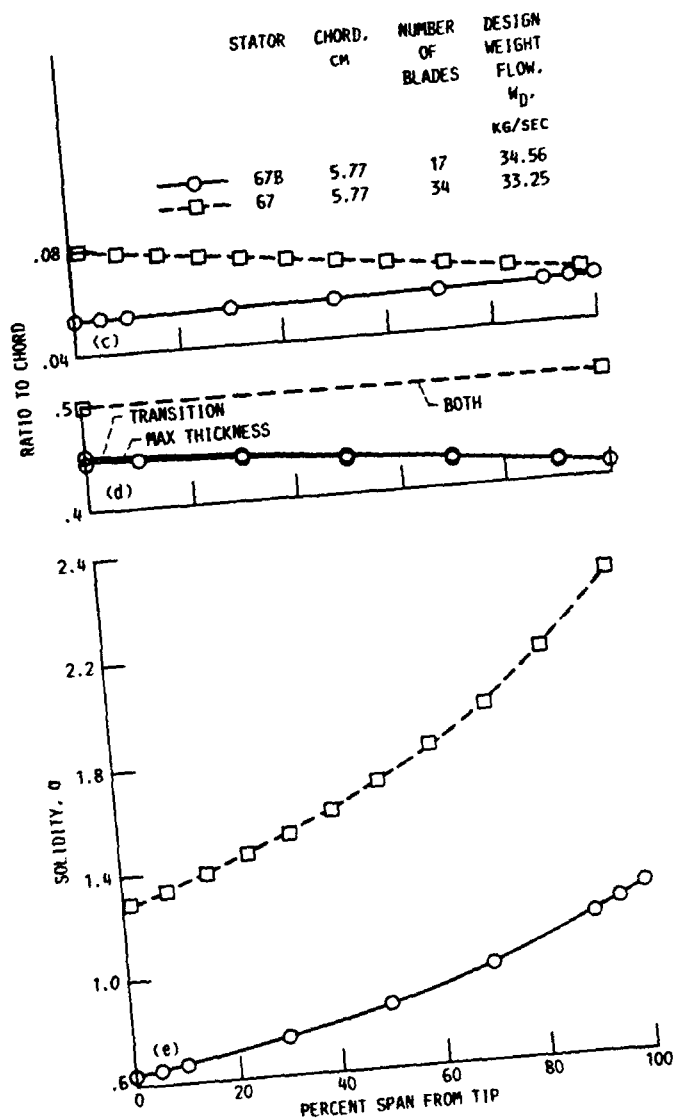
(a) Leading edge parameters.
(b) Trailing edge parameters.
(c) Maximum thickness.
(d) Transition and maximum thickness locations.
(e) Blade chord to spacing ratio (solidity).
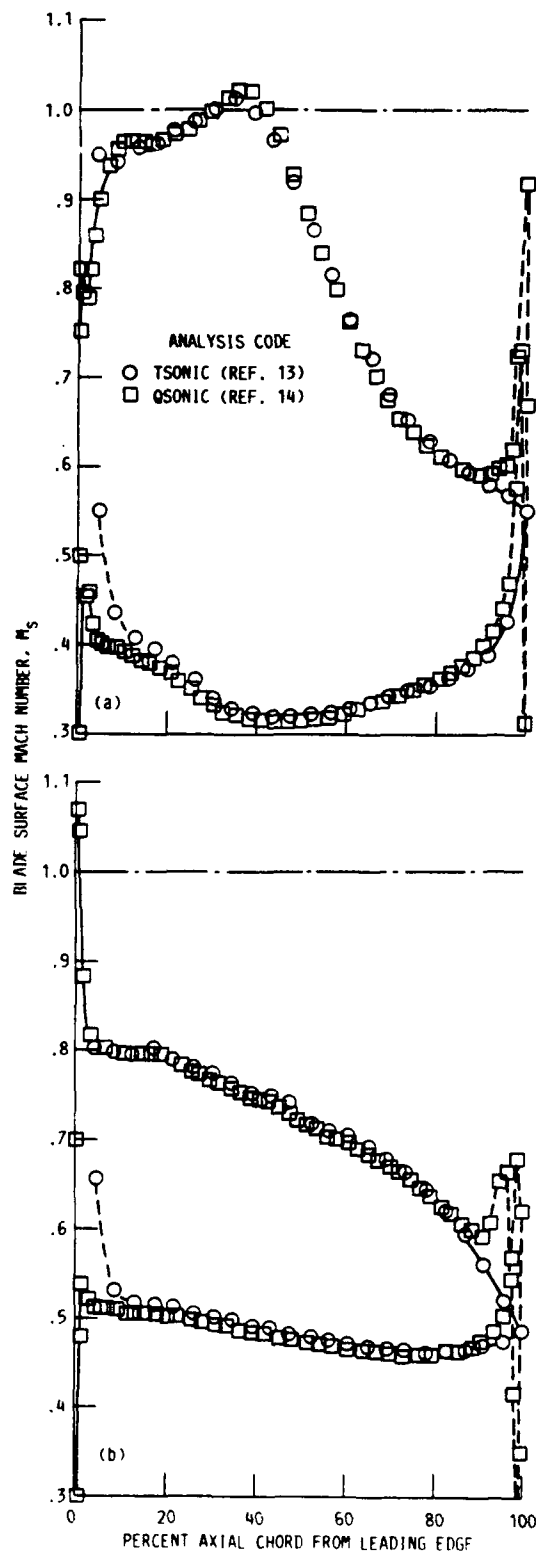
(a) Stator 67B. $i_{m_i} = -14°$, $\sigma = 0.84$.
(b) Stator 67. $i_{m_i} = 2.0°$, $\sigma = 1.68$.

Figure 9—Chordwise distribution of blade surface Mach numbers for the midspan sections of stator 67B and 67 at design conditions from analysis codes
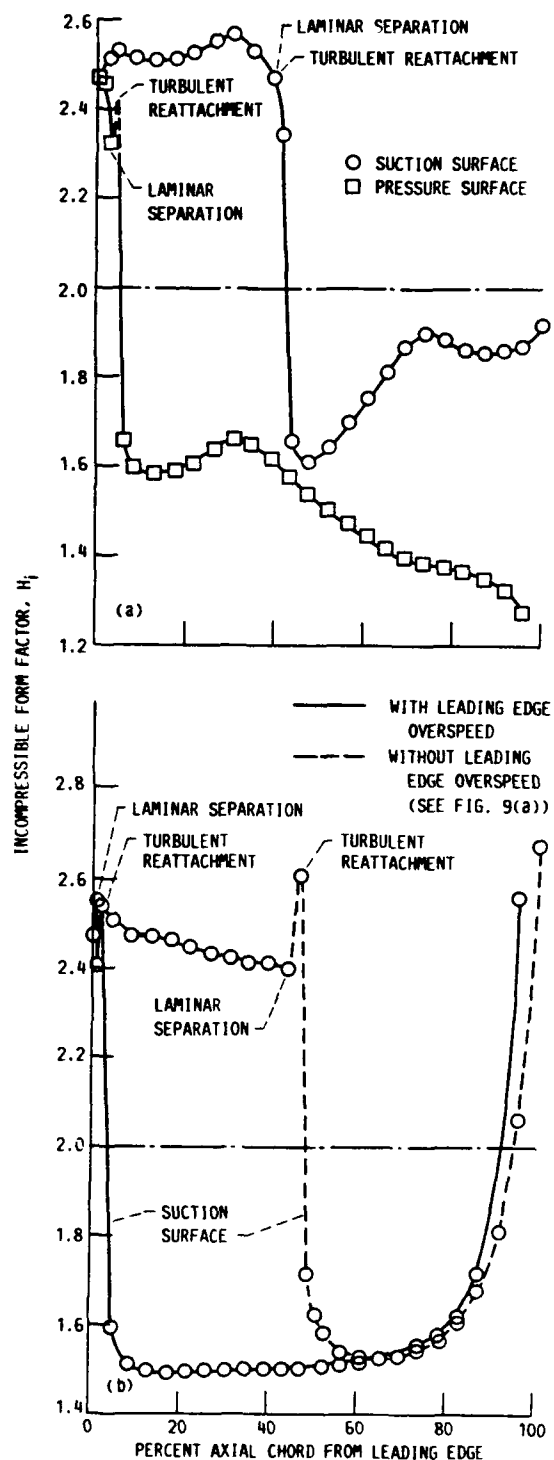
(a) Stator 67B
(b) Stator 67.

Figure 10—Chordwise distribution of boundary-layer form factors for the midspan sections of stator 67B and 67 at design conditions from analysis code (BLAYER)
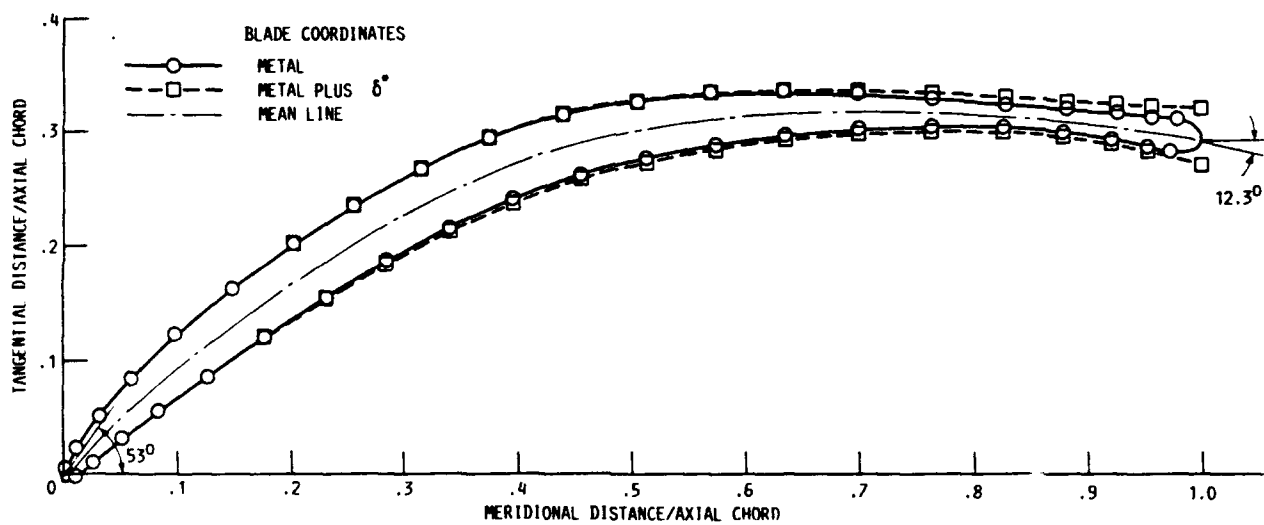
Figure 11.—Stator blade 67B geometry at midspan with mean-line and boundary-layer displacement thickness δ^* indicated.
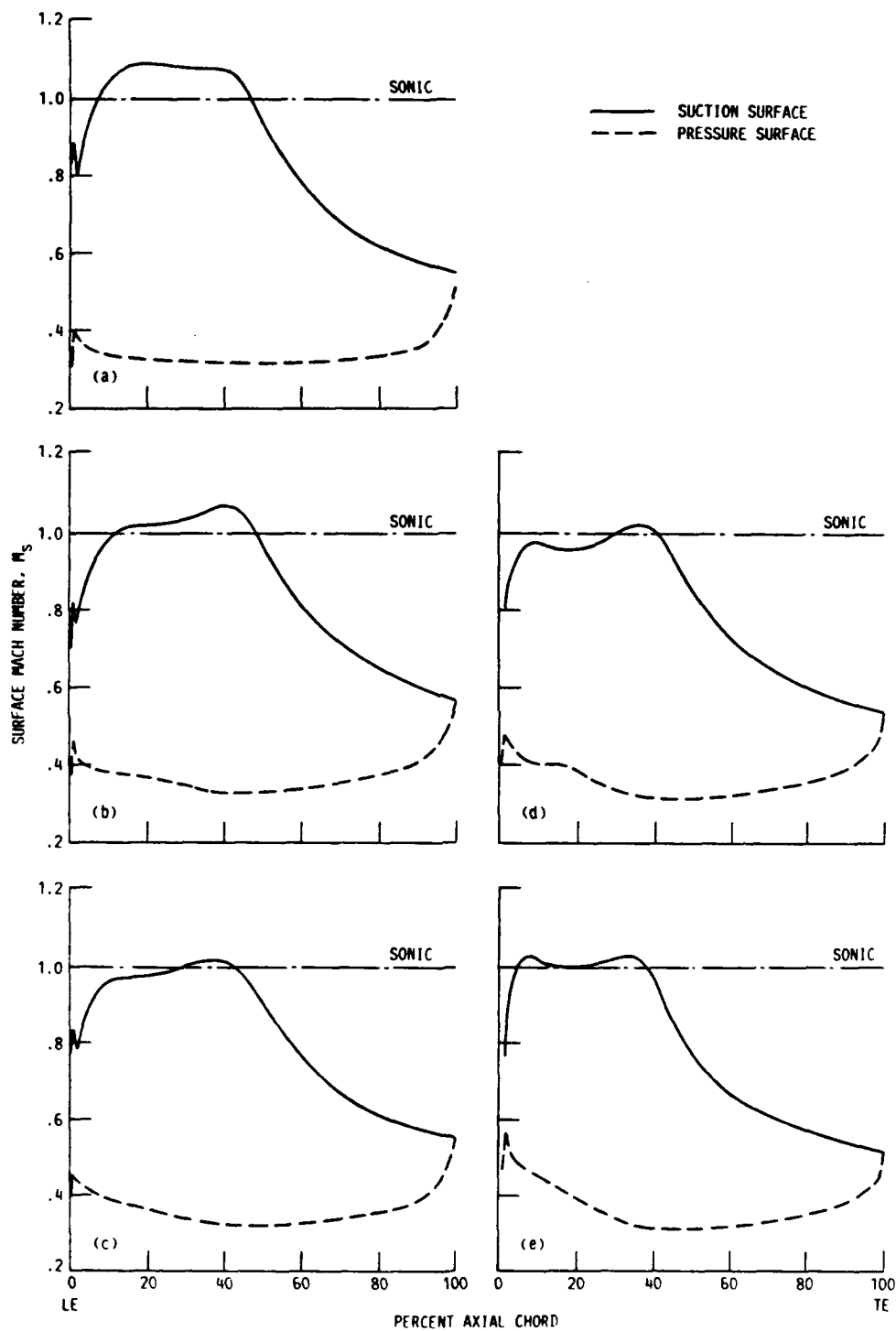
(a) Mach number, 10-percent span from tip.
(b) Mach number, 30-percent span from tip.
(c) Mach number, 50-percent span from tip.
(d) Mach number, 70-percent span from tip.
(e) Mach number, 90-percent span from tip.

Figure 12.—Chordwise distribution of blade surface Mach number and form factors for stator 67B at several spanwise locations for design conditions.
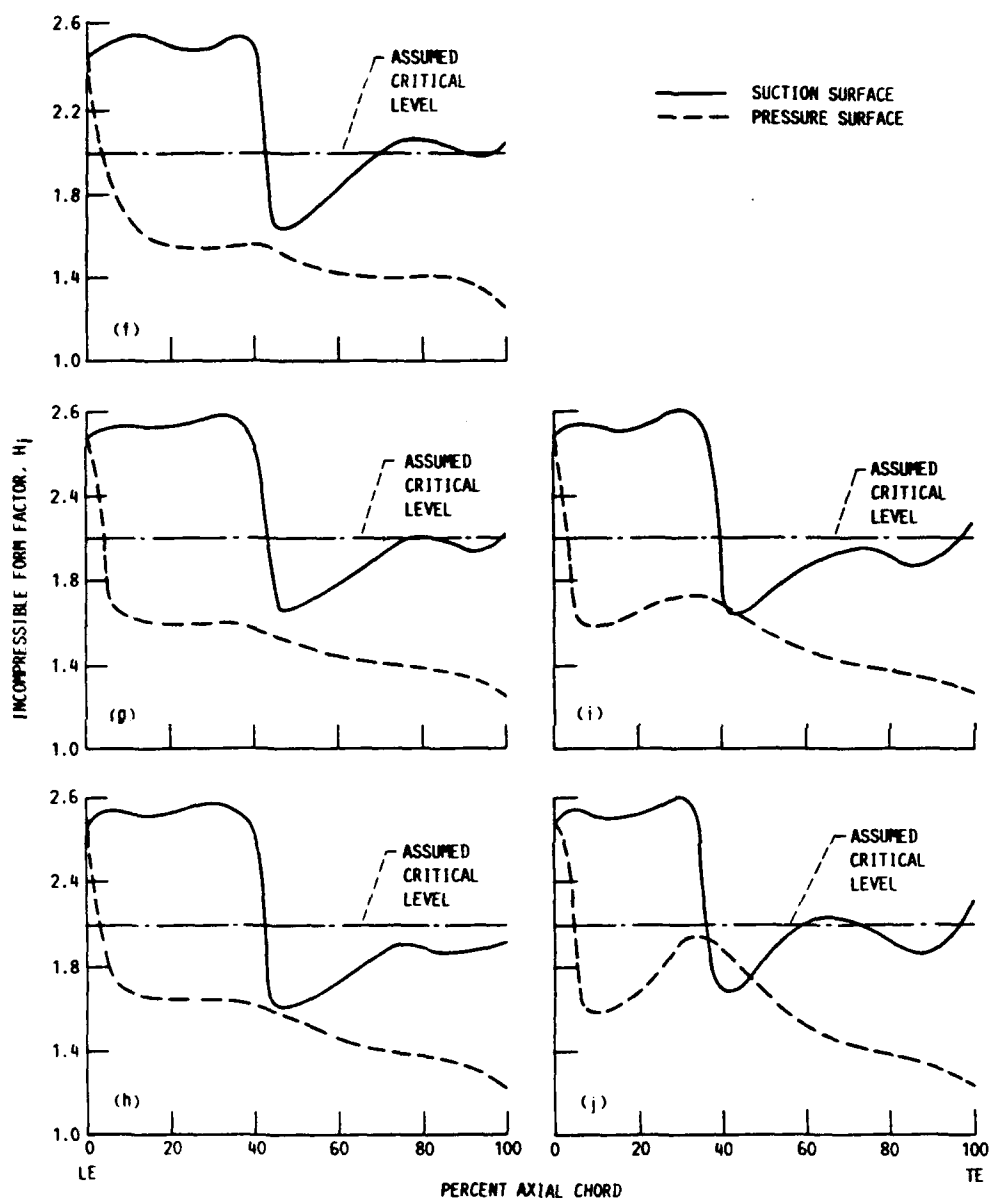
(f) Form factor, 10-percent span from tip.
(g) Form factor, 30-percent span from tip.
(h) Form factor, 50-percent span from tip.
(i) Form factor, 70-percent span from tip.
(j) Form factor, 90-percent span from tip.

Figure 12.—Concluded.

(a) Tip, 10-percent span.
(b) Mean, 50-percent span.
(c) Hub, 90-percent span.
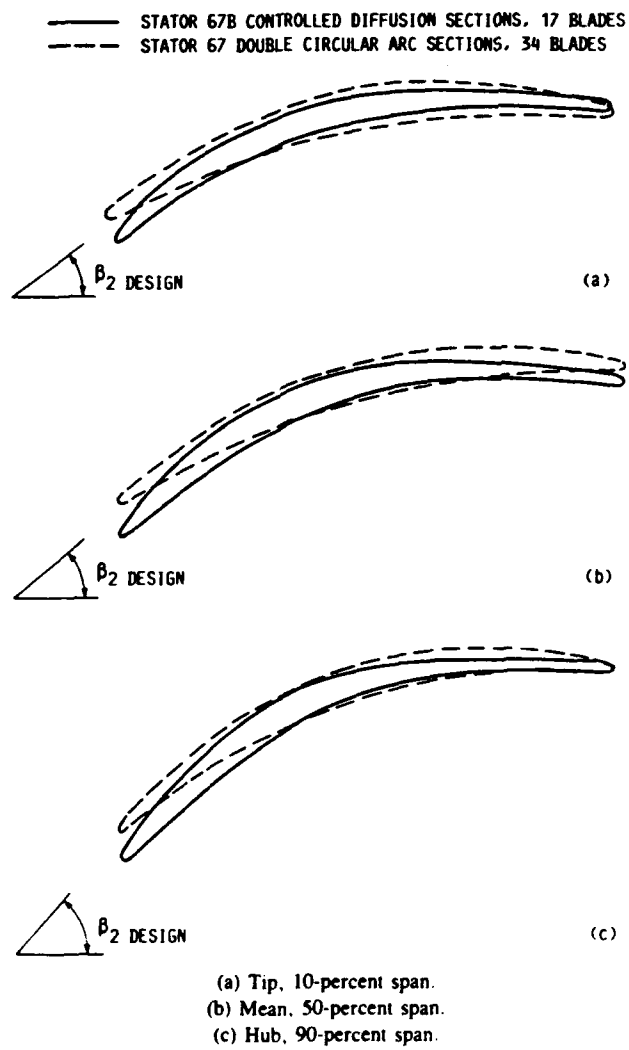
Figure 13.—Comparison of blade cross sections between stator 67B and 67 at 10-, 50-, and 90-percent span. Chord 5.77 cm (nominal).

(a) Coordinate axes and definition of elliptical edges (diagram with labels: UPPER SURFACE, LOWER SURFACE, 21, 1, M, MSP1(21), MSP2(21), R02, BETO1, R01, MSP1(1), MSP2(1), BETI1, R12, R11, LEADING EDGE ELLIPSE, TRAILING EDGE ELLIPSE)

(b)
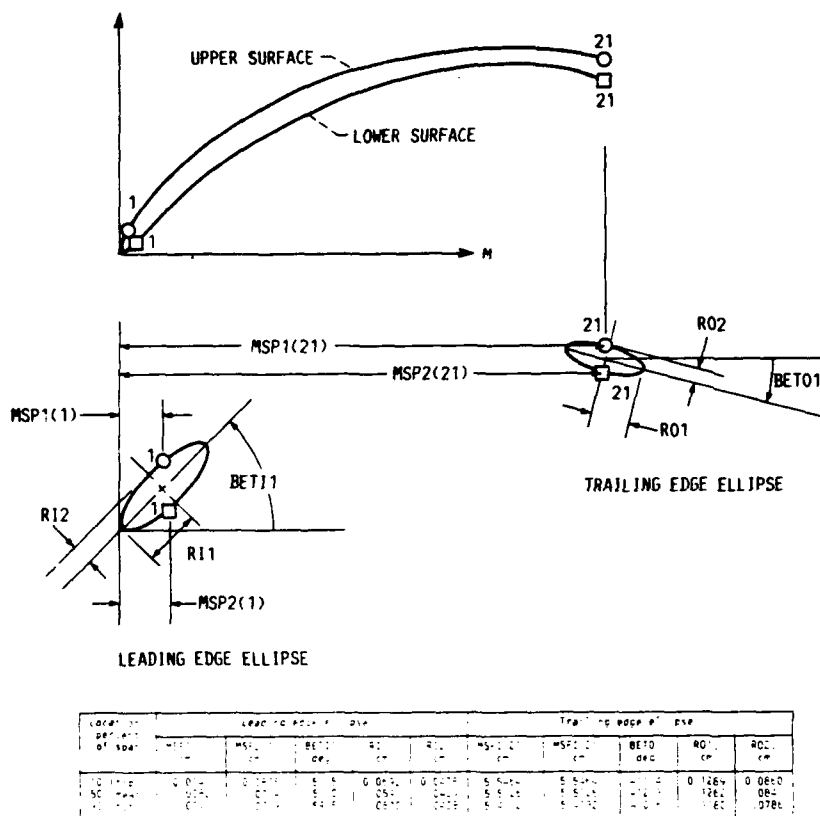
Location, percent of span	Upper surface		Lower surface	
	Meridional streamline distance, m, cm	Tangential distance, n, cm	Meridional streamline distance, m, cm	Tangential distance, n, cm
10 (tip)	0.0143	0.0437	0.0875	-0.0162
	.0823	.1408	.1698	.0621
	.1945	.2801	.2987	.1719
	.3594	.4518	.4788	.3075
	.5840	.6465	.7132	.4631
	.8123	.8542	1.0058	.6336
	1.1153	1.0382	1.3061	.7905
	1.4900	1.2028	1.6133	.9330
	1.8148	1.3847	1.9257	1.0607
	2.1510	1.4654	2.2430	1.1100
	2.4990	1.5551	2.5643	1.2584
	2.8535	1.6069	2.8919	1.3279
	3.2083	1.6266	3.7260	1.3793
	3.5607	1.6236	3.5656	1.4142
	3.9100	1.6075	3.9091	1.4356
	4.2578	1.5865	4.2541	1.4449
	4.6049	1.5660	4.5991	1.4414
	4.8945	1.5501	4.8859	1.4251
	5.1273	1.5366	5.1133	1.3096
	5.3032	1.5241	5.2813	1.3707
	5.5464	1.5010	5.5464	1.3063
50 (mean)	0.0082	0.0311	0.0734	-0.0202
	.0698	.1343	.1594	.0570
	.1756	.2812	.2914	.1691
	.3344	.4644	.4724	.3077
	.5514	.6696	.7053	.4750
	.8288	.8953	.9903	.6679
	1.1198	1.1024	1.2817	.8538
	1.4240	1.2947	1.5773	1.0273
	1.7428	1.4675	1.8797	1.1855
	2.0172	1.6127	2.1897	1.3184
	2.4262	1.7218	2.5082	1.4271
	2.7843	1.7930	2.8349	1.5169
	3.1449	1.8251	3.1699	1.5828
	3.5034	1.8300	3.5122	1.6211
	3.8591	1.8203	3.8588	1.6569
	4.2123	1.7985	4.2081	1.6666
	4.5647	1.7768	4.5577	1.6615
	4.8585	1.7558	4.8478	1.6392
	5.0941	1.7377	5.0177	1.6079
	5.2718	1.7246	5.2477	1.5767
	5.5126	1.6978	5.5126	1.5056
90 (hub)	0.0043	0.0230	0.0719	-0.0177
	.0542	.1391	.1527	.0716
	.1451	.3042	.2771	.1996
	.2859	.5099	.4484	.3639
	.4807	.7486	.6681	.5660
	.7300	1.0190	.9345	.8064
	.9933	1.2762	1.2030	1.0427
	1.2728	1.5201	1.4761	1.2680
	1.5734	1.7447	1.7581	1.4736
	1.8992	1.9417	2.0522	1.6515
	2.2558	2.0899	2.3594	1.8018
	2.6231	2.1863	2.6859	1.9241
	2.9919	2.2390	3.0267	2.0204
	3.3592	2.2729	3.3769	2.0979
	3.7240	2.2887	3.7326	2.1493
	4.0880	2.2985	4.0913	2.1808
	4.4519	2.3038	4.4507	2.1914
	4.7555	2.3034	4.7491	2.1832
	4.9993	2.2970	4.9062	2.1638
	5.1828	2.2861	5.1618	2.1410
	5.4132	2.2627	5.4132	2.0918

(a) Coordinate axes and definition of elliptical edges.

(b) Coordinates other than for elliptical edges.

Figure 14.—Metal coordinates for stator 67B at 10-, 50-, and 90-percent spans.

INLET THROTTLE VALVES

ORIFICE

FLOW

COLLECTOR

COLLECTOR SLEEVE VALVE

GEAR BOX

TEST STAGE

PLENUM

DRIVE MOTOR

VACUUM EXHAUSTER PIPING

ATMOSPHERIC EXHAUSTER PIPING
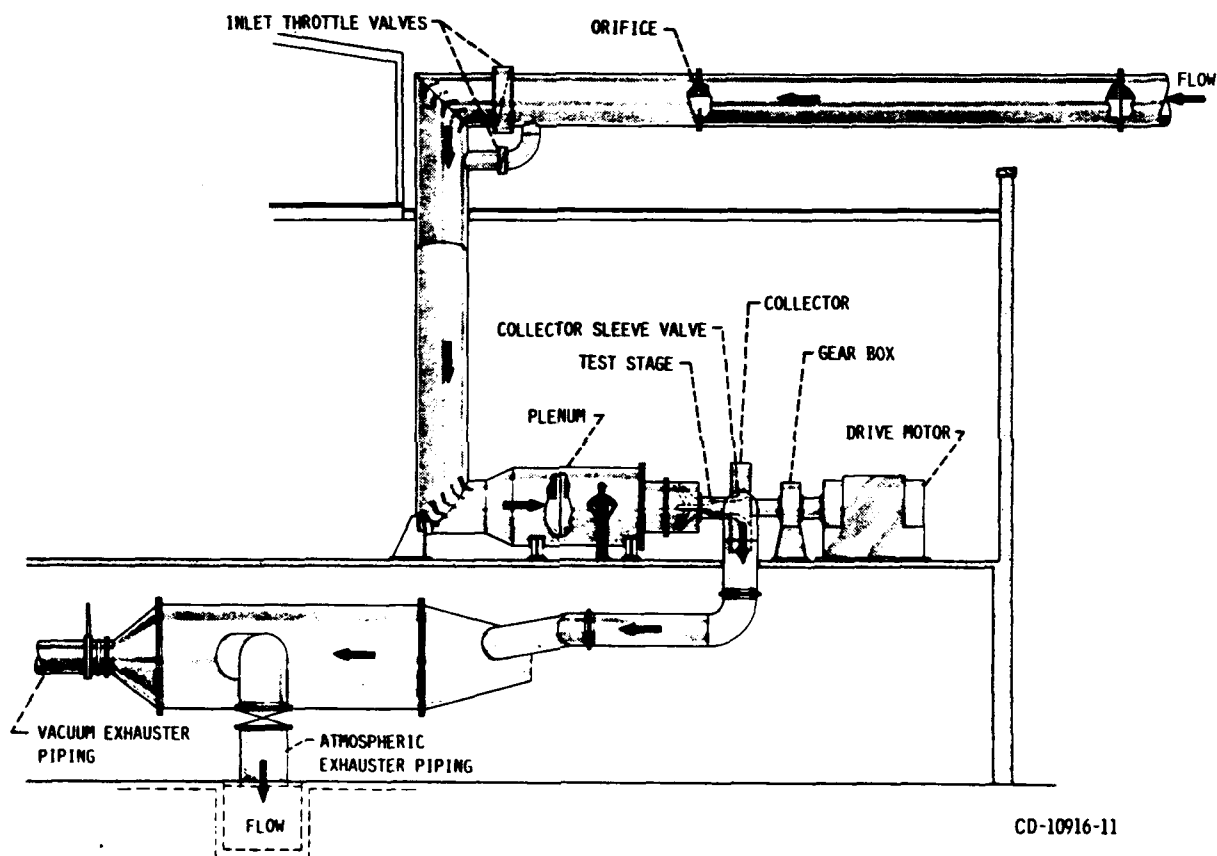
FLOW

CD-10916-11

Figure 15.—Compressor test facility.
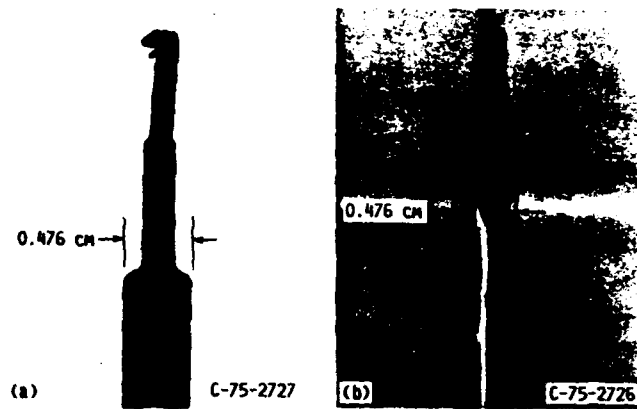
(a) Combination probe (total pressure, temperature, and flow angle).
(b) Wedge probe (static pressure).

Figure 16.—Traverse probes.

SUCTION SURFACE TAP NUMBER	CHORDWISE FRACTION, x'/C
1	0.05
2	.10
3	.20
4	.30
5	.35
6	.40
7	.45
8	.50
9	.55
10	.60
11	.75
12	.80
13	.85
14	.90
15	.95

PRESSURE SURFACE TAP NUMBER	CHORDWISE FRACTION, x'/C
1	0.05
2	.15
3	.25
4	.35
5	.50
6	.65
7	.80
8	1.00
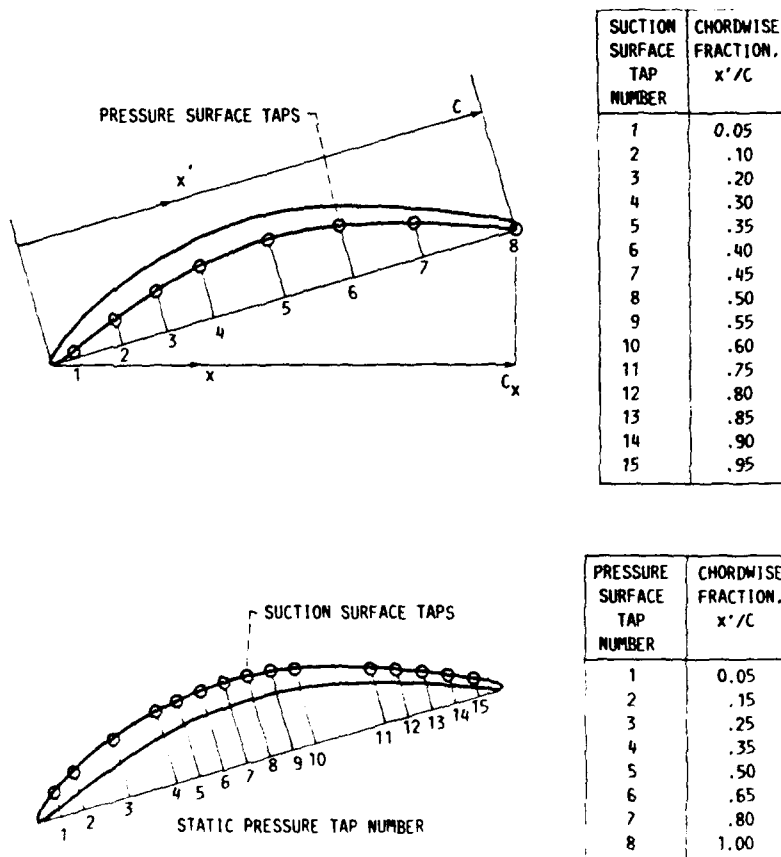
Figure 17.—Chordwise distribution of static pressure taps along design streamlines at 10-, 50-, and 90-percent span for stator 67B

47

Figure 18 (left)

SPEED,
N_D,
PERCENT
OF DESIGN

O 100
□ 95
◇ 90

OPEN SYMBOLS DENOTE STAGE 67B
WITH w_{CHOKE} OF 34.95 KG/SEC
SOLID SYMBOLS DENOTE STAGE 67
WITH w_{CHOKE} OF 35.1 KG/SEC
CROSS DENOTES DESIGN VALUES

(a) ADIABATIC EFFICIENCY, η_{ad} — .9, .8, .7

(b) TOTAL TEMPERATURE RATIO, $\overline{T_3/T_1}$ — 1.2, 1.1, 1.0

(c) TOTAL PRESSURE RATIO, $\overline{P_3/P_1}$ — 1.7, 1.6, 1.5, 1.4, 1.3

NEAR STALL LINE,
EITHER STAGE

STAGE 67B

STAGE 67

EQUIVALENT WEIGHT FLOW, FRACTION OF CHOKED
VALUE AT DESIGN SPEED
.76 .80 .84 .88 .92 .96 1.00

(a) Adiabatic efficiency, η_{ad}
(b) Total temperature ratio, $\overline{T_3/T_1}$.
(c) Total pressure ratio, $\overline{P_3/P_1}$.

Figure 18 —Overall performance for stages 67B and 67 over range of flows and speeds.

Figure 19 (right)

SPEED,
N_D,
PERCENT
OF DESIGN

O 100
□ 95
◇ 90

OPEN SYMBOLS DENOTE STAGE 67B
WITH w_{CHOKE} OF 34.95 KG/SEC
SOLID SYMBOLS DENOTE STAGE 67
WITH w_{CHOKE} OF 35.1 KG/SEC
CROSS DENOTES DESIGN VALUES

(a) ADIABATIC EFFICIENCY, η_{ad} — 1.0, .9, .8, .7

(b) TOTAL TEMPERATURE RATIO, $\overline{T_3/T_1}$ — 1.2, 1.1, 1.0

(c) TOTAL PRESSURE RATIO, $\overline{P_2/P_1}$ — 1.7, 1.6, 1.5, 1.4, 1.3, 1.2

ROTOR 67
WITH STATOR 67B

ROTOR 67
WITH STATOR 67

EQUIVALENT WEIGHT FLOW FRACTION OF CHOKED
VALUE AT DESIGN SPEED
.76 .80 .84 .88 .92 .96 1.00

(a) Adiabatic efficiency, η_{ad}.
(b) Total temperature ratio, $\overline{T_3/T_1}$.
(c) Total pressure ratio, $\overline{P_2/P_1}$.

Figure 19.—Overall performance for rotor 67 over range of flows and speeds.

Figure 21 legend (right, top):

STATOR	AIRFLOW FRACTION, w/w_{CHOKE}	CHOKED FLOW, w_{CHOKE}, KG/SEC	READING
○ 67B	0.993	34.95	2609
□ 67B	.985	35.1	DESIGN

(a)

1.7

1.6

1.5

1.4

PRESSURE RATIOED TO STANDARD DAY VALUE, 10.13 N/cm^2

(b)

1.3

1.2

1.1

1.0

.9

(c)

60

50

40

30

AIR ANGLE, DEG, $\tan^{-1}(M_\theta/M_m)$

0   20   40   60   80   100
TIP   HUB
PERCENT SPAN

(a) Total pressure ratioed to standard day value, 10.13 N/cm^2.
(b) Static pressure ratioed to standard day value, 10.13 N/cm^2.
(c) Air angle, deg, $\tan^{-1}(M_\theta/M_m)$.
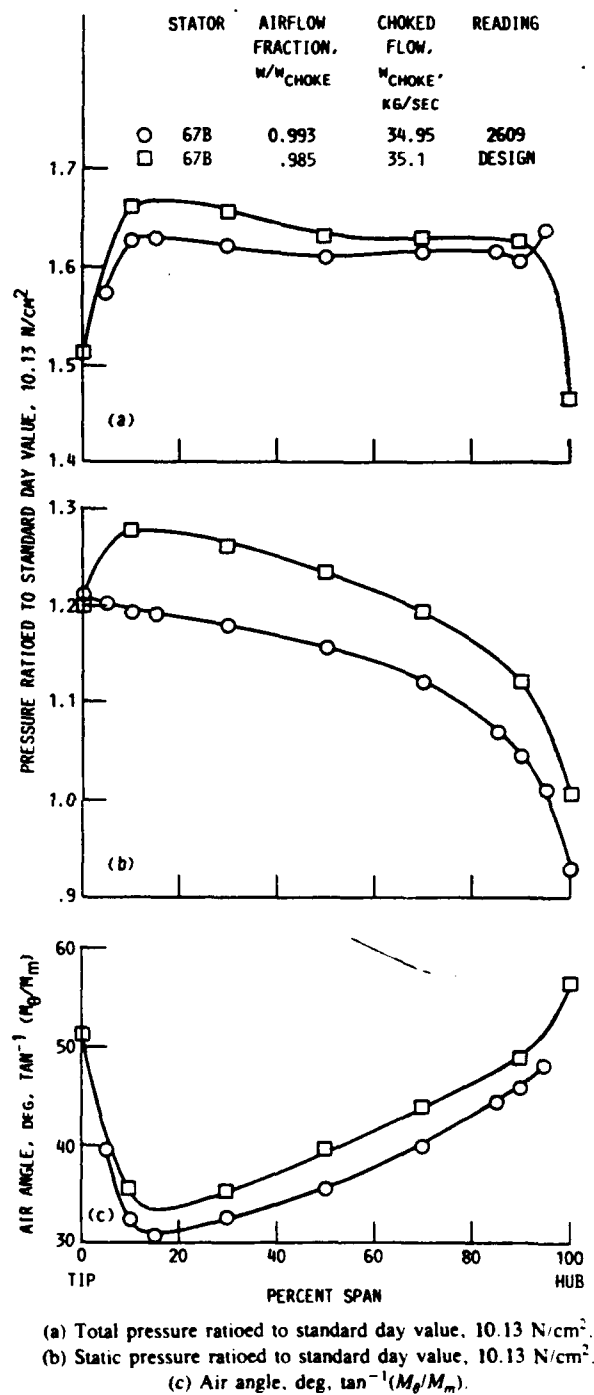
Figure 21.—Comparison of stator 67B inlet conditions (station 2) across span at design speed with design intent.

Figure 20 legend (left):

SPEED, N_D, PERCENT OF DESIGN	MINIMUM $\Delta\eta$ (FAIRED) STAGE 67B	STAGE 67
○ 100	0.046	0.028
□ 95	.043	-----
◇ 90	.043	.031

OPEN SYMBOLS DENOTE STAGE 67B WITH w_{CHOKE} OF 34.95 KG/SEC
SOLID SYMBOLS DENOTE STAGE 67 WITH w_{CHOKE} OF 35.1 KG/SEC
CROSS DENOTES DESIGN VALUES

.16

.12

.08

.04

0

ROTOR MINUS STAGE EFFICIENCY (STATOR EFFICIENCY DROP), $\Delta\eta$

.76   .80   .84   .88   .92   .96   1.00
EQUIVALENT WEIGHT FLOW, FRACTION OF CHOKED VALUE AT DESIGN SPEED

STAGE 67B
STAGE 67

Figure 20 —Overall rotor minus stage efficiency over range of flows and speed.

49

STATOR	AIRFLOW FRACTION, W/W_{CHOKE}	CHOKED FLOW, W_{CHOKE}, KG/SEC	READING
◯ 67B	0.993	34.95	2609
☐ 67B	.985	35.1	DESIGN

(d)

(e)

(f)

MACH NUMBER

TIP

PERCENT SPAN

HUB
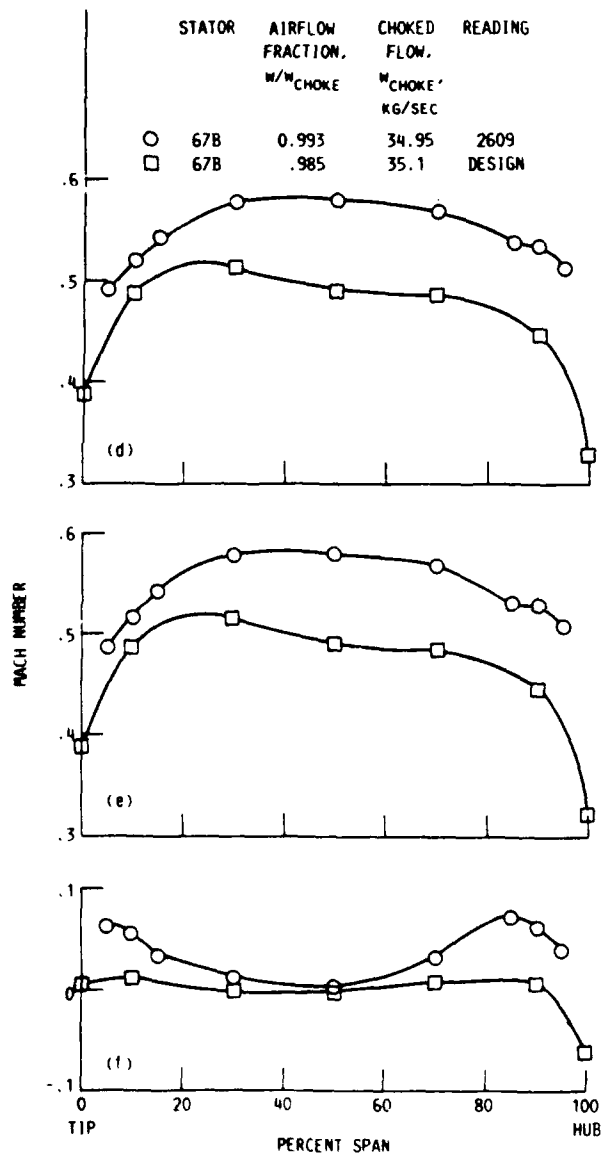
(d) Absolute Mach number, M
(e) Meridonal Mach number, M_m.
(f) Tangential Mach number, M_t.

Figure 21.—Concluded.

STATOR	AIRFLOW FRACTION, W/W_{CHOKE}	CHOKED FLOW, W_{CHOKE}, KG/SEC	READING
◯ 67B	0.993	34.95	2609
☐ 67B	.985	35.1	DESIGN

PRESSURE RATIOED TO STANDARD DAY VALUE, 10.13 N/cm²

(a)

(b)

AIR ANGLE, DEG, $\tan^{-1}$ (M_θ/M_m)

(c)

TIP

PERCENT SPAN

HUB

(a) Total pressure ratioed to standard day value, 10.13 N/cm².
(b) Static pressure ratioed to standard day value, 10.13 N/cm².
(c) Air angle, deg, $\tan^{-1}$ (M_θ/M_m).

Figure 22.—Comparison of stator 67B outlet conditions (station 3) across span at design speed with design intent.

(d) Absolute Mach number. M

(e) Meridional Mach number. M_m

(f) Tangential Mach number. M_θ

Figure 22 —Concluded

(a) Total pressure ratioed to standard day value. 10.13 N/cm².

(b) Static pressure ratioed to standard day value. 10.13 N/cm².

(c) Air angle, deg. $\tan^{-1}(M_\theta/M_m)$.

Figure 23.—Comparison of stator 67B inlet conditions (station 2) across span with those for stator 67 at some weight flow at design speed.

51

STATOR	AIRFLOW FRACTION, W/W_{CHOKE}	CHOKED FLOW, W_{CHOKE}, KG/SEC	READING
○ 67B	0.976	34.95	2618
□ 67	.972	35.1	383

(d) Absolute Mach number, M.
(e) Meridional Mach number, M_m.
(f) Tangential Mach number, M_θ.

Figure 23.—Concluded.

(a) Total pressure ratioed to standard day value, 10.13 N/cm².
(b) Static pressure ratioed to standard day value, 10.13 N/cm².
(c) Air angle, deg, $\tan^{-1}(M_\theta/M_m)$.
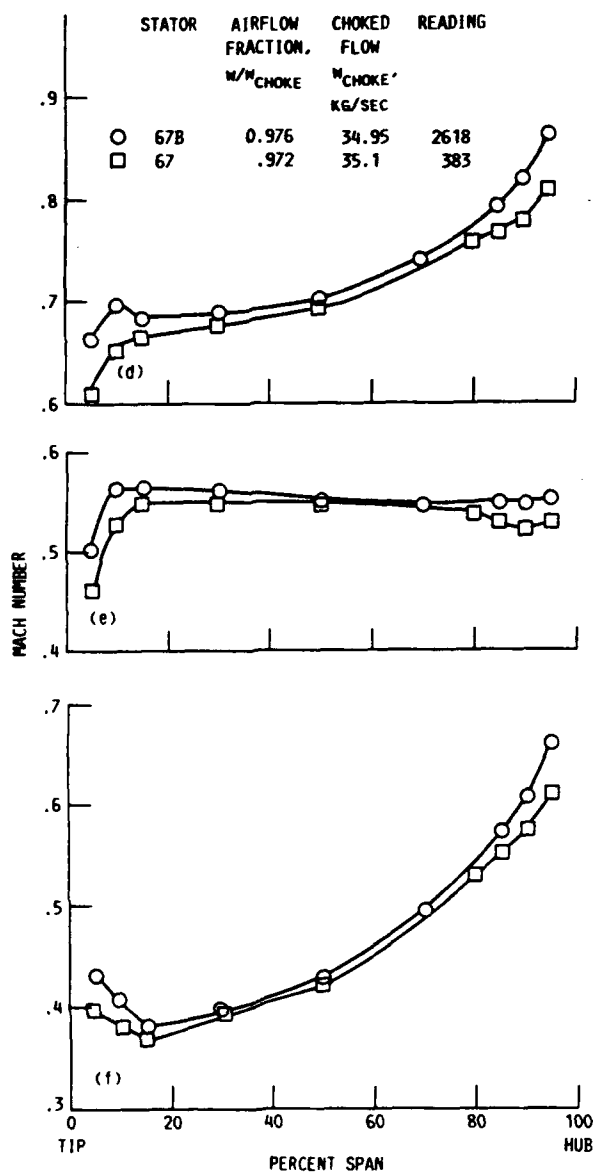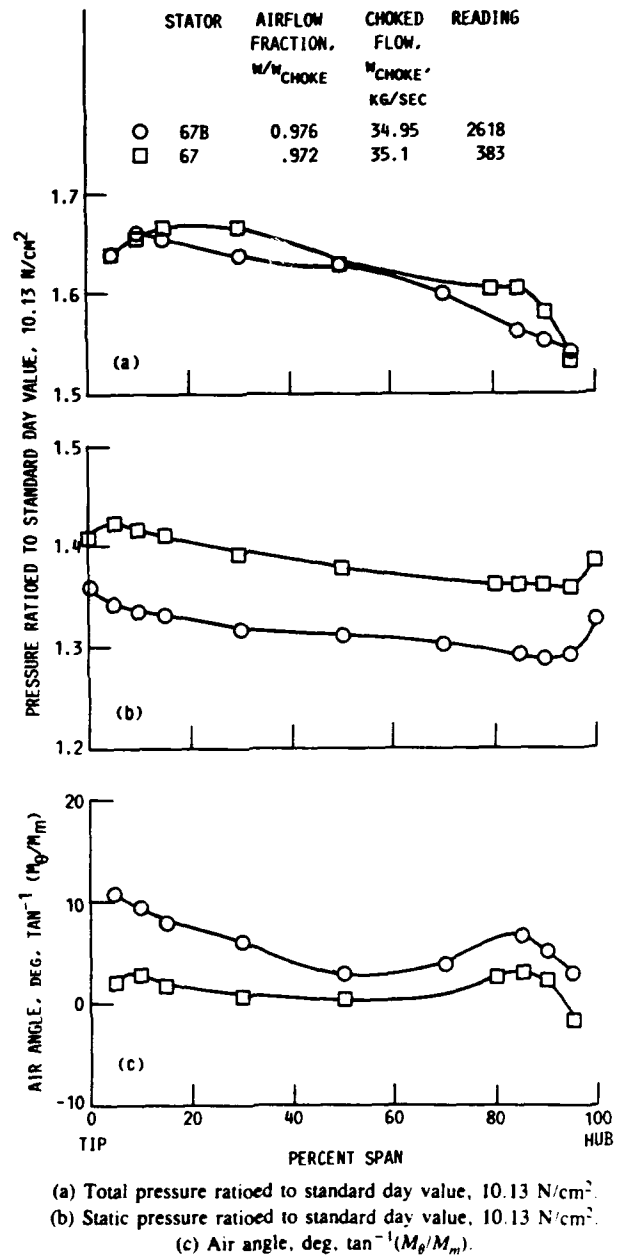
Figure 24.—Comparison of stator 67B outlet conditions (station 3) across span with those for stator 67 at same weight flow at design speed.
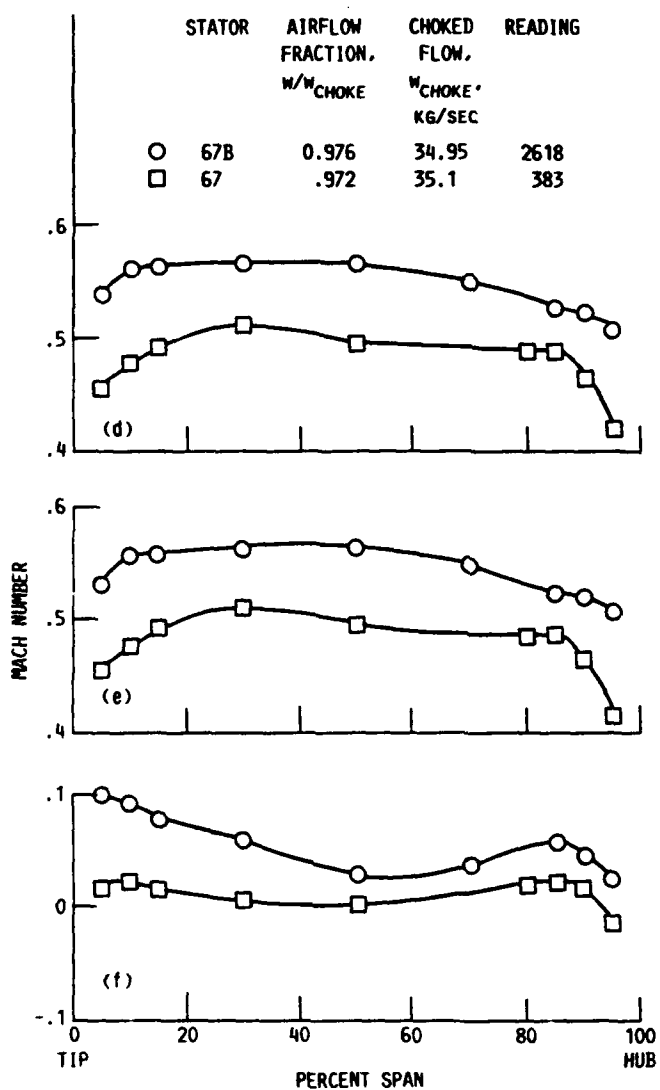
	STATOR	AIRFLOW FRACTION, w/w_{CHOKE}	CHOKED FLOW, w_{CHOKE}, KG/SEC	READING
O	67B	0.976	34.95	2618
□	67	.972	35.1	383

(d) Absolute Mach number, M.
(e) Meridonal Mach number, M_m.
(f) Tangential Mach number, M_θ.

Figure 24.—Concluded.

SPEED,
N_D,
PERCENT
OF DESIGN

○ 100
□ 95
◇ 90

OPEN SYMBOLS DENOTE STAGE 67B
WITH w_{CHOKE} OF 34.95 KG/SEC
SOLID SYMBOLS DENOTE STAGE 67
WITH w_{CHOKE} OF 35.1 KG/SEC
CROSS DENOTES DESIGN VALUES

(a) Tip, 10-percent span.
(b) Thirty-percent span.
(c) Mean, 50-percent span.
(d) Seventy-percent span.
(e) Hub, 90-percent span.
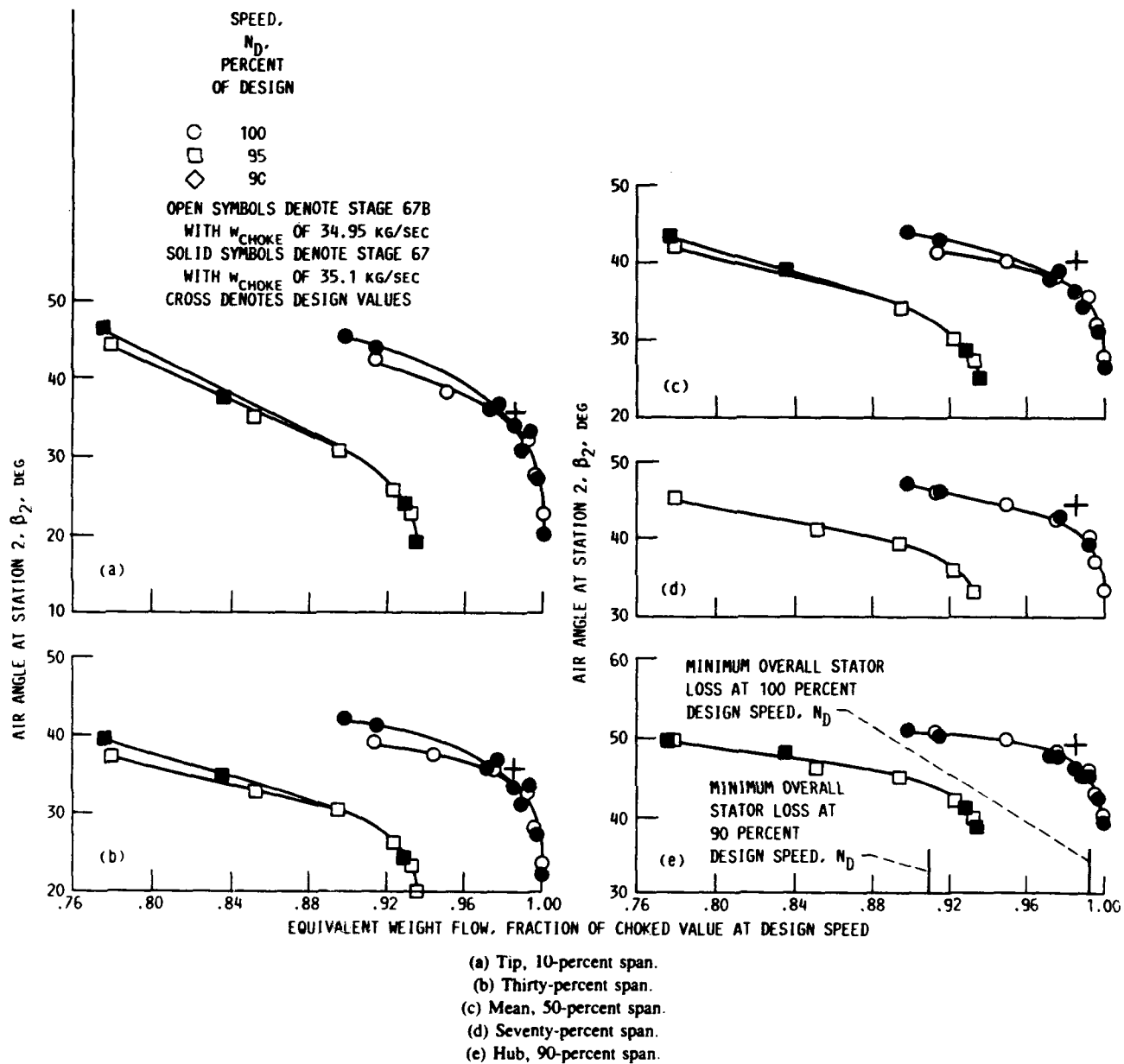
Figure 25.—Stator inlet air angles (station 2) at five spanwise locations over range of flows and speeds.
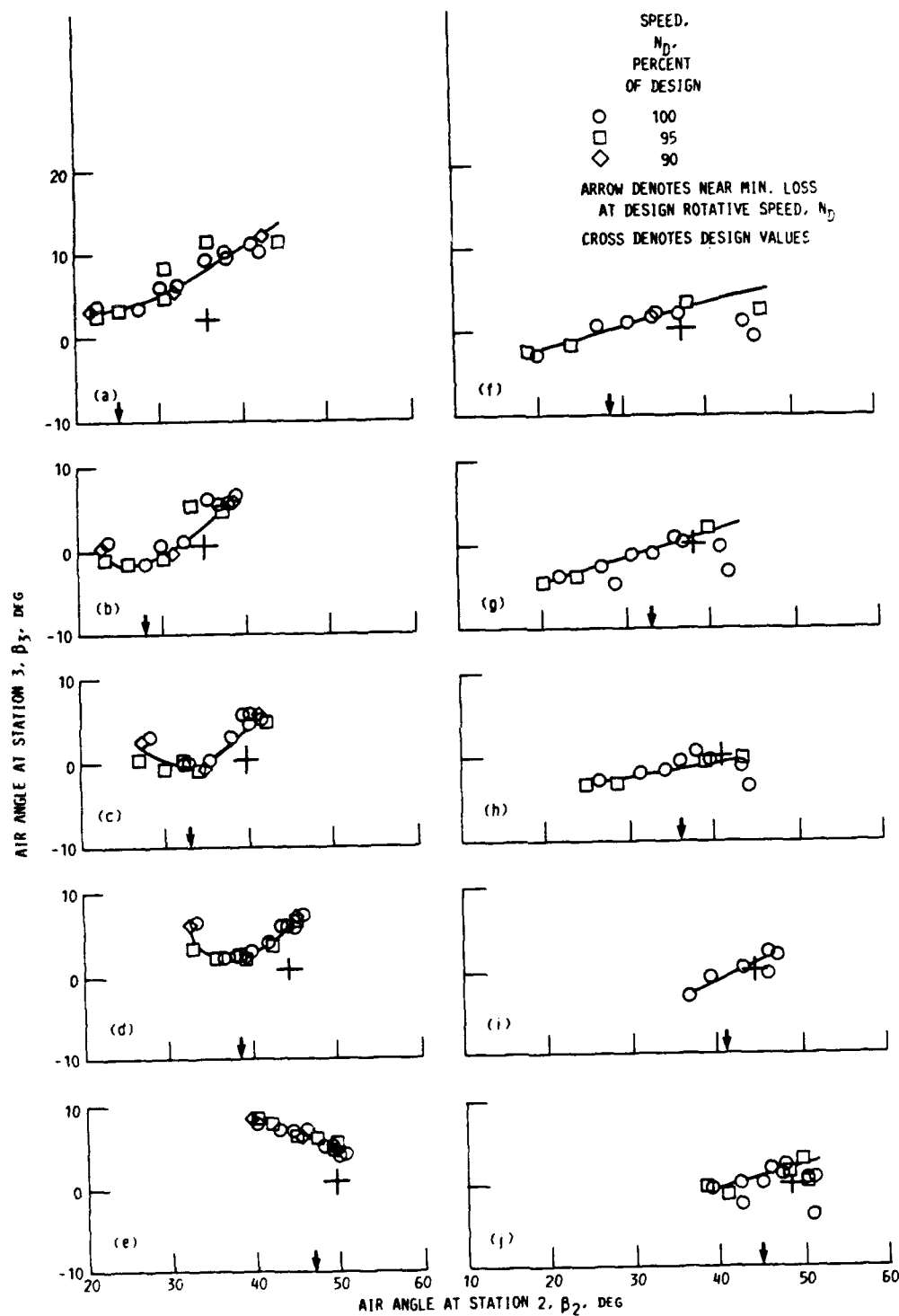
54

Figure 26 —Stator outlet air angles (station 3) at five spanwise locations over range of inlet air angles (station 2) and speeds
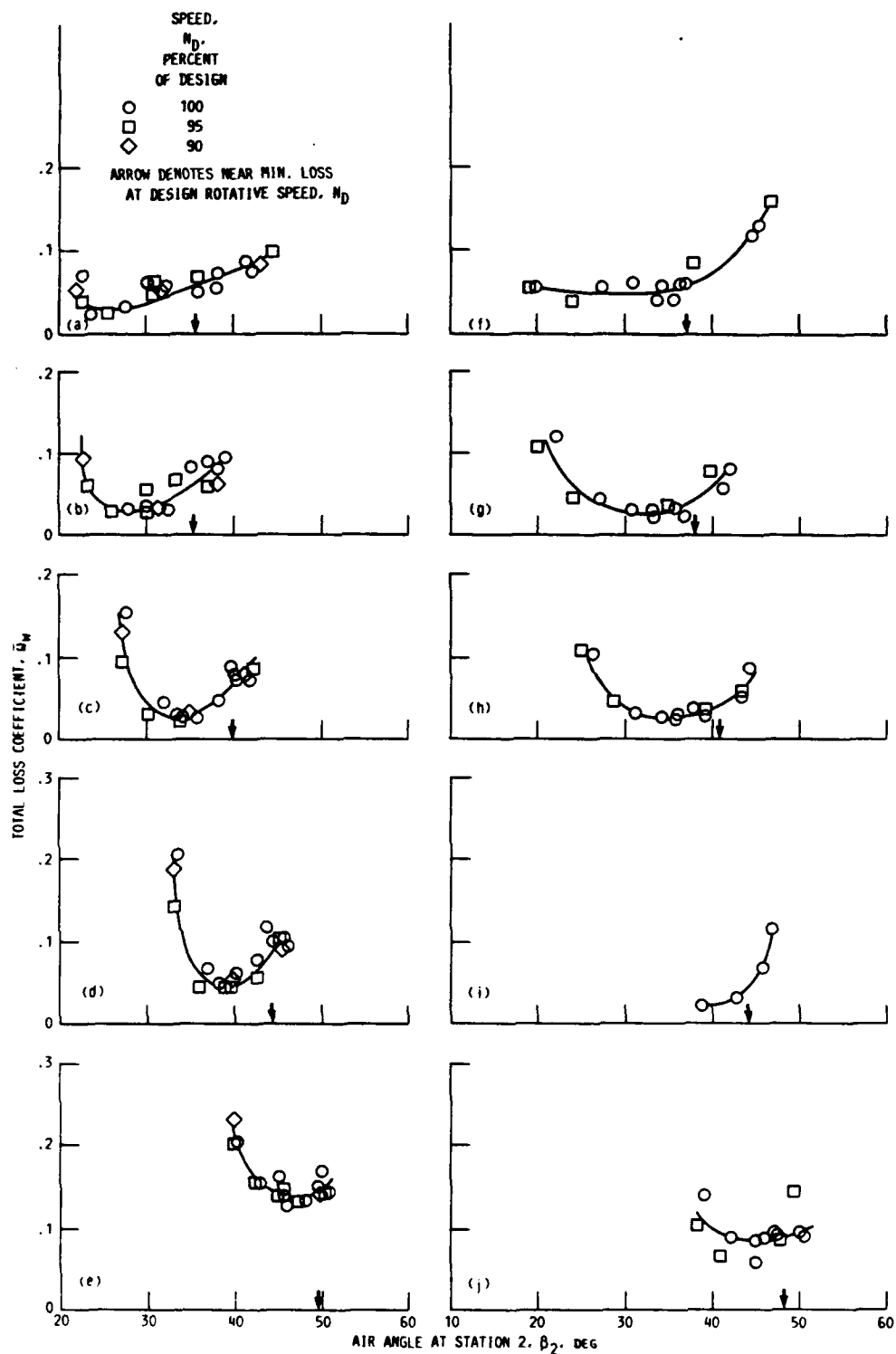
(a) Stator 67B, 10-percent span (tip).
(b) Stator 67B, 30-percent span.
(c) Stator 67B, 50-percent span (mean).
(d) Stator 67B, 70-percent span
(e) Stator 67B, 90-percent span (hub).

(f) Stator 67, 10-percent span (tip).
(g) Stator 67, 30-percent span.
(h) Stator 67, 50-percent span (mean).
(i) Stator 67, 70-percent span.
(j) Stator 67, 90-percent (hub).

Figure 27 —Stator losses at five spanwise locations over range of inlet air angles (station 2) and speeds.

(a) Stator 67B, 10-percent span (tip).
(b) Stator 67B, 30-percent span.
(c) Stator 67B, 50-percent span (mean).
(d) Stator 67B, 70-percent span.
(e) Stator 67B, 90-percent span (hub).

(f) Stator 67, 10-percent span (tip).
(g) Stator 67, 30-percent span.
(h) Stator 67, 50-percent span (mean).
(i) Stator 67, 70-percent span.
(j) Stator 67, 90-percent (hub).
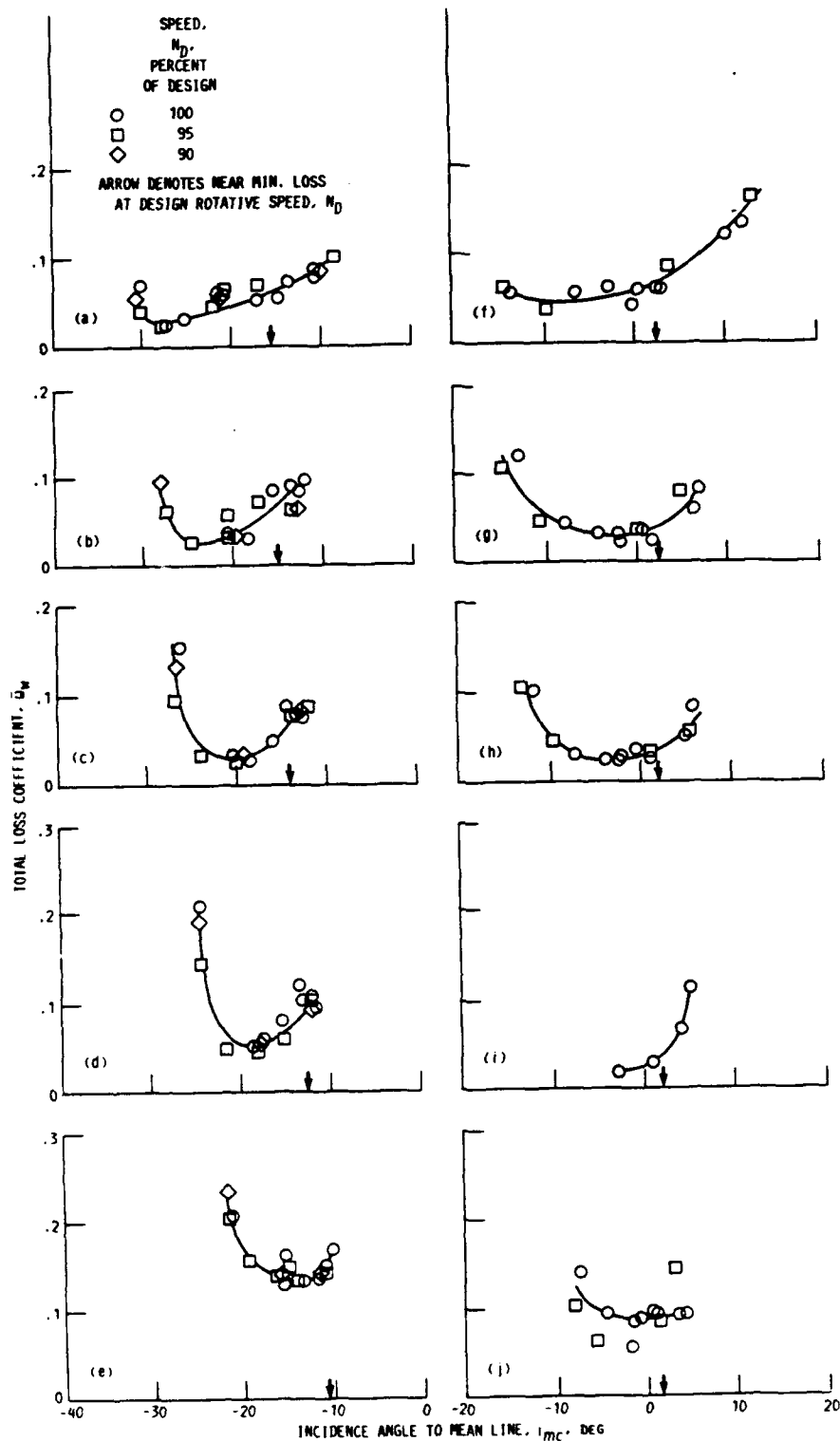
(a) Stator 67 B, 10-percent span (tip).
(b) Stator 67B, 30-percent span.
(c) Stator 67B, 50-percent span (mean).
(d) Stator 67B, 70-percent span.
(e) Stator 67B, 90-percent span (hub).

(f) Stator 67, 10-percent span (tip).
(g) Stator 67, 30-percent span.
(h) Stator 67, 50-percent span (mean).
(i) Stator 67, 70-percent span.
(j) Stator 67, 90-percent (hub).

Figure 28.—Stator losses at five spanwise locations over range of incidence angles and speeds.
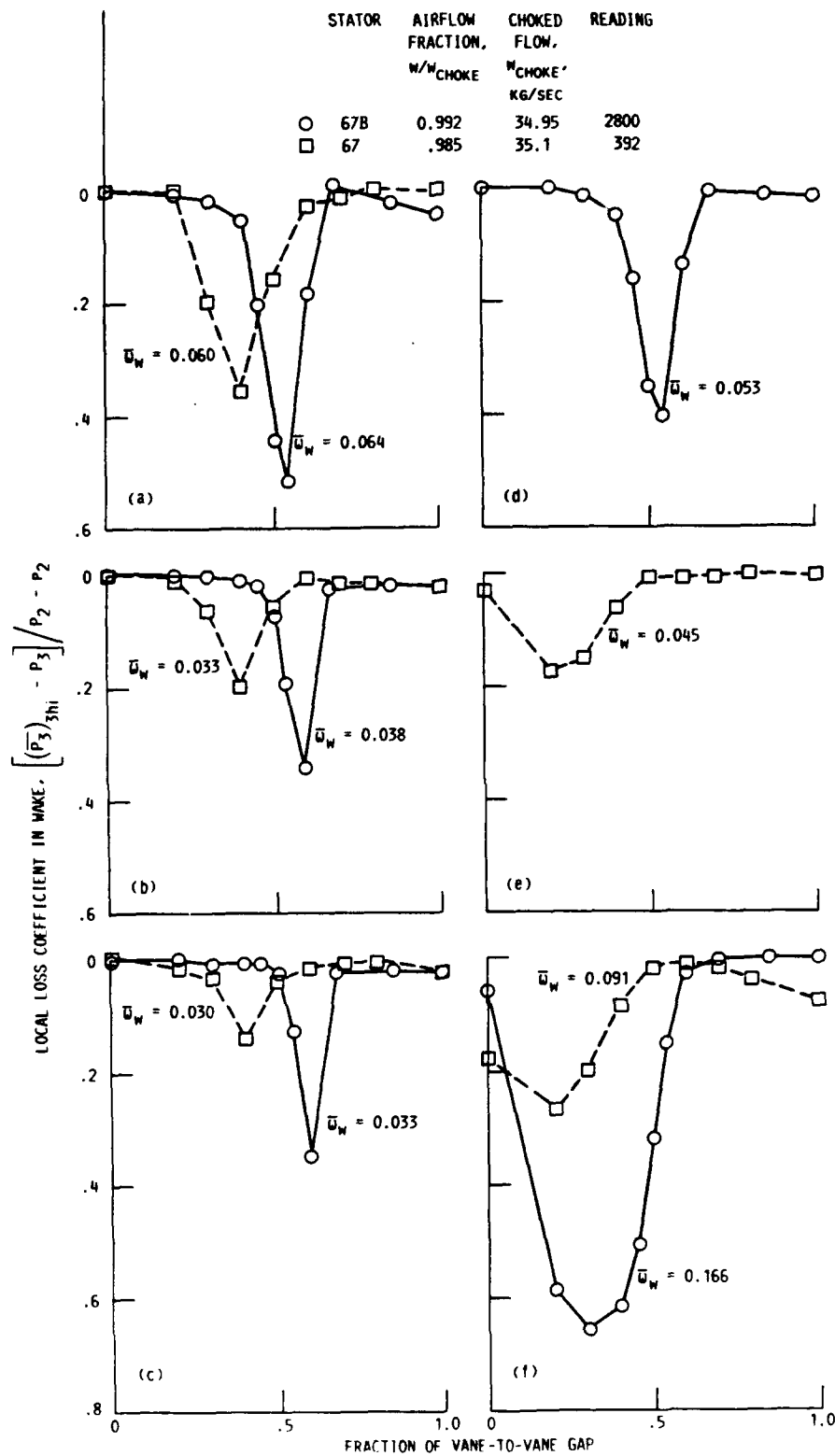
STATOR	AIRFLOW FRACTION, w/w_{CHOKE}	CHOKED FLOW, w_{CHOKE}, KG/SEC	READING
O 67B	0.992	34.95	2800
□ 67	.985	35.1	392

LOCAL LOSS COEFFICIENT IN WAKE, $\left[\left(\overline{P_3}\right)_{3hi} - P_3\right]/\overline{P_2 - P_2}$

FRACTION OF VANE-TO-VANE GAP

(a) Ten-percent span (tip).
(b) Thirty-percent span
(c) Fifty-percent span (mean).

(d) Seventy-percent span.
(e) Eighty-percent span
(f) Ninety-percent span (hub)

Figure 29 —Comparison of wake profiles across span of stator 67B with stator 67 Near peak stage efficiency operation at design speed

(a) Ten-percent span (tip).
(b) Thirty-percent span
(c) Fifty-percent span (mean).
(d) Seventy-percent span
(e) Ninety-percent span (hub).
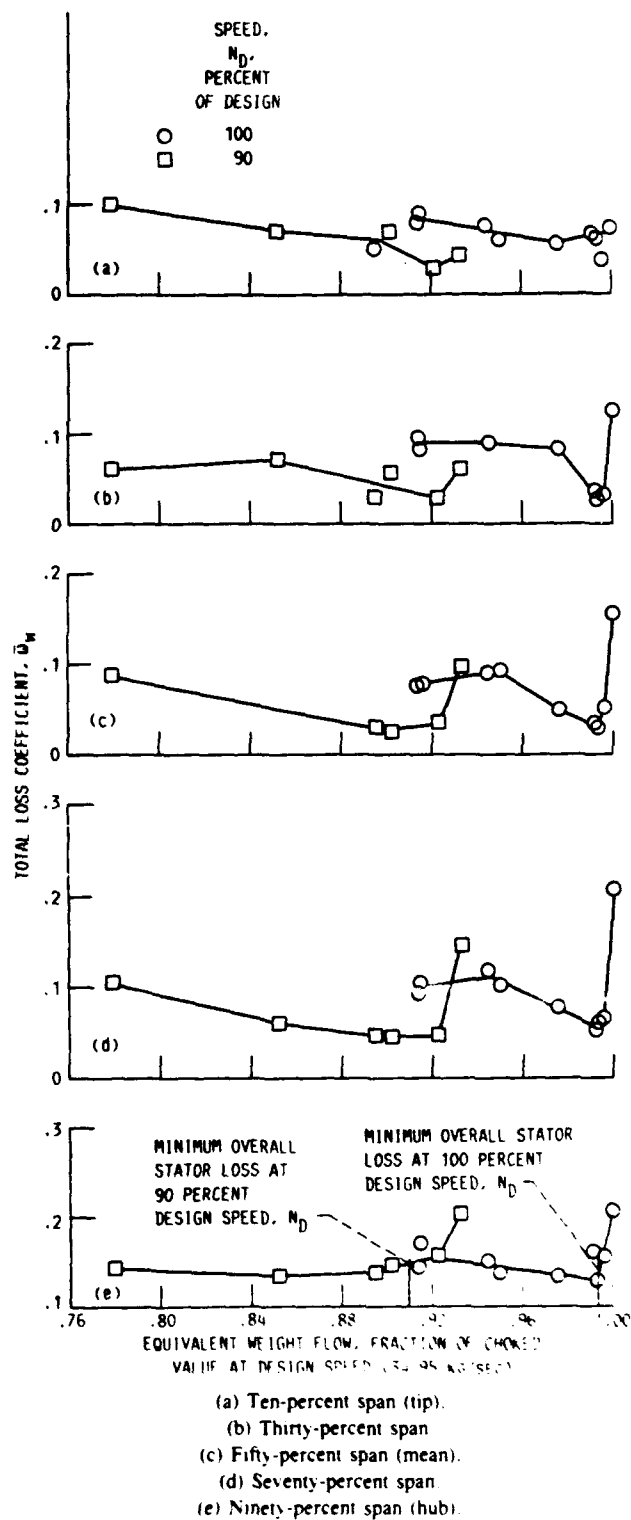
Figure 30.—Determination of minimum overall stator 67B losses at 90- and 100-percent of design

(a) Ten-percent span (tip).
(b) Thirty-percent span.
(c) Fifty-percent span (mean).
(d) Seventy-percent span.
(e) Ninety-percent span (hub).
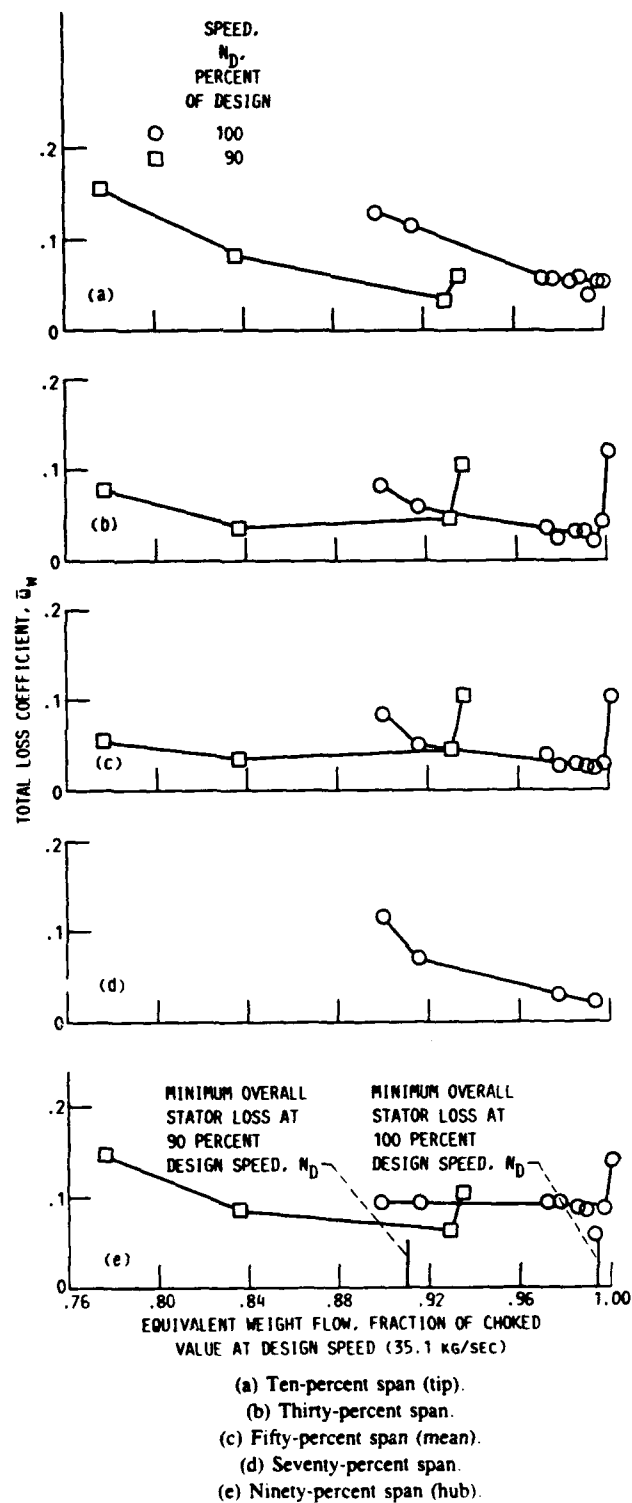
Figure 31.—Determination of minimum overall stator 67 losses at 90- and 100-percent design speed.
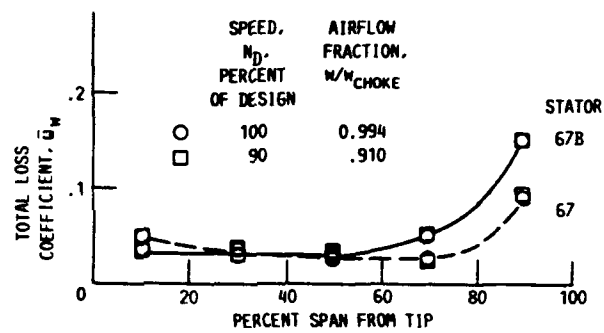
Figure 32.—Spanwise distributions of faired loss coefficients for stator 67B (17 vanes) and stator 67 (34 vanes) at their best operating points at 90- and 100-percent design speed.

SPEED, N_D, PERCENT OF DESIGN	AIRFLOW FRACTION, W/W_{CHOKE}	STATOR EFFICIENCY DROP, $\Delta\eta$	READING	MACH NUMBER, M_2	AIR ANGLE, DEG β_2	β_3	WAKE TOTAL-LOSS COEFFICIENT, $\bar{\omega}_W$
100	0.993	0.041	2609	0.68	32.3	6.3	0.058
95	.947	.045	2658	.65	31.8	5.4	.054
90	.895	.031	2687	.61	30.6	4.8	.047
100	.985	.026	DESIGN	.62	35.5	1.6	.060

DESIGN PREDICTION

AERO MEASUREMENT

(a)

(b)

0.70	35.6	0.3	0.029
.67	34.8	-.5	.034
.63	34.0	-1.0	.030
.64	39.7	-.3	.030

0.81	45.9	6.9	0.131
.78	45.5	6.7	.142
.75	45.1	6.3	.140
.75	49.0	.8	.090

(c)

FRACTION OF AXIAL CHORD, x/c_x

SURFACE PRESSURE COEFFICIENT, C_p

(a) Ten-percent span (tip).
(b) Fifty-percent span (mean).
(c) Ninety-percent span (hub).

Figure 33 —Surface pressure distributions for tip. mean. and hub sections of stator 67B operating near its best efficiency flows at 90-, 95-, and 100-percent design speed. Equivalent weight flow, $[w\sqrt{\theta}\,\delta]_{choke}$ = 34.95 kg sec.

61

	SPEED N_p, PERCENT OF DESIGN	AIRFLOW FRACTION, W/W_{CHOKE}	STATOR EFFICIENCY DROP, $\Delta\eta$	READING	MACH NUMBER, M_2	AIR ANGLE, DEG $\dot{\beta}_2$	β_3	WAKE TOTAL-LOSS COEFFICIENT $\bar{\xi}_w$
O	90	0.923	0.035	2745	0.61	25.7	3.4	0.025
□	90	.895	.031	2687	.61	30.6	4.8	.047
--	100	.985	.026	DESIGN	.62	35.5	1.6	.060

DESIGN PREDICTION

AERO MEASUREMENT

					0.64	30.0	-0.7	0.034
					.63	34.0	-1.0	.030
					.64	39.7	-.3	.030

					0.77	42.1	7.9	0.159
					.75	45.1	6.3	.140
					.75	49.0	.8	.090

SURFACE PRESSURE COEFFICIENT, C_p

FRACTION OF AXIAL CHORD, x/C_x

(a) Ten-percent span (tip)
(b) Fifty-percent span (mean).
(c) Ninety-percent span (hub).

Figure 34 —Surface pressure distributions for tip, mean, and hub sections of stator 67B operating near its best efficiency flows at 90-percent design speed. Equivalent weight flow $[w \sqrt{\theta}\,\delta]_{choke} = 34.95$ kg/sec.

62

	AIRFLOW FRACTION, w/w_{CHOKE}	STATOR EFFICIENCY DROP, $\Delta\eta$	READING	MACH NUMBER, M_2	AIR ANGLE, DEG β_2	AIR ANGLE, DEG β_3	WAKE TOTAL-LOSS COEFFICIENT, $\bar{\omega}_w$
O	0.923	0.035	2745	0.61	25.7	3.4	0.025
□	.895	.031	2687	.61	30.6	4.8	.047

				0.64	30.0	-.7	0.034
				.63	34.0	-1.0	.030

				0.77	42.1	7.9	0.159
				.75	45.1	6.3	.140

(a) Ten-percent span (tip)
(b) Fifty-percent span (mean).
(c) Ninety-percent span (hub)

Figure 35.—Local loss coefficients in wake for tip, mean, and hub sections of stator 67B operating near its best efficiency flows at 90-percent design speed

	AIRFLOW FRACTION, w/w_{CHOKE}	STATOR EFFICIENCY DROP, $\Delta\eta$	READING	MACH NUMBER, M_2	AIR ANGLE, DEG		WAKE TOTAL-LOSS COEFFICIENT, $\bar{\omega}_w$
					β_2	β_3	
○	0.933	0.091	2696	0.61	22.6	2.4	0.040
□	.852	.039	2754	.62	35.9	11.6	.070
△	.779	.041	2705	.63	44.3	11.2	.100
---	.985	.026	DESIGN	.62	35.5	1.6	.060

			0.66	27.1	0.1	0.097
			.62	37.1	2.1	-----
			.61	42.0	4.6	.088
			.64	39.7	-.3	.030

			0.81	39.9	8.5	0.204
			.75	47.4	6.5	.135
			.75	49.8	5.7	.144
			.75	49.0	.8	.090

(a) Ten-percent span (tip)

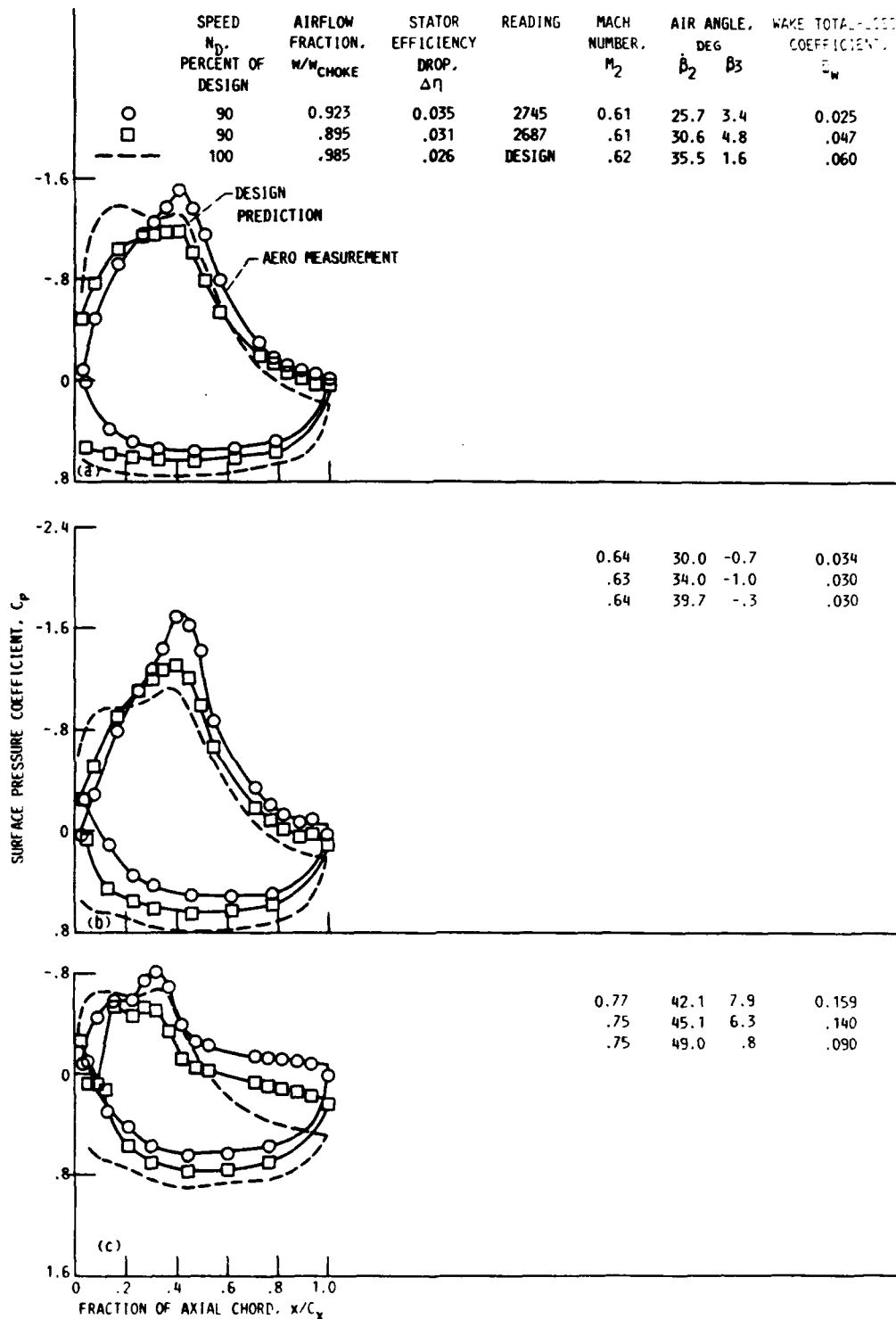(b) Fifty-percent span (mean).

(c) Ninety-percent span (hub).

Figure 36.—Surface pressure distributions for tip, mean, and hub sections of stator 67B operating at other than its best efficiency flows at 90-percent design speed. Equivalent weight flow, $(w \sqrt{\bar{\theta}} \delta)_{choke} = 34.95$ kg/sec.

	AIRFLOW FRACTION, W/W_CHOKE	STATOR EFFICIENCY DROP, Δη	READING	MACH NUMBER, M₂	AIR ANGLE, DEG β₂	β₃	WAKE TOTAL-LOSS COEFFICIENT, ω̄_w
○	0.993	0.091	2696	0.61	22.6	2.4	0.040
□	.852	.039	2754	.62	35.9	11.6	.070
△	.779	.041	2705	.63	44.3	11.2	.100

0.66	27.1	0.1	0.097
.62	37.1	2.1	-----
.61	42.0	4.6	.088

STATOR GAPWISE POSITION RELATIVE TO
WAKE MEASUREMENTS IS APPROXIMATE

0.81	39.9	8.5	0.204
.75	47.4	6.5	.135
.75	49.8	5.7	.144

(a) Ten-percent span (tip)
(b) Fifty-percent span (mean)
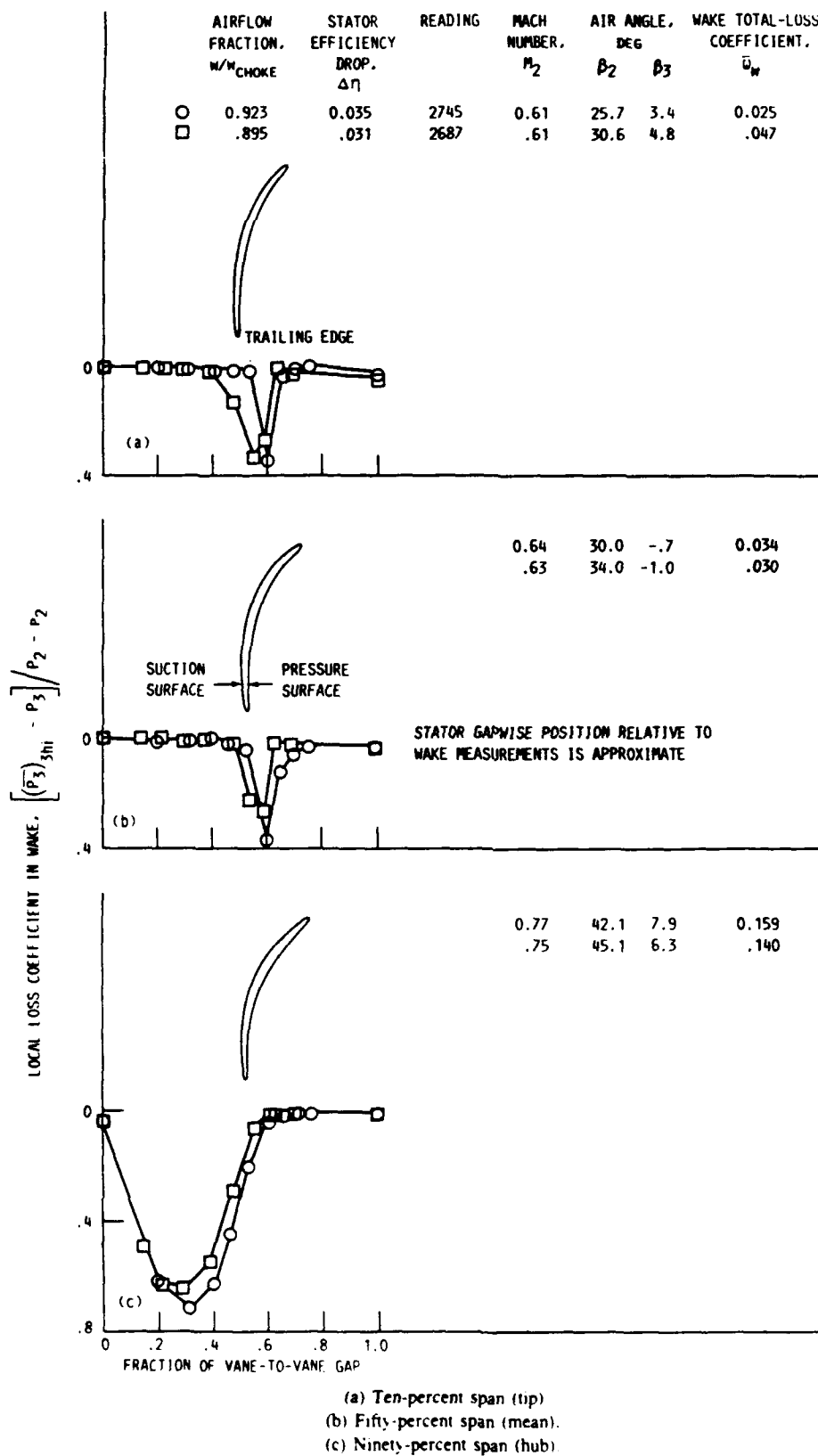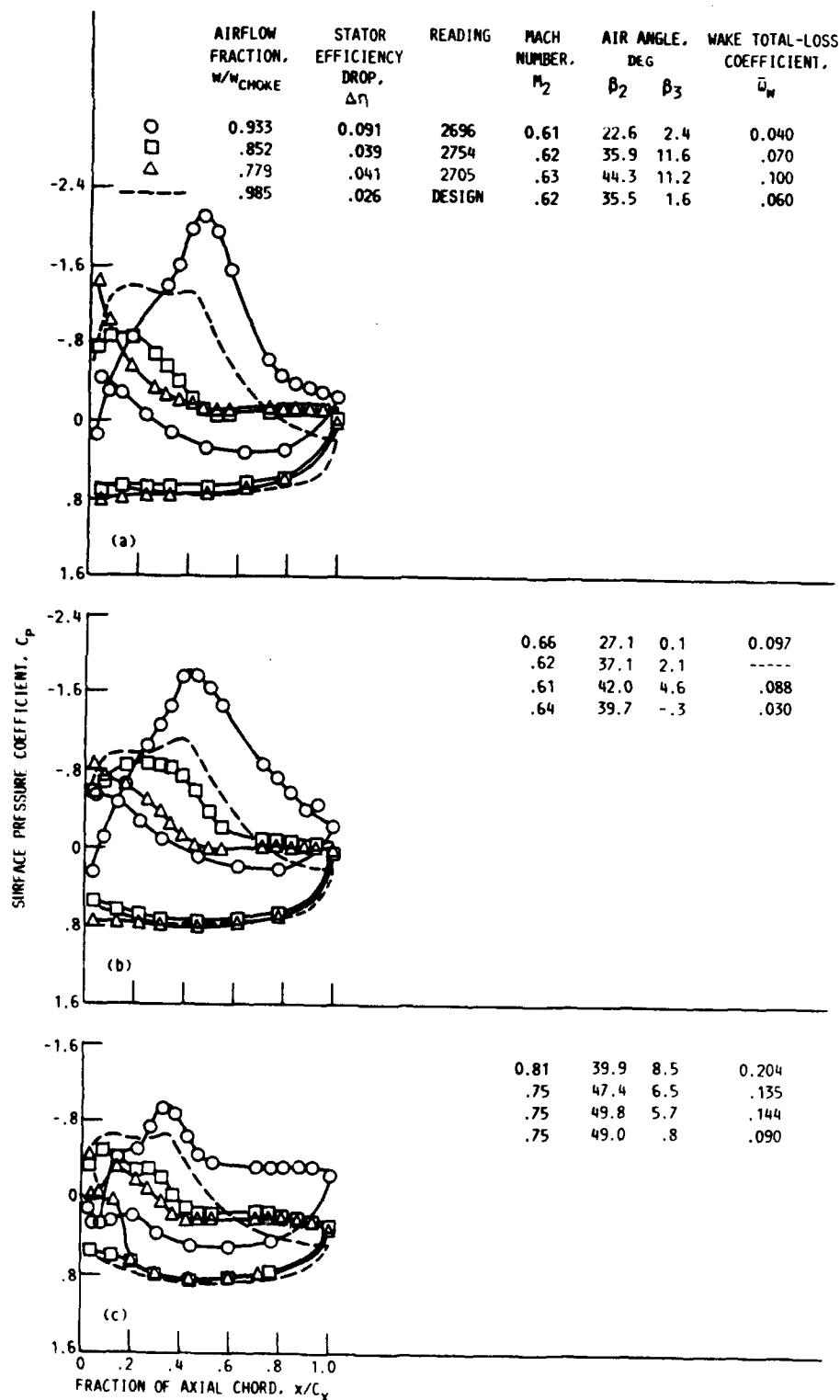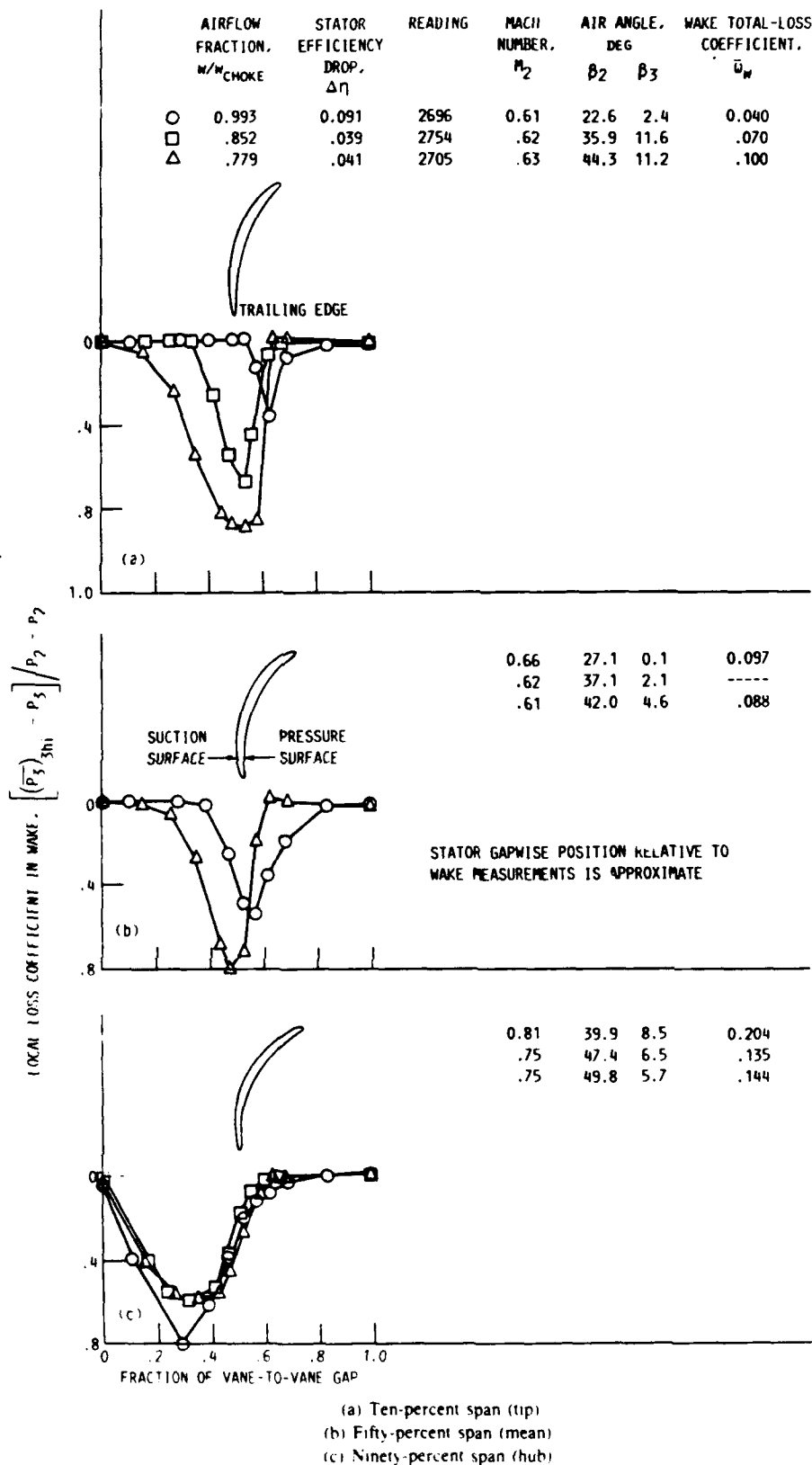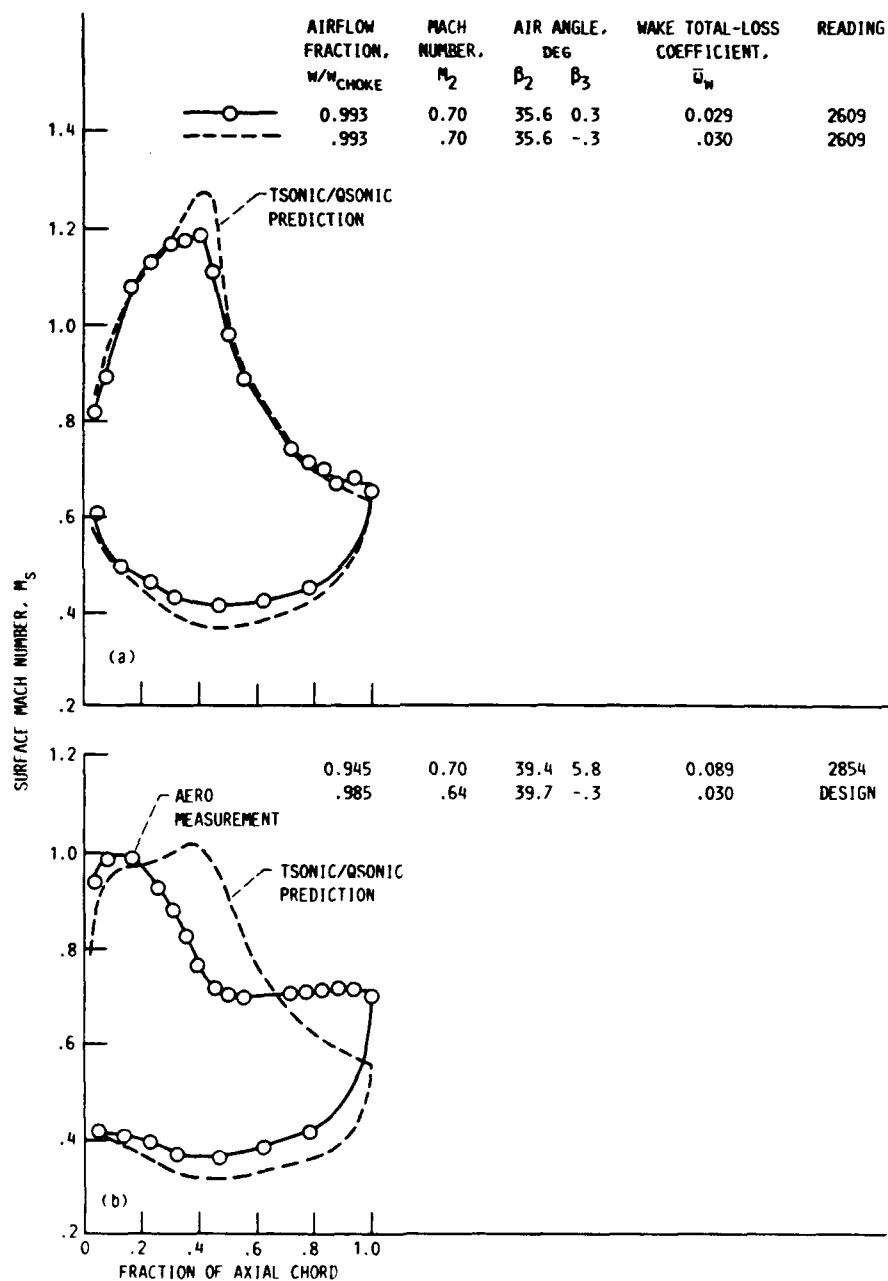(c) Ninety-percent span (hub)

Figure 37 —Local loss coefficients in wake for tip, mean, and hub sections of stator 67B operating at other than its best efficiency flows at 90-percent design speed. Equivalent weight flow to √θ/δ = 34.95 kg/sec.

		AIRFLOW FRACTION, W/W_CHOKE	MACH NUMBER, M_2	AIR ANGLE, DEG β_2	β_3	WAKE TOTAL-LOSS COEFFICIENT, ū_w	READING
—⊙—		0.993	0.70	35.6	0.3	0.029	2609
– – –		.993	.70	35.6	-.3	.030	2609
		0.945	0.70	39.4	5.8	0.089	2854
		.985	.64	39.7	-.3	.030	DESIGN

(a) Inlet air angle β_2 near minimum loss operation

(b) Inlet air angle β_2 near design

Figure 38.—Comparison of surface Mach number distributions at 50-percent span for stator 67B for an inlet air angle near design with one near minimum loss operation at 100-percent design speed.
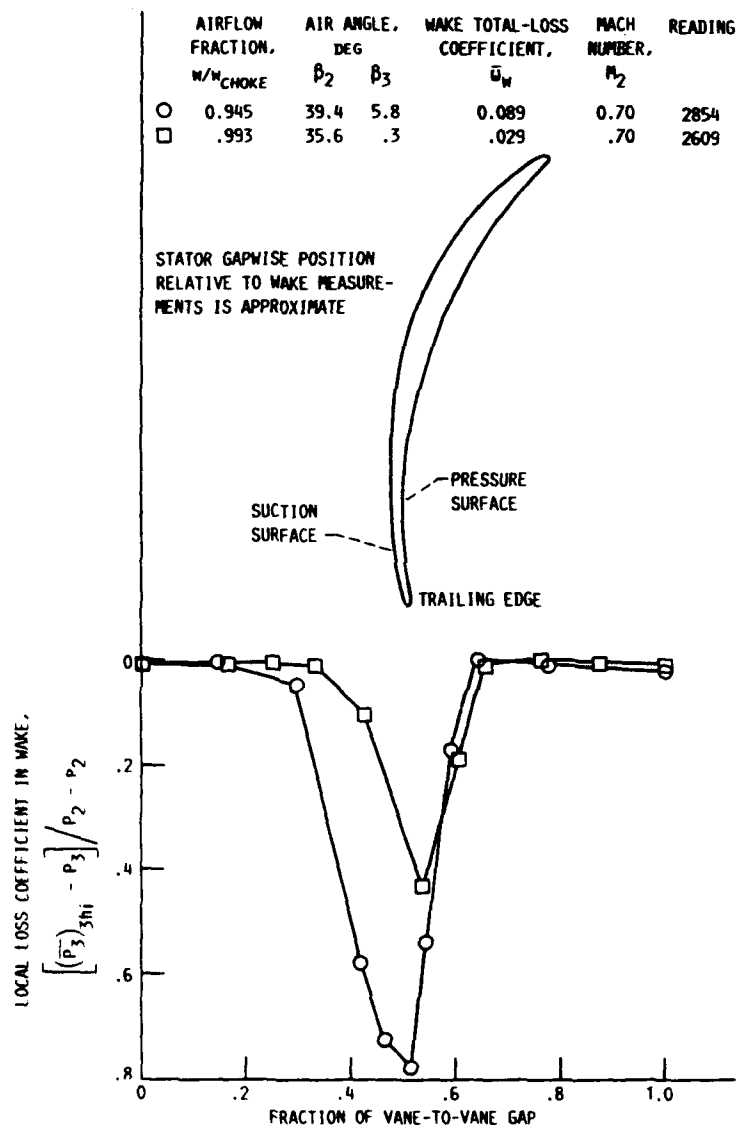
66

	AIRFLOW FRACTION, w/w_{CHOKE}	AIR ANGLE, DEG β_2	β_3	WAKE TOTAL-LOSS COEFFICIENT, $\bar{\omega}_w$	MACH NUMBER, M_2	READING
O	0.945	39.4	5.8	0.089	0.70	2854
□	.993	35.6	.3	.029	.70	2609

STATOR GAPWISE POSITION RELATIVE TO WAKE MEASURE-MENTS IS APPROXIMATE

PRESSURE SURFACE

SUCTION SURFACE

TRAILING EDGE

LOCAL LOSS COEFFICIENT IN WAKE, $\left[\left(\overline{P_3} \right)_{3hi} - P_3 \right] / P_2 - P_2$

FRACTION OF VANE-TO-VANE GAP

Figure 39 —Local loss coefficients in wake of 50-percent span section of stator 67B for an inlet air angle near design and for one near minimum loss operation at 100-percent design speed. (Mach number, $M_2 = 0.70$.)
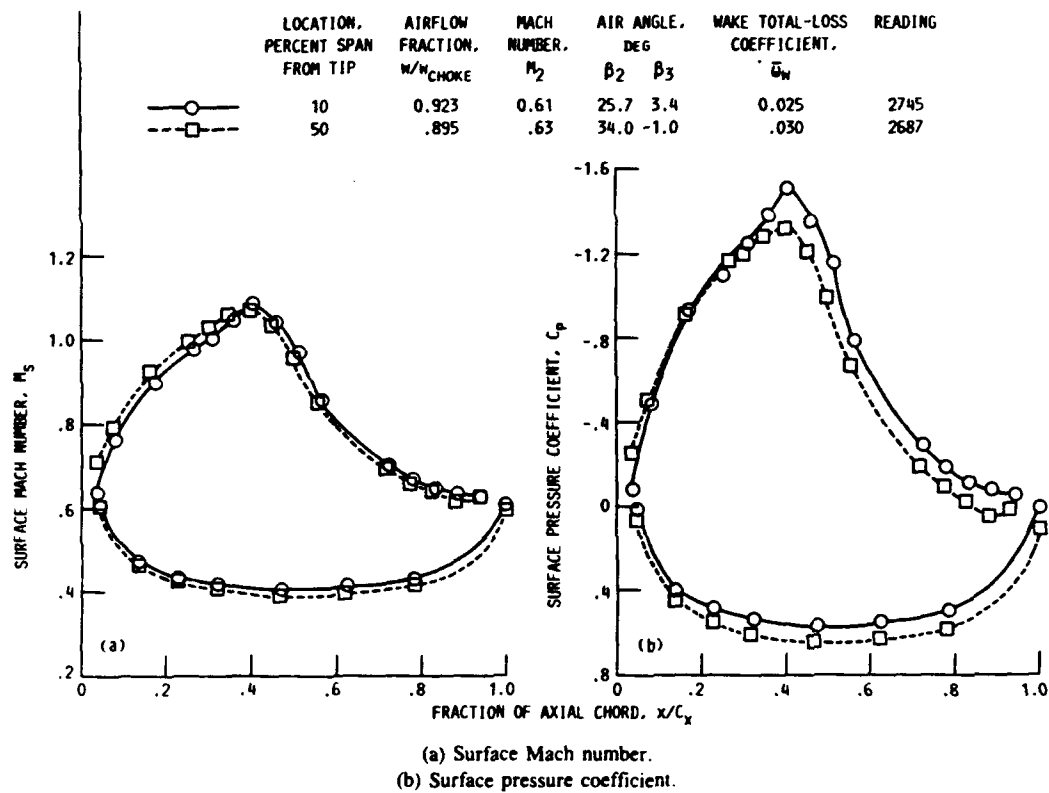
67

LOCATION, PERCENT SPAN FROM TIP	AIRFLOW FRACTION, w/w_{CHOKE}	MACH NUMBER, M_2	AIR ANGLE, DEG		WAKE TOTAL-LOSS COEFFICIENT, $\bar{\omega}_w$	READING
			β_2	β_3		
◯ 10	0.923	0.61	25.7	3.4	0.025	2745
▢ 50	.895	.63	34.0	-1.0	.030	2687

(a) Surface Mach number.

(b) Surface pressure coefficient.

Figure 40.—Surface pressure and Mach number distributions for tip and mean sections of stator 67B that produces the same loss levels operating at 90-percent design speed. Equivalent weight flow $[w \sqrt{\theta}/\delta]_{choke} = 34.95$ kg/sec.

SPEED, N_D, PERCENT OF DESIGN	AIRFLOW FRACTION, w/w_{CHOKE}	MACH NUMBER, M_2	AIR ANGLE, DEG		WAKE TOTAL-LOSS COEFFICIENT, $\bar{\omega}_w$	STATOR EFFICIENCY DROP, $\Delta\eta$	READING
			β_2	β_3			
◯ 90	0.923	0.77	42.1	7.9	0.159	0.035	2745
▢ 70	.695	.61	42.8	5.5	.085	.018	2716
△ 50	.494	.44	41.8	4.4	.043	.010	2727

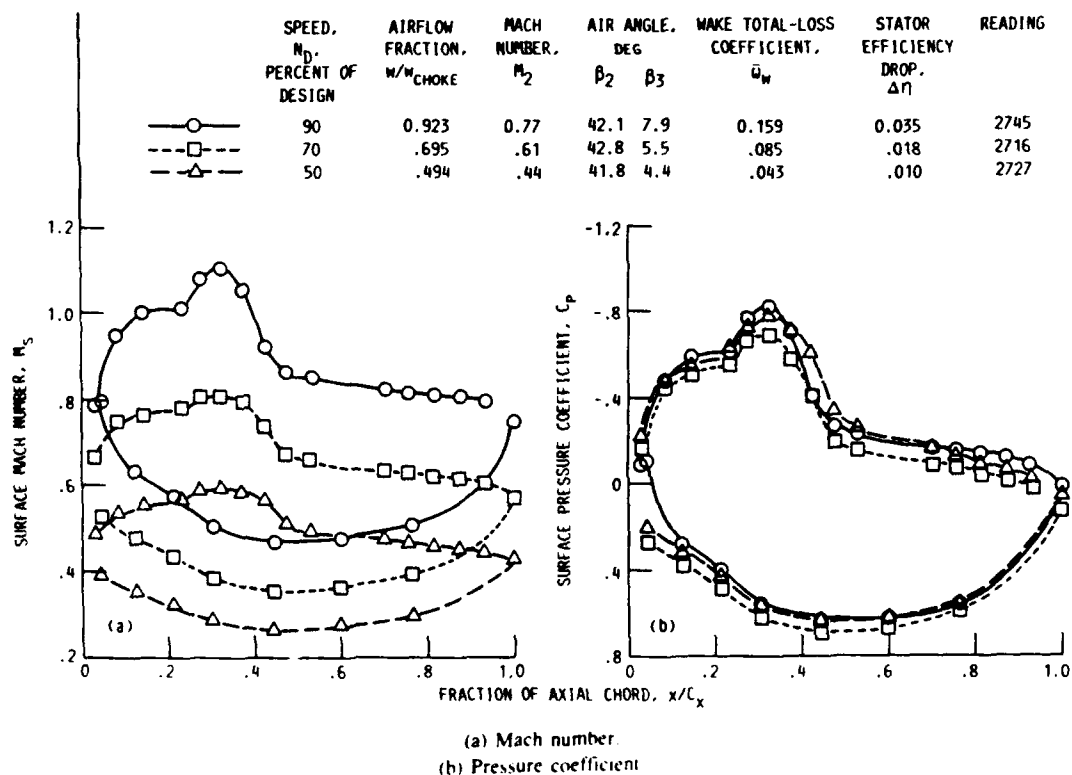(a) Mach number

(b) Pressure coefficient

Figure 41 —Surface pressure and Mach number distributions for hub section (90- percent span) of stator 67B at 90-, 70-, and 50-percent design speed when near best efficiency flows. Equivalent weight flow $[w \sqrt{\theta}/\delta]_{choke} = 34.95$ kg/sec
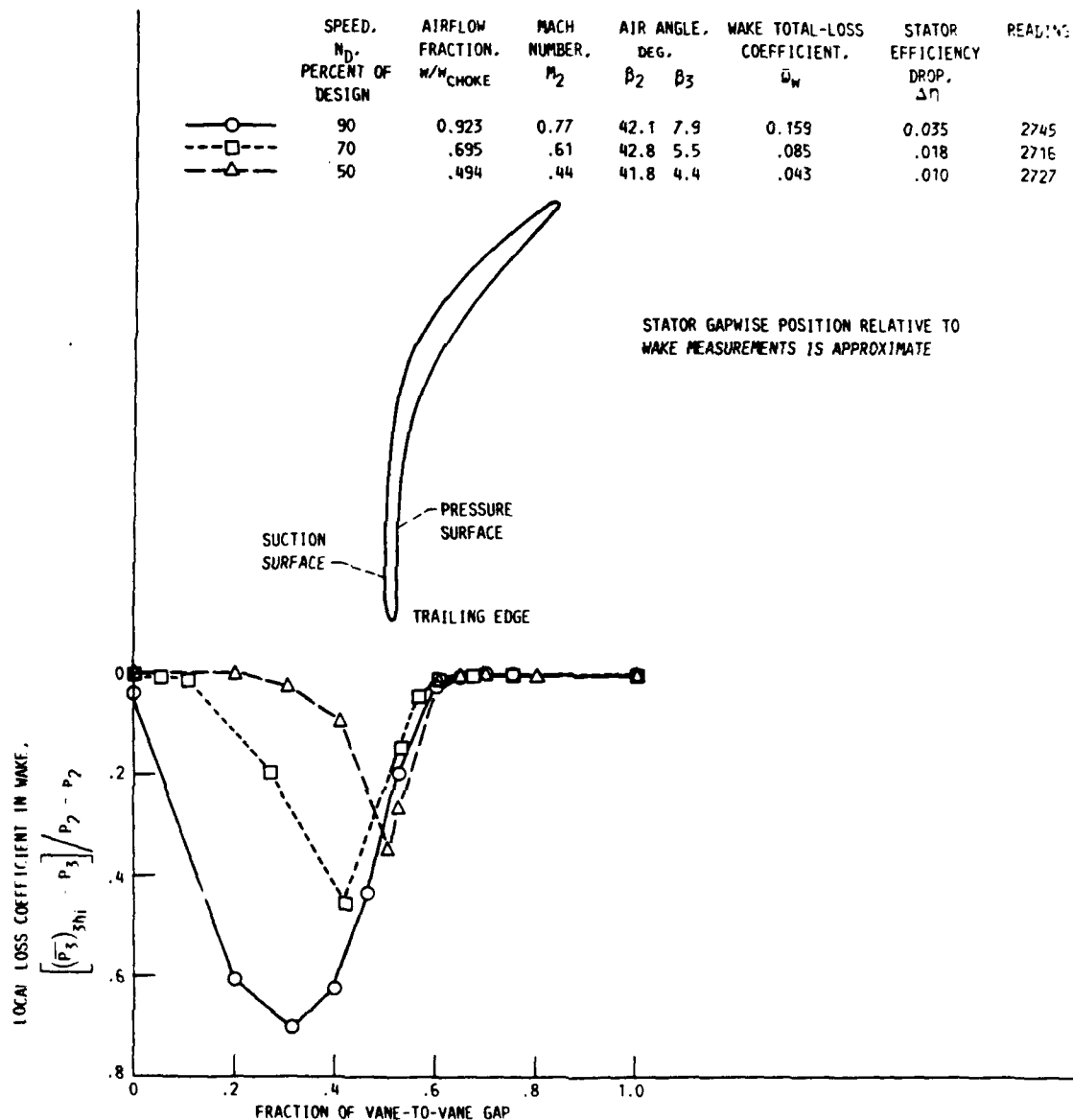
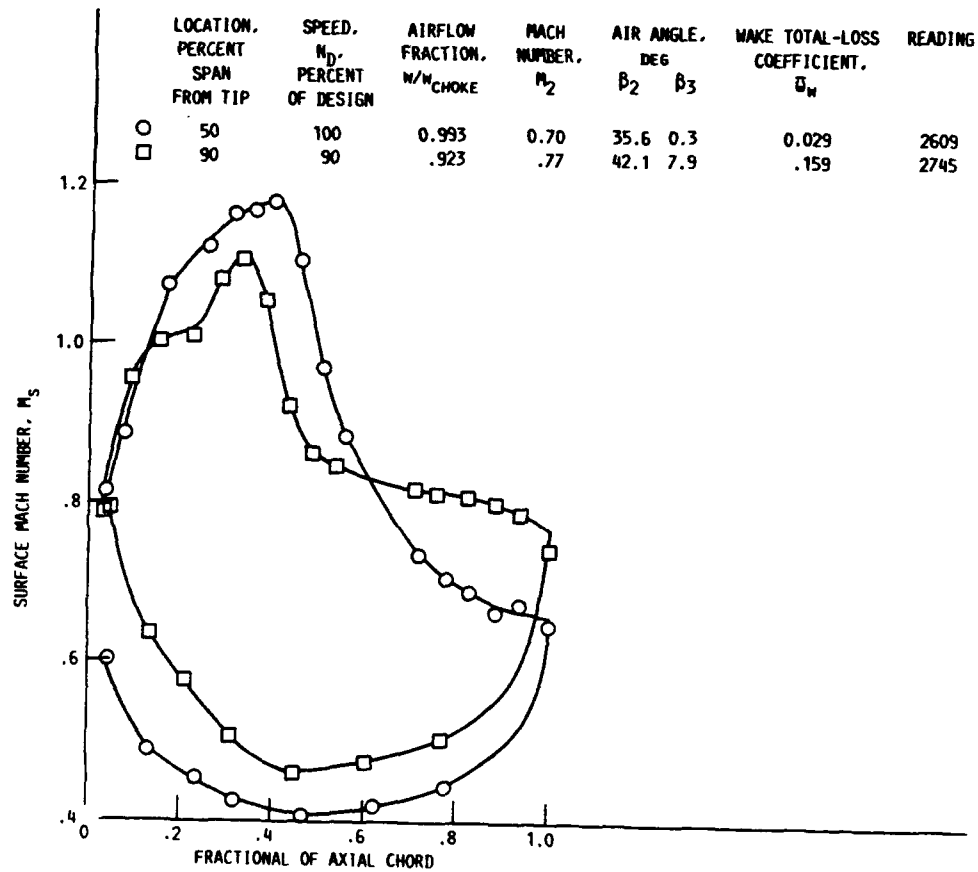|	SPEED, N_D, PERCENT OF DESIGN	AIRFLOW FRACTION, w/w_{CHOKE}	MACH NUMBER, M_2	AIR ANGLE, DEG. β_2	β_3	WAKE TOTAL-LOSS COEFFICIENT, $\bar{\omega}_w$	STATOR EFFICIENCY DROP, $\Delta\eta$	READING
—O—	90	0.923	0.77	42.1	7.9	0.159	0.035	2745
---□---	70	.695	.61	42.8	5.5	.085	.018	2716
—△—	50	.494	.44	41.8	4.4	.043	.010	2727

STATOR GAPWISE POSITION RELATIVE TO
WAKE MEASUREMENTS IS APPROXIMATE

PRESSURE
SURFACE

SUCTION
SURFACE

TRAILING EDGE

Figure 42 —Local loss coefficients in wake of hub section (90-percent span) of stator 67B at 50-, 70-, and 90-percent design speed when near best efficiency flows. Equivalent weight flow $[w\sqrt{\theta}/\delta]_{choke}$ = 34.95 kg/sec.

69

	LOCATION, PERCENT SPAN FROM TIP	SPEED, N_D, PERCENT OF DESIGN	AIRFLOW FRACTION, W/W_{CHOKE}	MACH NUMBER, M_2	AIR ANGLE, DEG β_2	β_3	WAKE TOTAL-LOSS COEFFICIENT, $\bar{\omega}_M$	READING
O	50	100	0.993	0.70	35.6	0.3	0.029	2609
□	90	90	.923	.77	42.1	7.9	.159	2745

Figure 43.—Surface Mach number distributions for stator 67B that show similar patterns over the forward chord but different ones over the aftchord.

STATOR	NUMBER OF VANES	AIRFLOW FRACTION, w/w_{CHOKE}	MACH NUMBER, M_2	AIR ANGLE, DEG β_2	β_3	WAKE TOTAL-LOSS COEFFICIENT, $\bar{\omega}_M$	EQUIVALENT WEIGHT FLOW, $[w\sqrt{\theta}/\delta]_{CHOKE}$, KG/SEC
S67B	17	0.852	0.76	47.4	6.5	0.135	34.95
S67A	34	.895	.74	47.9	1.0	.096	34.44
S67	34	.890	.72	48.0	-1.8	.080	34.74

(a) Surface Mach numbers.

(b) Surface Mach number curves predicted for $M_2 = 0.75$ and $\beta_2 = 49.9°$.

(c) Wake local loss coefficients.
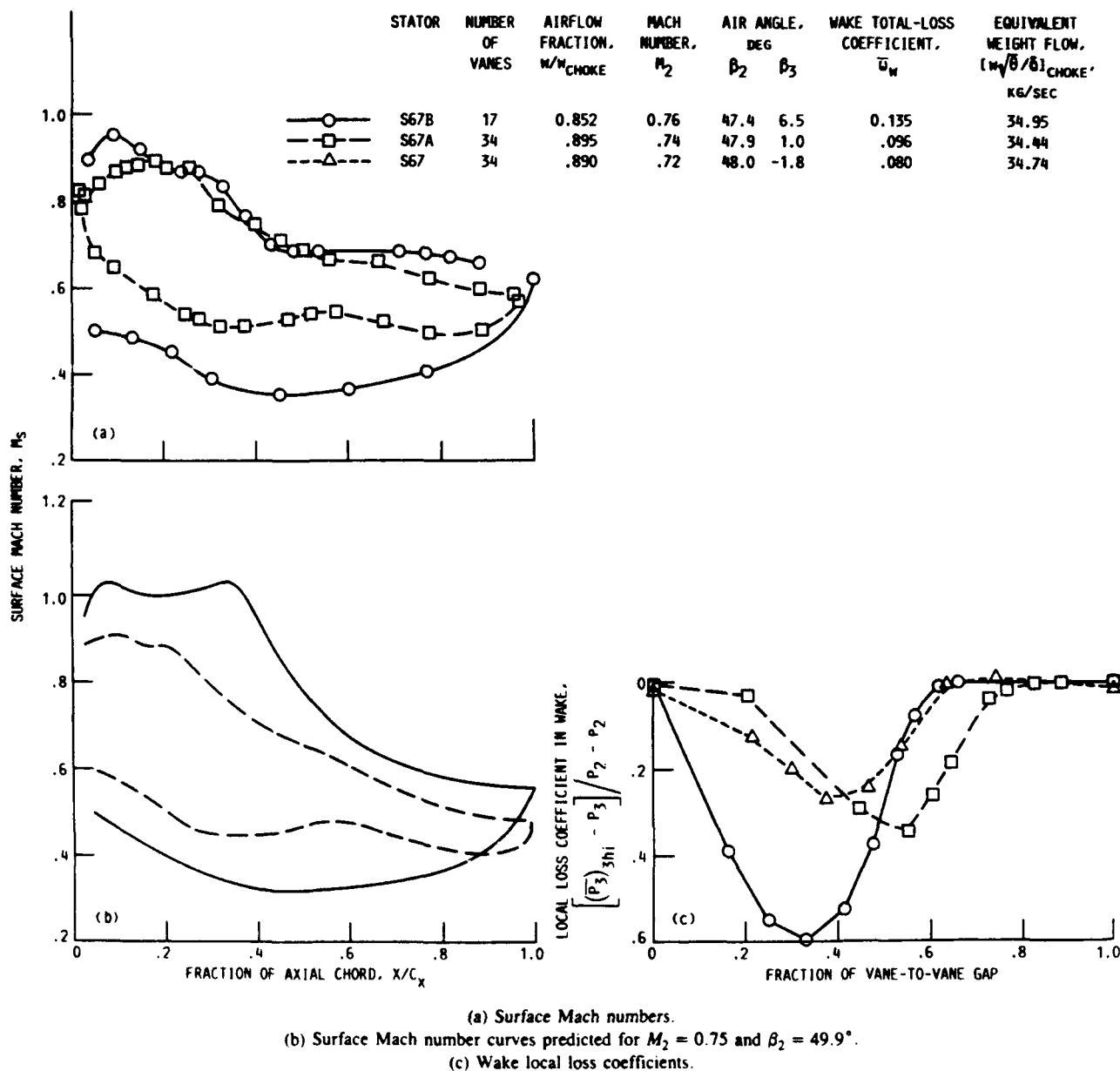
Figure 44.—Surface Mach number distributions and local wake loss coefficients for the hub section (90 percent span) of stators 67B, 67, and 67A at 90-percent design speed and comparable inlet conditions. Near best stator efficiency flows.
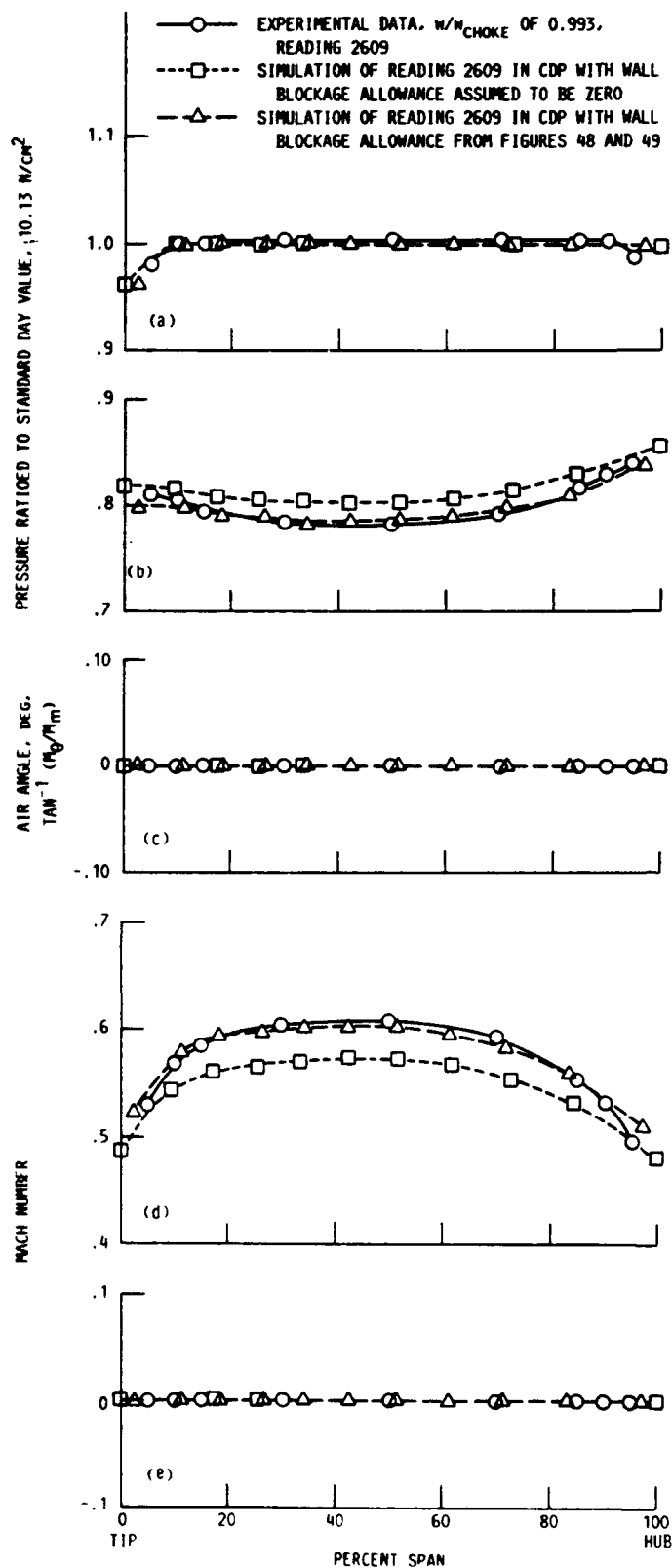
PRESSURE RATIOED TO STANDARD DAY VALUE, 10.13 N/cm^2

AIR ANGLE, DEG. TAN^{-1} (M_θ/M_m)
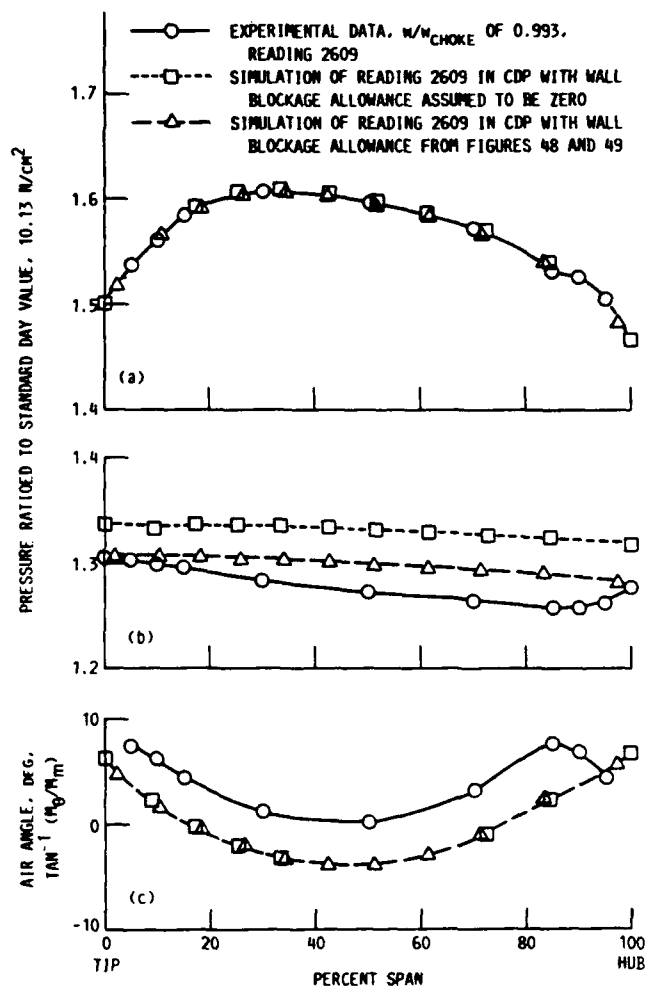
MACH NUMBER

TIP   PERCENT SPAN   HUB

(a) Total pressure ratioed to standard day value 10.13 N/cm^2.
(b) Static pressure ratioed to standard day value, 10.13 N/cm^2.
(c) Air angle, deg. tan^{-1} (M_θ/M_m)
(d) Absolute Mach number, M
(e) Tangential Mach number, M_θ

Figure 45 —Rotor 67 inlet conditions (station 1) across span for near peak efficiency operation at design speed Data compared to simulations in compressor design program (CDP) with different wall blockage allowances assumed
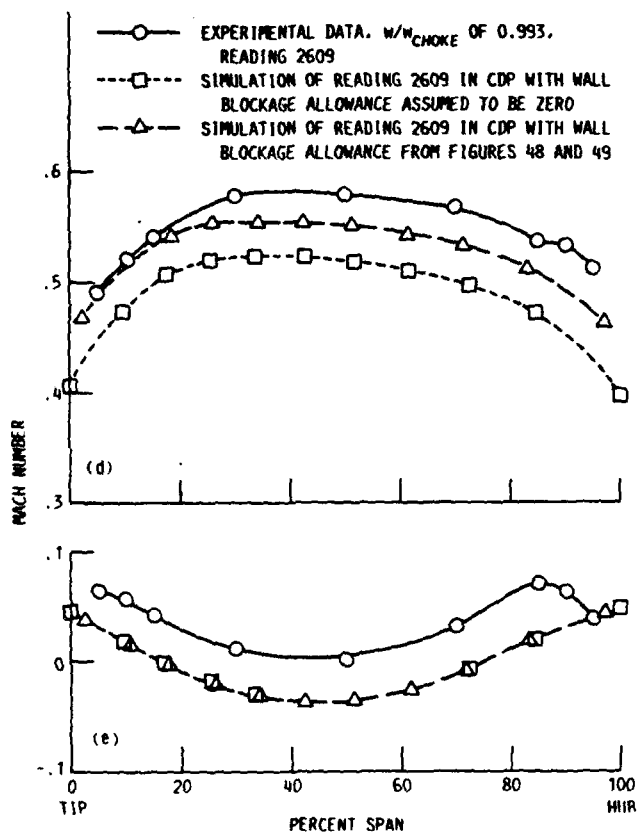
EXPERIMENTAL DATA, w/w$_{CHOKE}$ OF 0.993, READING 2609

SIMULATION OF READING 2609 IN CDP WITH WALL BLOCKAGE ALLOWANCE ASSUMED TO BE ZERO

SIMULATION OF READING 2609 IN CDP WITH WALL BLOCKAGE ALLOWANCE FROM FIGURES 48 AND 49

PRESSURE RATIOED TO STANDARD DAY VALUE, 10.13 N/cm^2

AIR ANGLE, DEG. TAN^{-1} (M_θ/M_m)

TIP   PERCENT SPAN   HUB
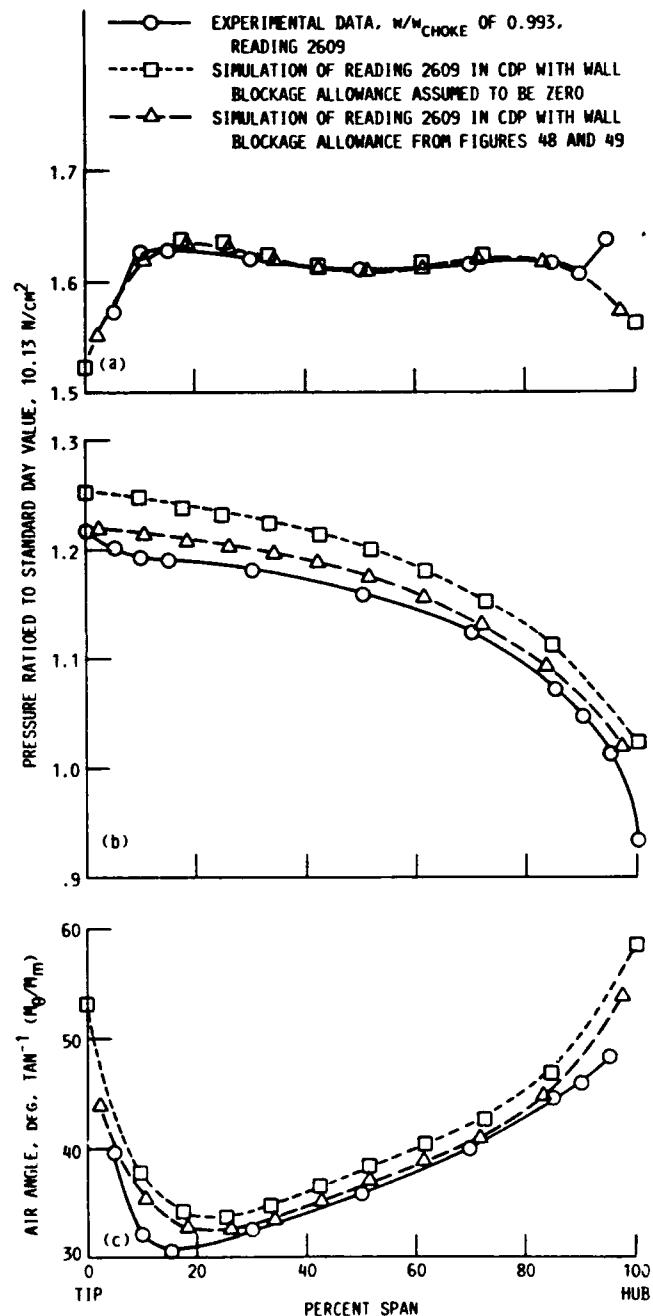
(a) Total pressure ratioed to standard day value, 10.13 N/cm^2.
(b) Static pressure ratioed to standard day value, 10.13 N/cm^2.
(c) Air angle, deg. tan^{-1} (M_θ/M_m).

Figure 46 —Stator 67B inlet conditions (station 2) across span for near peak efficiency operation at design speed Data compared to simulations in compressor design program (CDP) with different wall blockage allowances assumed

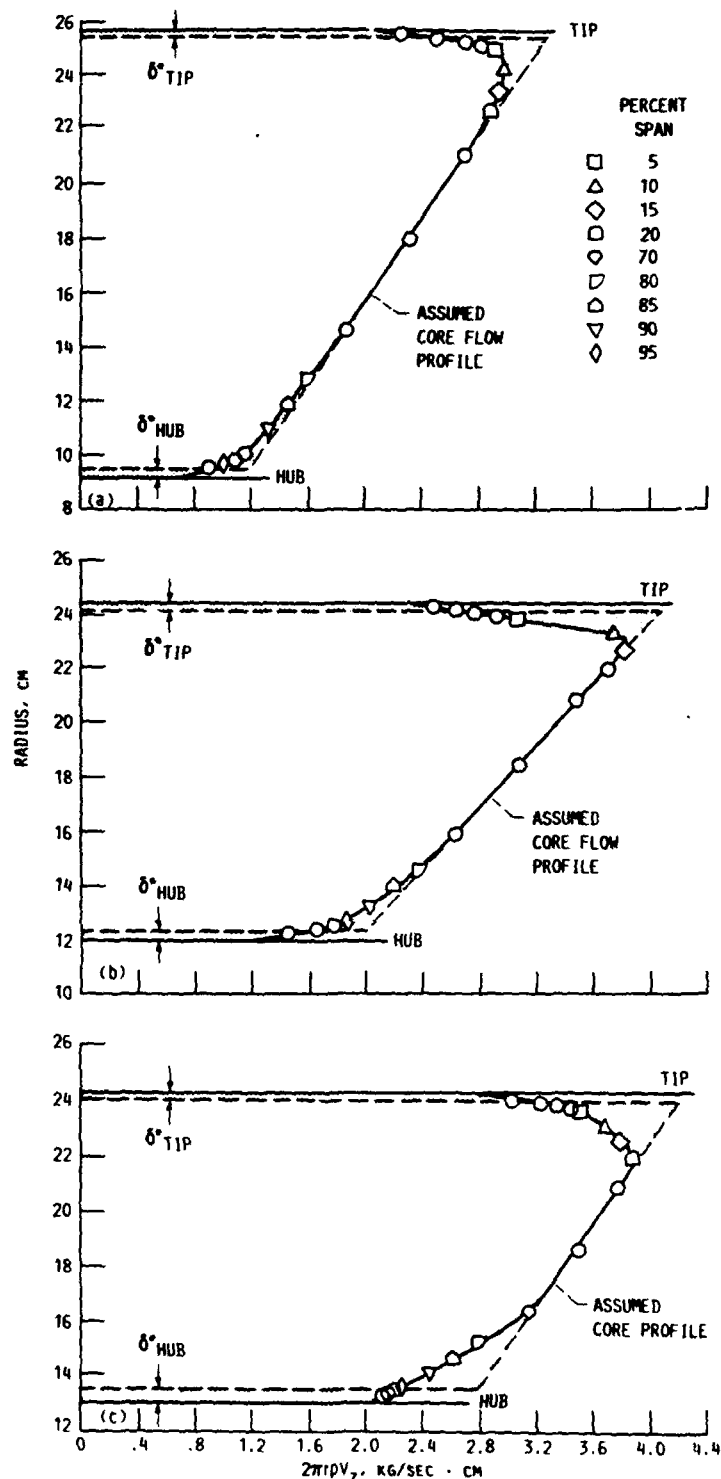EXPERIMENTAL DATA, w/w_{CHOKE} OF 0.993, READING 2609

SIMULATION OF READING 2609 IN CDP WITH WALL BLOCKAGE ALLOWANCE ASSUMED TO BE ZERO

SIMULATION OF READING 2609 IN CDP WITH WALL BLOCKAGE ALLOWANCE FROM FIGURES 48 AND 49

(d)

(e)

MACH NUMBER

(f)

TIP   PERCENT SPAN   HUB

(d) Absolute Mach number, M.
(e) Meridional Mach number, M_m.
(f) Tangential Mach number, M_θ.

Figure 46.—Concluded.

EXPERIMENTAL DATA, w/w_{CHOKE} OF 0.993, READING 2609

SIMULATION OF READING 2609 IN CDP WITH WALL BLOCKAGE ALLOWANCE ASSUMED TO BE ZERO

SIMULATION OF READING 2609 IN CDP WITH WALL BLOCKAGE ALLOWANCE FROM FIGURES 48 AND 49

PRESSURE RATIOED TO STANDARD DAY VALUE, 10.13 N/cm²

(a)

(b)

AIR ANGLE, DEG, $\tan^{-1} (M_\theta/M_m)$

(c)

TIP   PERCENT SPAN   HUB
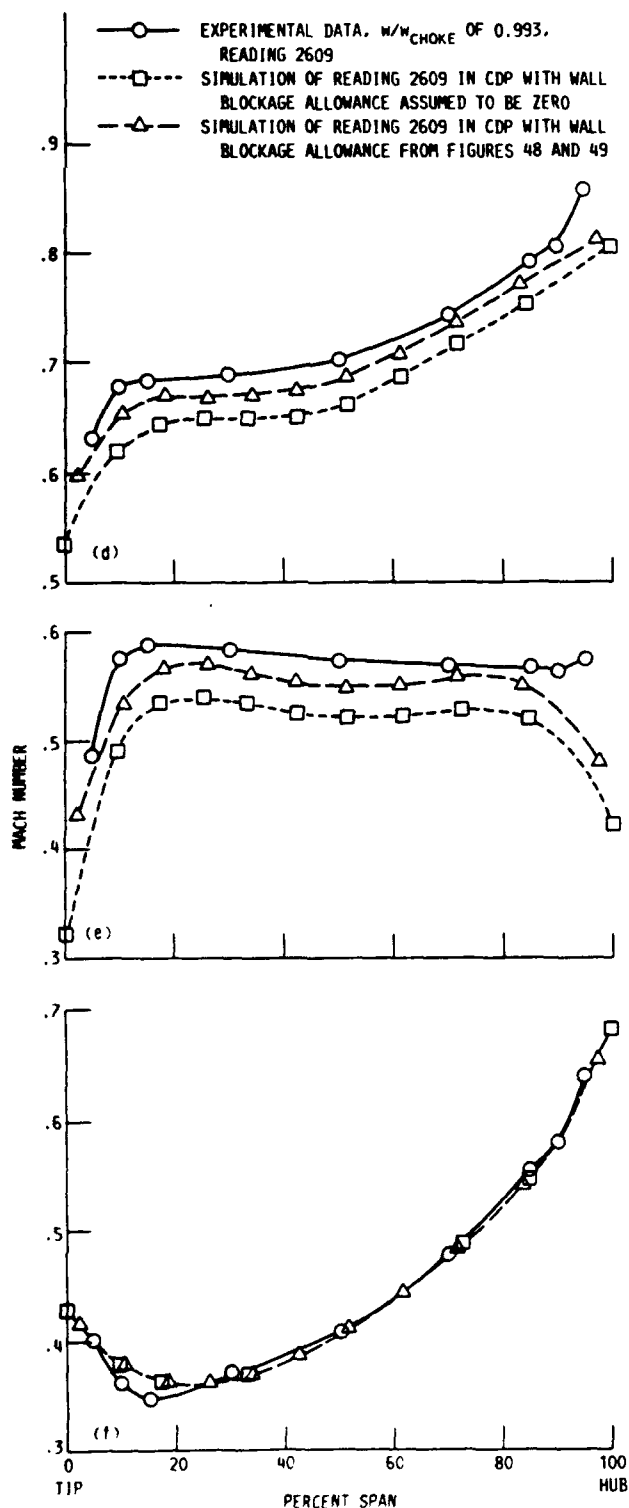
(a) Total pressure ratioed to standard day value, 10.13 N/cm².
(b) Static pressure ratioed to standard day value, 10.13 N/cm².
(c) Air angle, deg, $\tan^{-1} (M_\theta/M_m)$.

Figure 47.—Stator 67B outlet conditions (station 3) across span for near peak efficiency operation at design speed. Data compared to simulations in compressor design program (CDP) with different wall blockage allowances assumed.

73

EXPERIMENTAL DATA. w/w_{CHOKE} OF 0.993, READING 2609

SIMULATION OF READING 2609 IN CDP WITH WALL BLOCKAGE ALLOWANCE ASSUMED TO BE ZERO

SIMULATION OF READING 2609 IN CDP WITH WALL BLOCKAGE ALLOWANCE FROM FIGURES 48 AND 49

(d) Absolute Mach number, M.
(e) Tangential Mach number, M_θ.

Figure 47.—Concluded.

(a) Station 1 with 0.022 blockage allowance at tip and 0.011 blockage allowance at hub.

(b) Station 2 with 0.030 blockage allowance at tip and 0.017 blockage allowance at hub.

(c) Station 3 with 0.027 blockage allowance at tip and 0.025 blockage allowance at hub.

Figure 48.—Determination of wall blockage allowances at three measuring stations from stage 67B near-wall data series. Near peak efficiency operation at design speed. Reading numbers 2795 and 2800, airflow fraction $w/w_{choke} = 0.992$, and choked flow $w_{choke} = 34.95$ kg/sec.
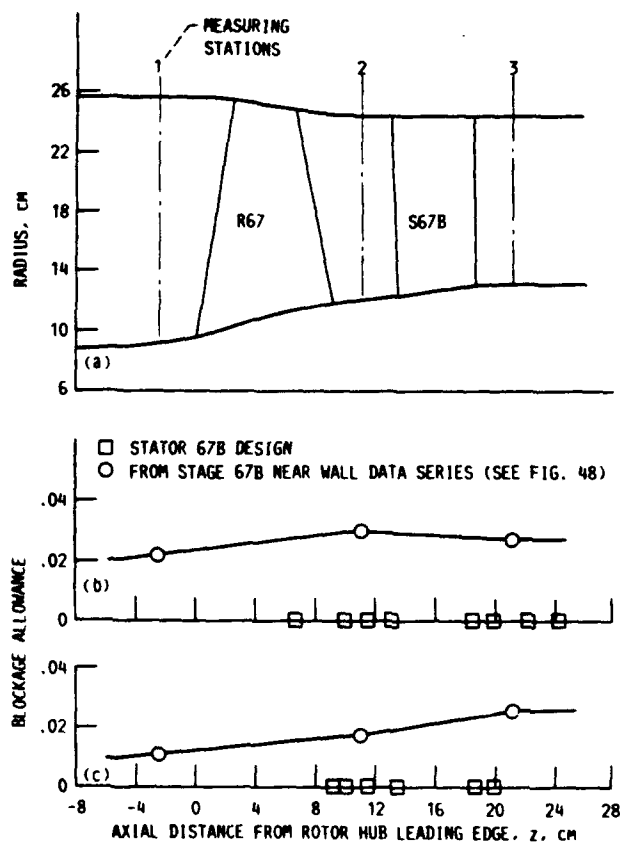
(a) Flow path schematic.
(b) Tip blockage allowance.
(c) Hub blockage allowance.

Figure 49.—Wall blockage allowance for stage 67B.
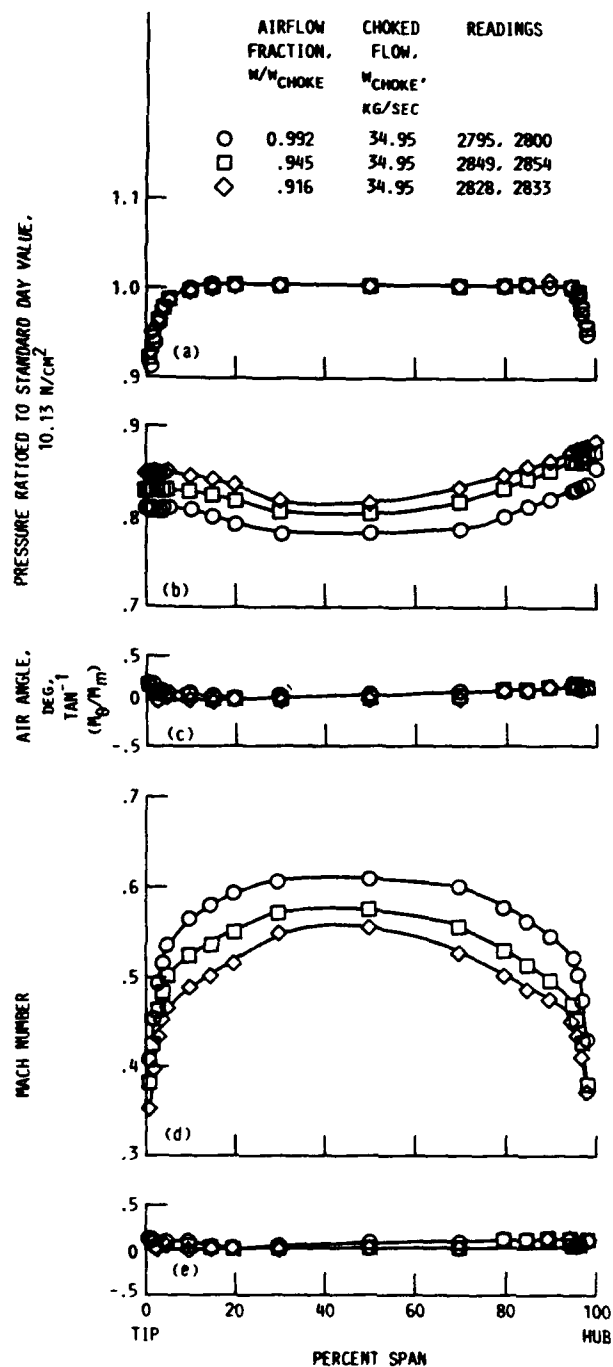
(a) Total pressure ratioed to standard day value, 10.13 N/cm².
(b) Static pressure ratioed to standard day value, 10.13 N/cm².
(c) Air angle, deg, tan⁻¹ (M_θ/M_m).
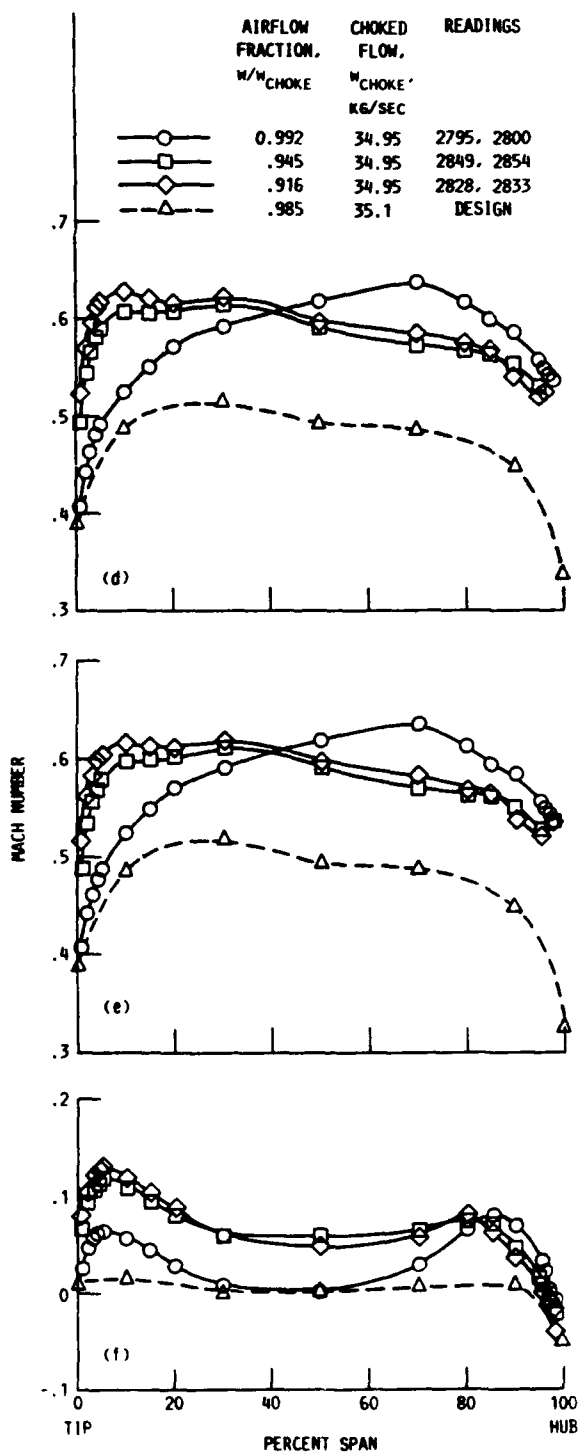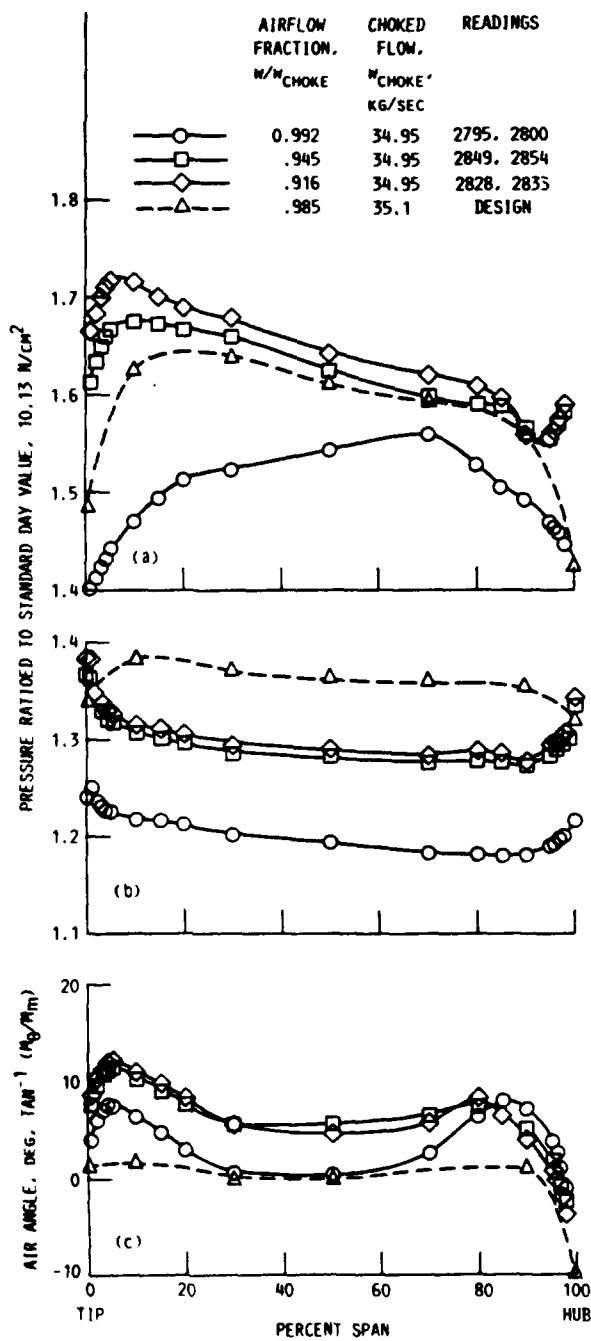(d) Absolute and meridional Mach numbers.
(e) Tangential Mach number, M_θ.

Figure 50.—Rotor 67 inlet conditions (station 1) across span operating with stator 67B over range of weight flows at design speed. Near-wall data series.
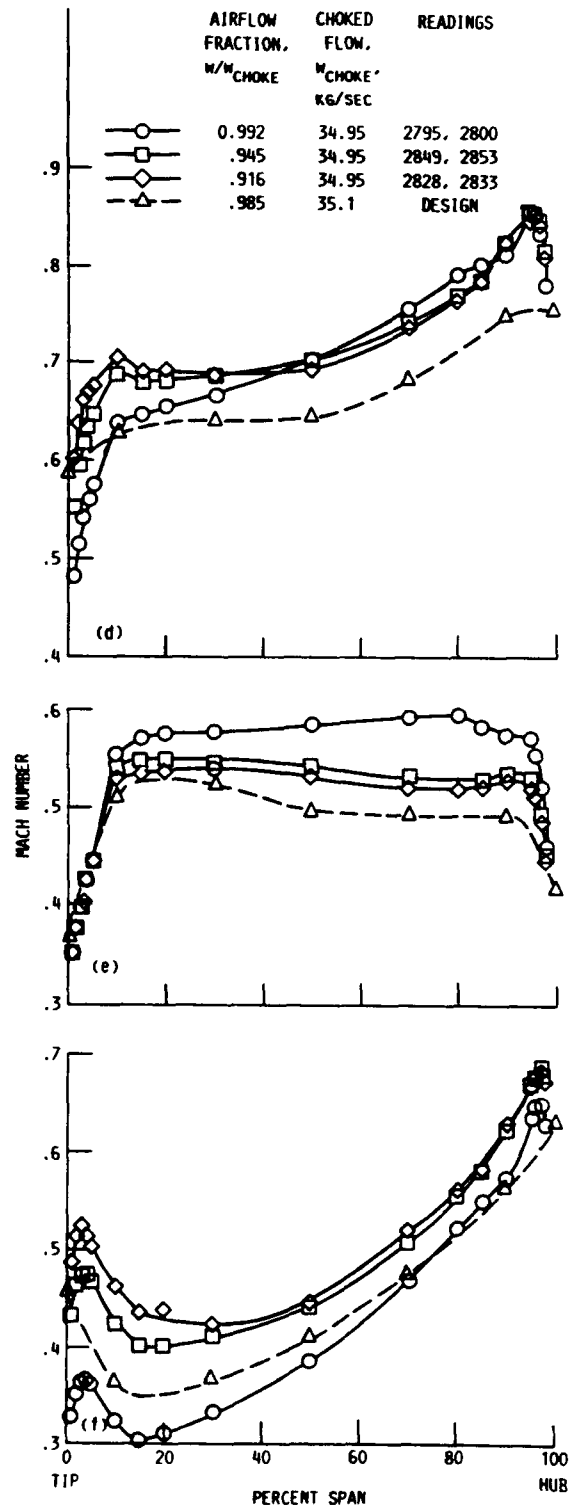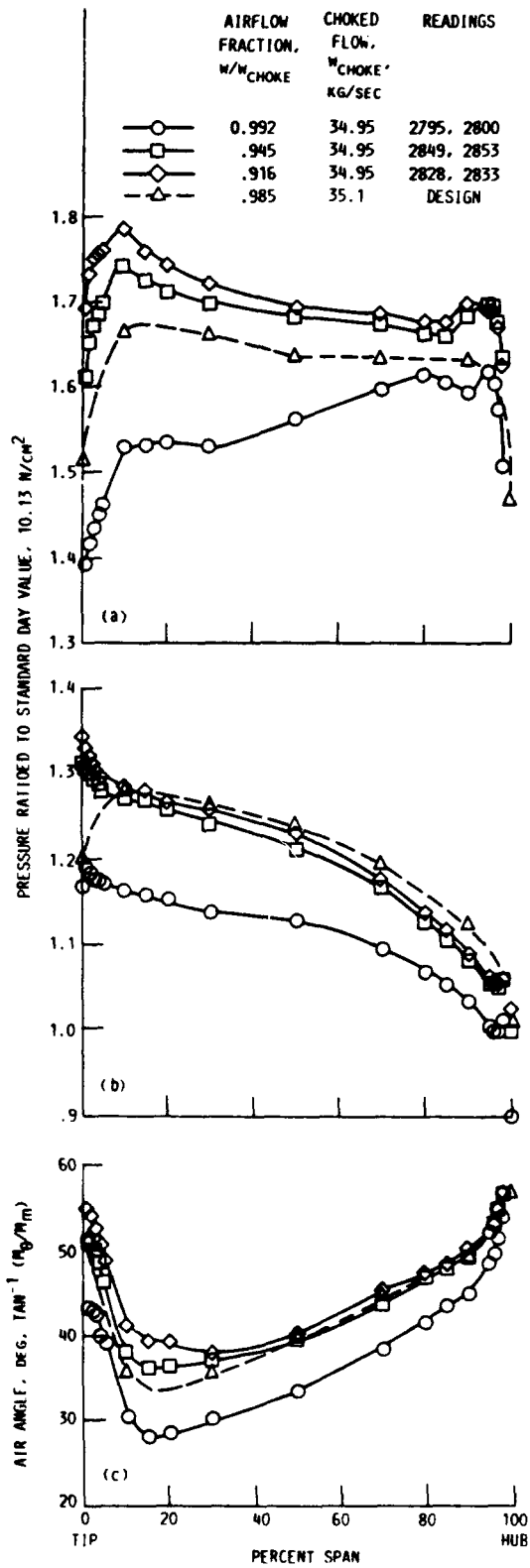
(a) Total pressure ratioed to standard day value, 10.13 N/cm².
(b) Static pressure ratioed to day value, 10.13 N/cm².
(c) Air angle, deg, tan⁻¹ (M_θ/M_m)

(d) Absolute Mach number, M
(e) Meridonal Mach number, M_m
(f) Tangential Mach number, M_θ

Figure 51 —Stator 67B inlet conditions (station 2) across span over range of weight flows at design speed. Near-wall data series.

Figure 52 —Stator 67B outlet conditions (station 3) across span over range of weight flows at design speed. Near-wall data series

NASA
National Aeronautics and Space Administration

Report Documentation Page

1. Report No. NASA TP-2852 AVSCOM TR 88-C-013	2. Government Accession No.	3. Recipient's Catalog No.

4. Title and Subtitle		5. Report Date
Design and Performance of Controlled-Diffusion Stator Compared With Original Double-Circular-Arc Stator		March 1989
		6. Performing Organization Code

7. Author(s)	8. Performing Organization Report No.
Thomas F. Gelder, James F. Schmidt, Kenneth L. Suder, and Michael D. Hathaway	E-4195

9. Performing Organization Name and Address	10. Work Unit No.
NASA Lewis Research Center Cleveland, Ohio 44135-3191 and Propulsion Directorate U.S. Army Aviation Research and Technology Activity—AVSCOM Cleveland, Ohio 44135-3127	505-62-51 1L161102AH45
	11. Contract or Grant No.

12. Sponsoring Agency Name and Address	13. Type of Report and Period Covered
National Aeronautics and Space Administration Washington, D.C. 20546-0001 and U.S. Army Aviation Systems Command St. Louis, Mo. 63120-1798	Technical Paper
	14. Sponsoring Agency Code

15. Supplementary Notes

16. Abstract

The performance capabilities of a fan stator blade row having controlled-diffusion (CD) blade sections were compared with the performance capabilities of a fan stator blade row having double-circular-arc (DCA) blade sections. A CD stator with the same chord length but half the blades of the DCA stator was designed and tested. The same fan rotor (tip speed, 429 m/sec; pressure ratio, 1.64) was used with each stator row. The design and analysis for the CD stator is described. The overall stage and rotor performances with each stator are then compared along with selected stator blade element data. The CD stator efficiency drop (rotor minus stage efficiency, overall) was about one percentage point higher than for the DCA stator at or near design speed because of high losses in the hub region.

17. Key Words (Suggested by Author(s))	18. Distribution Statement
Controlled-diffusion stator Turbomachinery	LIMITED DISTRIBUTION DOCUMENT Because of its significant technological potential, this information which has been developed under a U.S. Government program is being given a limited distribution whereby advanced access is provided for use by domestic interests. This legend shall be marked on any reproduction of this information in whole or in part. Date for general release _____ March 1991 _____ . Subject Category 07

19. Security Classif. (of this report)	20. Security Classif. (of this page)	21. No of pages	22. Price
Unclassified	Unclassified	80	